TEM Investigations of NdFeB Based Permanent Magnetic Materials

Stuart Young

submitted for the degree of PhD in the University of Glasgow, March 1994

One should never do anything one can't talk about after dinner
Oscar Wilde, from The Picture of Dorian Gray

It was not made clear how the answers to the religious quiz were assesed, were those who did not know that God created the earth in 7 days awarded 0 out of 10 for religious knowledge or 10 out of 10 for intelligence.

Letter to the *Independent.*

Acknowledgements

I would primarily like to thank my supervisor Professor J.N.Chapman for his help and guidance throughout this project. Thanks are also due to Dr W.A.P.Nicholson for much help on the HB5 and the EDX side of things and to Dr S.McVitie for answering many questions I should have known the answer to. Major thanks go to Dr L.Heyderman for time and energy spent helping me operate the CM-20 and to obtain some of the results for chapter 5. I would like to thank Miss M.Low and Mr I.McVicar for production of many photographs throughout the last three years and Mr J.Sims for technical support of the JEOL microscopes. I am indebted to Mr A.Young and Mr D.Mcdonald for endless repairs to our previous ion-beam thinner and other devices. Thanks to Prof H.A.Davies and the group at Sheffield University for supplying the sample investigated in chapter 8 and for the magnetic data in chapters 3 and 8. Thanks also to Dr E.W.Hill for provision of the materials investigated in chapter 9.

I would further like to thank the SERC and Philips Components Ltd for provision of a CASE award.

Lastly, thanks are due to Deborah Lee and Stewart James for keeping me sane, my mother for keeping me solvent and many PhD-doing friends who made me realise I wasn't alone.

Declaration

This thesis has been written solely by myself and details the research I have carried out in the Department of Physics and Astronomy at the University of Glasgow. The work described is my own, except where otherwise stated. Some of the results from this work have been presented in the following papers:

An Investigation of Domains and Walls in Two NdFeB alloys by Transmission Electron Microscopy, S.Young and J.N.Chapman to be published in IEEE Trans.Mag., proceedings of Intermag '93, Stockholm.

A TEM Investigation of the Magnetic Domain Structure in Nanocrystalline NdFeB Samples, J.N.Chapman and S.Young, submitted to the Rare-Earth Workshop, Birmingham, (1994).

Lorentz Microscopy with Application of Large Magnetic Fields, L.J.Heyderman, S.Young and J.N.Chapman, submitted to ICEM '94, Paris.

This thesis has not been submitted in any previous application for a degree.

Summary

This thesis documents work carried out on NdFeB based permanent magnetic materials using electron microscopy and related techniques. The first chapter introduces the basic theory of magnetism, the various energy terms which determine the overall state of a magnetic system and dicusses magnetic domains and domain walls. The development of permanent magnets and their uses are outlined.

Chapter 2 is a discussion of transmission electron microscopy (TEM) and related techniques. The principles of image formation in an electron microscope are given. The general technique of Lorentz microscopy is described and the various modes available are reviewed. The advantages and disadvantages are highlighted. The specific instruments in the Department of Physics and Astronomy at Glasgow University and their relative merits are described.

Chapter 3 describes the properties which are used to characterise a permanent magnet and gives a brief history of permanent magnets including the improvements recently realised to these properties. The material upon which most of the research was carried out is then discussed including how the bulk material is processed and how products are made from this material. The advantages and disadvantages of the material are described along with its properties and the various approaches used to enhance these properties. The preparation of samples from the bulk material suitable for the TEM is discussed in some detail.

Chapter 4 presents the results of TEM studies of thinned sections of sintered NdFeB. The domain structures observed are explained in terms of the inclination of the c-axis with respect to the sample normal. Data is shown for three different samples of the variation of domain period with the c-axis inclination. It is found that for a given inclination, the domain period is different for each material. The behaviour of domain walls at the boundary between two grains is studied. Various types of behaviour have been observed and these have been explained in terms of the inclination of the c-axes, the orientation of the boundary with respect to the domains and the possible existence of a Nd rich grain boundary phase.

Chapter 5 takes the data from the previous chapter and, using a modified version of

a model derived by Kooy and Enz, calculates the domain wall energy of each of the three samples. It is found that despite sample B and C having additions of Dy, the domain wall energies are very similar. This is explained on the basis that although Dy increases the anisotropy of the material, the exchange coupling is decreased. This results in a smaller domain wall width which theoretical models predict should result in a higher coercivity. Assuming that the increase in anisotropy field and the decrease in exchange coupling are linearly proportional to the Dy content, a factor of two increase in the coercivity is expected. Magnetising experiments have been undertaken which show that the domain width of favourably oriented domains increases as expected under the influence of an increasing field which supports the validity of the model as applied to these materials.

Chapter 6 gives the theory behind x-ray production and its subsequent extension to x-ray analysis and shows how this technique can be used to derive compositional information. The hardware is briefly described and the method of ratios for obtaining compositional information is explained. Finally, the accuracy of this approach is discussed.

Chapter 7 shows the results of x-ray analysis of sintered NdFeB. The basic nature of the materials has been studied and it has been observed to consist of $Nd_2Fe_{14}B$ grains separated by a predominantly Nd phase. The distribution of Nb within the materials takes various forms i.e. small precipitate-like features of varying composition or much larger Fe/Nb containing features. The smaller features, whilst similar in appearance can in fact be distinguished by their composition i.e. some of them are regions where Nb has substituted into the matrix for Fe while others appear to be genuine precipitates of what is presumed to be FeNbB. The remaining ones are rich in Nd but have not yet been identified. The larger features are also FeNbB which are crystals left over from the primary melt; these were found in Nd rich areas suggesting that the FeNbB has prevented formation of the $Nd_2Fe_{14}B$ phase.

Chapter 8 shows the results of investigations into melt-spun NdFeB. Foucault images have been obtained of three melt-spun materials with Nd contents ranging from 9.5% to 14%. The mean crystallite size and domain width are given and it has been found that the domain width increases with crystallite size. It has also been observed that the mean domain width decreases with increasing Nd content suggesting that, as in the sintered case, the Nd leads to increased decoupling of the grains.

Chapter 9 presents work carried out in collaboration with the University of Manchester on magnetoresistive multilayers. X-ray analysis was carried out on layers of NiFe separated by spacer layers of Cu or Ta. Two specimens with Cu spacer layers were studied, one where the Cu had been deposited at room temperature and one where the deposition temperature was 300°C. The higher temperature specimen had a broader distribution of Cu suggesting that the increase in temperature had led to more diffusion of the Cu into the NiFe. The Ta spacer layer was found to be narrower than both the Cu layers as a result of the chemical stability of the Ta-NiFe interface.

Finally, in chapter 10, the conclusions are stated and suggestions for future work are discussed.

Contents

List of Figures

List of Tables

Chapter 1

Ferromagnetic materials

A ferromagnetic material is one which may have a net magnetic moment in the absence of a magnetic field and below a certain temperature known as the Curie temperature (T_c). This net moment may be introduced by subjecting the material to a magnetic field. Upon removal of the field, some of the individual atomic moments remain aligned. As with most systems, the overall configuration is determined by energy considerations. The most important of these, their effect on the system and how they arise is discussed below.

1.1 Exchange Interaction

The exchange interaction is the basis of ferromagnetism. The alignment of atomic moments present in a ferromagnet would require the application of a massive field ($\sim 3\times 10^9 \mathrm{Am}^{-1}$). Weiss (1907) proposed the existence of a molecular field within the material which produced this alignment. This field arises as a result of the interaction of adjacent electron clouds which produces energy variations as a function of the relative orientation of the atoms. For two atoms with spins $\underline{s}_i$ and $\underline{s}_j$ separated by a distance r_{ij}, the potential energy is given by;

$$E_{ex} = -2J_{ij}\underline{s}_i \cdot \underline{s}_j \tag{1.1}$$

where J(r) is known as the exchange integral. The integral is positive for ferromagnetism and only nearest neighbour interactions are important in ferromagnetic materials. The negative sign means that the energy is lowest for parallel spins. Above T_c, the thermal

energy is sufficient to break down the exchange interaction and the material becomes paramagnetic i.e. the moments will align in the presence of an external field but there will be no spontaneous net moment.

1.2 Magnetocrystalline Anisotropy Energy

Whereas the exchange energy aligns the moments with each other, magnetocrystalline anisotropy determines the preferred direction. This direction is usually coincident with one or more of the crystal axes or planes. These directions are called the easy axes since the anisotropy energy is a minimum when the moments are parallel (or anti-parallel) to them. In Fe for example, the easy axes are parallel to the edges of the cubic lattice giving rise to three such axes. Clearly, in an ideal permanent magnet, it is preferable to minimise the number of directions in which the moments may easily align. In NdFeB which has a tetragonal crystal structure, the anisotropy is uniaxial along the c-axis. The anisotropy energy arises as a result of any rotation of the moments away from the easy axis and in this case is given by

$$E_{anis} = K_1 \sin^2\theta + K_2 \sin^4\theta + ... \tag{1.2}$$

where K_1 and K_2 are anisotropy constants and θ is the angle between the magnetisation and the c-axis.

1.3 Magnetostatic energy

If exchange and anisotropy were the only mechanisms controlling the system then, for a material with uniaxial anisotropy along the c-axis, the situation in figure 1.1a would arise where all the moments are parallel and aligned along the c-axis. This would lead to free magnetic poles at each end of the sample. These give rise to a demagnetising field (H_d) which as its name suggests is opposite to the direction of magnetisation. The magnetostatic energy is associated with the interaction of the magnetic dipoles with H_d whose magnitude is given by

$$H_d(r) = \frac{1}{4\pi}\int_V \frac{\nabla.\underline{M}}{r^2}dV + \frac{1}{4\pi}\int_S \frac{\underline{M}.\underline{n}}{r^2}dS \tag{1.3}$$

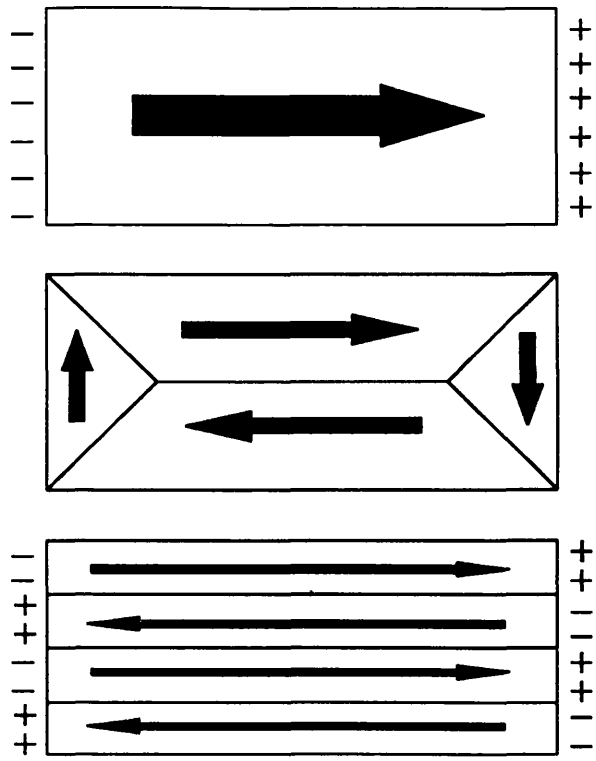

Figure 1.1: *(a) Fully magnetised ferromagnetic material (b) Domains in a material with cubic anisotropy (c) Domains in a material with uniaxial anisotropy*

M is the magnetisation within a sample whose volume is V and whose surface area is S. r is the position vector from the source to the field point and n is the unit vector normal to the surface. The magnetostatic energy is then given by

$$E_{mag} = -\frac{1}{2}\int_v \underline{M}.\underline{H}_d dV \tag{1.4}$$

In the case of an externally applied field H the magnetostatic energy is given by

$$E_{mag} = -\int_V \underline{M}.\underline{H} dV \tag{1.5}$$

1.4 Magnetic Domains

In order to reduce the magnetostatic energy, the system forms magnetic domains as shown in figure 1.1b for a material with cubic anisotropy and in figure 1.1c for a material

with uniaxial anistropy. Within each domain, the exchange and anisotropy energies are minimised but the number of free poles has been reduced and hence the magnetostatic energy has been reduced. The existence of these domains means that while each domain is magnetised to saturation, the net moment of a bulk sample may be zero.

1.5 Domain walls and their energy

The region between two domains is called a domain wall. If magnetostatic energy were the only consideration, the system would form many domains and thereby reduce E_{mag} to zero but this is prevented by the energy inherent in the domain wall which obviously increases in proportion to the number of domain walls. In a simple single-element magnetic system such Co, the wall will consist of a smooth rotation of the moment through 180°. This is known as a 180° Bloch wall (1932) after the first person to postulate the nature of the domain wall. In more complex multi-element systems such as those dealt with here, the structure of the wall is more difficult to describe since the moments of different elements may rotate at different rates giving rise effectively, to two overlapping domain walls of different widths. The wall energy arises as a result of an increase in exchange energy within the wall since adjacent moments are not perfectly parallel. This encourages as wide a wall as possible in order to minimise the angle between adjacent moments but this is countered by the anistropy energy which tends to narrow the wall in order to minimise the number of moments which do not lie parallel to the easy axis. In a simple system, the wall energy can be determined by integrating the excess of anisotropy and exchange energies across the width of the domain wall. This will be discussed in more detail in chapter 5.

1.6 Permanent magnets

A permanent or hard magnet is one whose microstructure impedes the formation and movement of domain walls. Therefore once it has been fully magnetised, it will be unable to form domains and hence demagnetise itself. The dividing line between soft and hard materials has been set at a coercivity of 0.012T ($10 kAm^{-1}$). Modern day permanent

magnets have coercivities two orders of magnitude greater than this and a material with a coercivity of 0.012T would not be considered hard today.

They are in use in many areas of modern life but their biggest uses are in motors and actuators. Their advantage over not only earlier magnets but also previously non-magnet based systems is their low volume, high efficiency and high power to weight ratio.

1.6.1 Coercivity

At best, a permanent magnet will be subject only to its own demagnetising field but it is likely that it will be subject to other demagnetising influences such as temperature and external fields. Therefore, the coercivity (H_c) must be as large as possible. Thetheoretical maximum possible coercivity (assuming $K_1 \gg K_2$) for an infinite magnet is equal to the anisotropy field H_a which is given by;

$$H_a = 2K_1/M_s \tag{1.6}$$

Anisotropy fields in the material under investigation here i.e. $Nd_2Fe_{14}B$ can be as high as 7.3T (Herbst, 1991) but coercivities are much less than this as a result of the shape of, the finite extent of and imperfections within, the magnet. Better estimates can be modelled by the following expression although as will be described later, this still does not take account of some factors (Hirosawa, 1990);

$$H_c = \frac{2K_1}{M_s} - NM_s \tag{1.7}$$

where N is a factor representing the demagnetising field.

1.6.2 Coercivity Mechanisms

There are two coercivity mechanisms which describe the behaviour of permanent magnets.

Wall Pinning

In this mechanism, when the material is magnetised, the domain walls are not actually annihilated. The microstructure of the material pins the domain walls. This pinning can take place at the edge of the grain as in the case of $SmCo_5$ or at sites within the grain.

These sites may already be in the material in the form of defects or may be introduced by the addition of another element to the material. One possible cause of the pinning effect arises as a result of reduced magnetisation at a point because, for example, the added material is non-magnetic. This leads to an energy minimum at that point which traps the wall.

Nucleation of reverse domains

Here all domain walls are removed from the sample when it is magnetised. The coercivity is determined by the field required to nucleate a reverse domain. The associated domain wall then sweeps through the material. The coercivity is greatly reduced if the material contains defects or sharp corners where the field may be far higher, making it much easier to nucleate a reverse domain.

These two types of behaviour can be easily identified from the initial magnetisation curves of the material. Figure 1.2 shows a hysteresis loop with two initial magnetisation curves; in curve 1, the domain walls move easily as can be seen by the rapid increase in M - this material would be nucleation dominated. In curve 2, there is little wall movement since the walls are pinned. When the applied field reaches the coercivty, the pinning sites are not strong enough to hold the walls and they are swept out. The walls may still be annihilated in this material meaning that the initial coercivity mechanism will be nucleation but the pinning will contribute to the coercivity.

1.6.3 Remanence

There is little point in having a large coercivity if the magnet does not provide a large induction. When magnet is being magnetised, we would expect almost 100% alignment of the c-axes but on removal of this field, inevitably some domains will reverse and the remaining magnetisation or remanence (M_r) will be smaller than M_s. NdFeB has M_r/M_s >90%

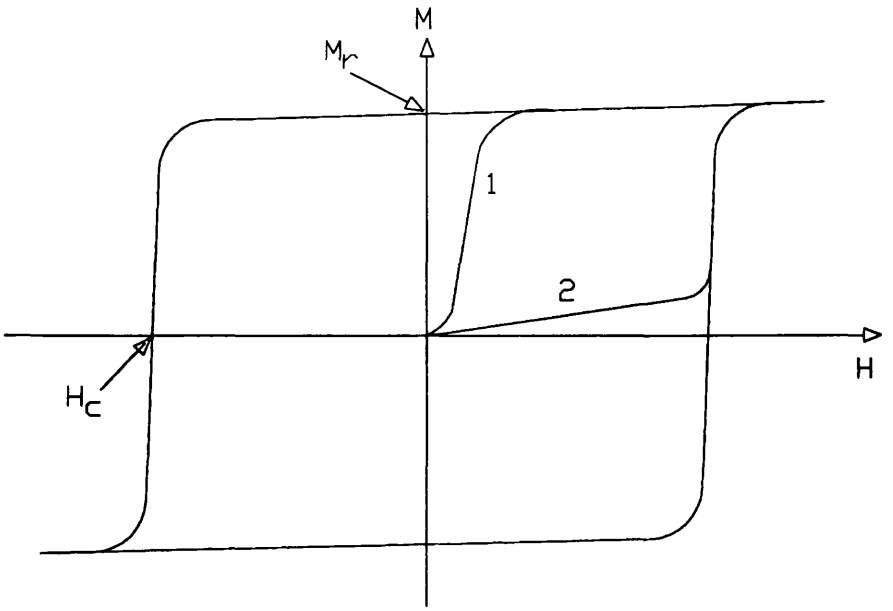

Figure 1.2: *Hysteresis loop showing domain wall pinning*

1.6.4 Energy product

The energy product is related to the area inside the hysteresis loop and is a measure of the induction that can be produced by a unit volume of material. The theoretical maximum energy product is given by the following expression.

$$(BH)^*_{max} = (4\pi M_s)^2/4 \tag{1.8}$$

This maximum can only be achieved if the magnet is able to retain M_s in a field at least as large as $2\pi M_s$ or, put more simply, if the magnets coercivity is large enough so that the magnet does not demagnetise itself under the influence of its own field. NdFeB has $(BH)^*_{max}$ ~64MGOe. The larger the energy product, the smaller the volume of material required to produce the same induction. this has obvious applications in miniaturisation.

1.6.5 Development of hard magnetic materials

The first known permanent magnet was Fe_3O_4, a naturally occuring oxide of iron, which was discovered by the ancient Greeks in Magnesia which subsequently gave its name to

both the material (magnetite) and the study of all such materials. The first magnets provided a very weak field and were far too easily demagnetised. To overcome this, the material was made into long thin bars and bent into the familiar horseshoe shapes. This is known as shape anisotropy where the atomic moments are forced to align in a particular direction as a result of the shape of the material. This clearly limits the shape and hence the application of the material.

Subsequent magnets were made from high carbon hard steels which contained ~1% carbon. These were physically hard while the previous low carbon steels were soft. This gave rise to the terms hard and soft magnets (Jiles, 1991). Further advances involved the addition of tungsten and chromium to the steels. The best of these had B_r=0.96T, H_c=0.02T and $(BH)_{max}$=0.9MGOe.

The next development, in the 1930's was the AlniCo magnet made from an alloy of iron, aluminium, cobalt and nickel. This consisted of a strongly magnetic phase (Fe–Co) and a much weaker phase (Ni–Al) whose purpose was to provide pinning sites for the domain walls. The magnet relied on the formation of long rod like grains of Fe–Co which gave rise to shape anisotropy. These magnets had B_r=1.31T, H_c=0.07T and $(BH)_{max}$=5.0MGOe.

The hard ferrites (Jiles, 1991), developed in the 1950's and still in widespread use make use of crystalline anisotropy in order to improve the coercivities available at the time. The ferrites currently used are barium and strontium ferrite and still retain the biggest share of the permanent magnet market simply because they are the cheapest per unit energy product. They can also be easily shaped by embedding them in a plastic matrix. They have B_r=0.4T, H_c=0.24T and $(BH)_{max}$=3.5MGOe which demonstrates a dramatic improvement in the coercivity but at the expense of a slight drop in the energy product.

The next major development, and the forerunner of NdFeB, was $SmCo_5$ (Jiles, 1991) which was a specific attempt to bring together the high magnetocrystalline anisotropy of the light rare earths with the high magnetisation of the 3d transition metals. It is simplistic but not inaccurate to think of the TM as providing the majority of the magnetic moment and the RE as providing the strong anisotropy neccessary to align the moments. The coercivity in $SmCo_5$ is dominated by wall pinning, i.e when the material is magnetised, the domain walls are pinned at the grain boundaries. The properties of this

material were a vast improvement on all previous materials with B_r=0.98T, H_c=0.87T and $(BH)_{max}$=20.1MGOe. Until 1978, SmCo had been the most popular new material but the civil war in Zaire (the main source of Co) made it too expensive to be commercially viable and so alternative materials had to be found.

1.7 NdFeB

Despite reports in 1935 of a Nd-Fe alloy with a coercivity of 0.43T (Drozzina and Janus, 1935), it was not until 1984 that the Sumitomo Mining Company produced the first commercial NdFeB magnet (Sagawa et al, 1984). It relies on the hard magnetic $Nd_2Fe_{14}B$ tetragonal phase which has a large magnetocrystalline anisotropy ($K \simeq 5 \times 10^6 Jm^{-3}$ compared to $K \simeq 5 \times 10^4 Jm^{-3}$ in Fe). This anisotropy is uniaxial and is directed along the c-axis. The coercivity in NdFeB is dominated by nucleation of reverse domains. As stated earlier, nucleation may occur if a grain has sharp edges or irregularities where the demagnetising field can become much more intense and as a result the production of NdFeB (see chapter 3) is designed to minimise any such areas and also to magnetically isolate each grain so that if one reverses, the others are unaffected. This is achieved by having an excess of Nd in the initial alloy. At the sintering temperature, the excess Nd is a liquid phase which flows between the $Nd_2Fe_{14}B$ grains helping to smooth the edges and, since it is non-magnetic, isolating them. The basic NdFeB alloy has exceptional magnetic properties i.e. a coercivity of up to 1.3T and an energy product of 40MGOe which is more than ten times greater than a ferrite magnet. Unfortunately, it has a low Curie temperature (592K), and relatively high temperature coefficients of remanence, α, and intrinsic coercivity, β, which are defined as the percentage change in B_r and H_c when the temperature is raised from T_1 to T_2 (Hirosawa et al, 1990) i.e.

$$\alpha(T) = \frac{B_r(T_2) - B_r(T_1)}{B_r(T_1)} \frac{1}{T_2 - T_1} \times 100\% \tag{1.9}$$

$$\beta(T) = \frac{H_{ci}(T_2) - H_{ci}(T_1)}{H_{ci}(T_1)} \frac{1}{T_2 - T_1} \times 100\% \tag{1.10}$$

T_1 is usually room temperature. As a result, the expression for coercivity (equation 1.7) may be more generally written as;

$$H_c(T) = \alpha(T)\frac{2K_1}{M_s} - NM_s \tag{1.11}$$

Typical values are $\alpha \simeq$-0.1%/°C and $\beta \simeq$-0.8%/°C (Xaio et al, 1988) which results in a serious deterioration of the magnetic properties at temperatures as low as 100°C. This, combined with their susceptibility to corrosion, has limited their widespread use. The approaches used to counter these problems are discussed in detail in chapter 3.

1.8 References

F.Bloch, *Z.Physik*, **74**, p295 (1932).

V.Drozzina and R.Janus, Nature, pp36–37, (1935).

J.F.Herbst *Rev.Mod.Phys.*, **63**, pp819–899, (1991).

J.F.Herbst and J.J.Croat, *J.Mag.Mag.Mat.*, **100**, pp57–78, (1991).

S.Hirosawa, A.Hanaki, H.Tomizawa and A.Hamamura *Physica B*, **164**, pp117–123, (1990).

D.Jiles, Introduction to Magnetism and Magnetic Materials, Chapman and Hall (1991).

G.Martinek and H.Kronmuller, *J.Mag.Mag.Mat.*, **86**, pp177–183, (1990).

K.S.V.L.Narasimhan, *J.Appl.Phys.*, **57**, pp4081–4085, (1985).

M.Sagawa, S.Fujimura,N.Togawa, H.Yamamoto and Y.Matsuura, *J.Appl.Phys*, **55**, pp2083–2087, (1984).

H.H.Stadelmaier and K.J.Strnat, Paper No 17A0206 at the 10th International Workshop on Rare-Earth Magnets and their Applications, Kyoto, Japan, 16–19 May, (1989).

P.Weiss, *J.Phys.*, **6**, p661 (1907).

Y.Xiao, S.Liu, H.F.Mildrum, K.J.Strnat and A.E.Ray, *J.Appl.Phys.*, **63**, pp3516–3518, (1988).

Chapter 2

Electron Microscopy Techniques

This chapter describes some of the techniques available for magnetic imaging and in particular image formation in a conventional transmission electron microscope (CTEM).

The first techniques used to observe magnetic domains were optical. This was done by Bitter in 1931 when he coated a ferromagnetic crystal with a colloidal solution of ferromagnetic particles. These particles are attracted to the domain walls and the domain structure on the surface of the material can be highlighted.

More advanced optical techniques include the use of the Kerr and Faraday effects. The first technique relies on the rotation of the plane of polarisation of a polarised beam of light when it is reflected from a magnetic material. The second is similar but depends on the rotation of the plane of polarisation of light when the beam is transmitted through a thin film of magnetic material or a transparent bulk material.

All of these techniques are limited to investigation of the surface of materials and more importantly by the wavelength of light which limits the resolution of the observations to $\sim 0.5\mu$m. The transmission electron microscope can be used to study the magnetic structure within a sufficiently thin sample and resolutions of 10–50nm can be obtained depending on the imaging technique used. Fidler (1991A, 1991B) has reviewed the use of electron microscopy in the study of permanent magnets and discussed some of the features observed.

2.1 Electron microscopy and domain imaging

2.1.1 Electron Illumination Systems

The cheapest and most basic electron source in a CTEM is the heated tungsten filament (Spence, 1981). This provides a virtual source size of $\simeq 30\mu$m and a brightness of $\simeq 5\times10^5 \mathrm{Acm}^{-2}\mathrm{sr}^{-1}$ at 100kV. The energy spread in the source is $\approx$2.5eV. This operates at a vacuum of around 10^{-5}torr. A much more expensive option is the lanthanum hexaboride (LaB_6) filament which consists of a single crystal of LaB_6 directly heated by tungsten connections. The virtual source size for this filament is 5–10μm and the brightness is increased to $\simeq 7\times10^6 \mathrm{Acm}^{-2}\mathrm{sr}^{-1}$ and the energy spread is only 2.5eV as a result of the lower operating temperature. This tip is more susceptible to contamination and has to be operated at vacuums of better than 10^{-6}torr. The best performance is obtained from a cold field emission gun (FEG) where the emitter is frequently a single crystal of (310) tungsten. The electrons are extracted from the tip by an electrode biased at a few kV. The source size is 5–10nm giving rise to a brightness of 10^7–$10^8 \mathrm{Acm}^{-2}\mathrm{sr}^{-1}$. The energy spread is only 0.3eV. This tip has to be operated at pressures of $<10^{-10}$ torr to minimise the damage from contaminants. This is achieved by use of a differential pumping aperture between the gun chamber and the column which allows the column to remain at a pressure of $<10^{-8}$ torr. Despite the high vacuum, the electron emission drops during use as contaminants build up on the tip, and as a result, the tip must occasionally be 'flashed' by passing a small current through it to remove them. It is also possible to have a thermally assisted FEG where the tip is heated. This prevents the build up of contaminants and avoids the need for flashing the tip. The increased operating temperature results in a larger energy spread of $\sim$0.9eV.

2.1.2 Image formation in CTEM and STEM

In STEM, a probe is raster scanned across the sample whereas in CTEM, the beam is stationary, and a much larger area of specimen is illuminated. The following discussion will concentrate on STEM but by the principal of reciprocity (Cowley, 1969) it can be shown that these concepts apply to CTEM imaging. The electron source is operated at a high negative potential (100-200kV) and the emergent electrons are accelerated towards

an anode through two or more condenser lenses which produce a demagnified image of the source. By varying the excitations of these lenses, the source size and angular convergence of the beam can be determined. The sample usually rests within the objective lens and as a result, it is subject to both a pre-specimen and a post-specimen field. The pre-specimen field is effectively the probe forming lens while the post-specimen field is the first imaging lens. It is this field that provides the first stage of magnification and this lens must be as free of aberrations as possible.

2.1.3 Probe Size and Resolution

There are two contributions to the probe size namely the incoherent probe size, d_i and the coherent probe size, d_c. d_i is determined simply by the demagnification of the electron source while d_c is calculated by assuming a point source. There are three main effects which determine d_c (Colliex and Mory, 1983).

1. Diffraction: the first zero of the Airy disc produced by diffraction is at a radius r_d where

$$r_d = 0.61\lambda/\alpha_0 \tag{2.1}$$

where λ is the electron wavelength and α_0 is the probe angle.

2. Spherical aberration produces a disc of radius $C_s\alpha_0^3$ in the Gaussian image plane and in the least confusion disk plane at a distance of $\Delta z = (3/4)C_s\alpha_0^2$ in front of it;

$$r_s = C_s\alpha_0^3/4 \tag{2.2}$$

where C_s is the spherical aberration coefficient of the lens. An optimum probe angle can be calculated to minimise both these effects i.e.

$$\alpha_{opt} \propto \left(\frac{\lambda}{C_s}\right)^{1/4} \tag{2.3}$$

The exact coefficient of proportionality depends on whether r_d and r_s are summed linearly or in quadrature - both are in common use.

3. Chromatic aberration: This is proportional to ($\Delta V/V+2\Delta I/I$) where ΔV and ΔI are the voltage and current variations in the beam - these are determined initially by the energy spread in the electron source but energy loss within the sample will also contribute to this.

Again, the probe size is determined by summing d_i and d_c linearly or in quadrature.

2.1.4 Electron Diffraction

In addition to producing a magnified image, the objective lens also produces a diffraction pattern in the back focal plane. In the case of the two CTEMs used in this work, three further intermediate lenses and a projector lens are used to transmit the image to a fluorescent screen (or alternatively to a low light TV level camera). By varying the excitation of these lenses, so that they are focused on the back focal plane, it is possible to obtain a magnified electron diffraction pattern of the specimen. If an aperture is placed in the first image plane of the objective then a selected area diffraction (SAD) pattern can be obtained, this allows a diffraction pattern to be obtained from a small area of specimen whilst still using a plane electron wave.

2.1.5 The JEOL 1200-EX

This microscope operates at an accelerating voltage of 120kV and has an immersion objective lens with a field of 0.5-1T at the specimen plane. The illumination is provided by a tungsten filament. The specimen sits within the field of the objective lens which is a problem for investigations of the magnetic microstructure since the field will alter or even destroy the magnetic domain structure. It is necessary in microscopes with immersion lenses, to study magnetic samples in 'low mag' mode where the objective lens is switched off. This usually limits the maximum magnification to $\times$ $\sim$1000 since the distance between the sample and the 'imaging lens' i.e. the first intermediate lens (also known as the diffraction lens) is vastly increased. The 1200-EX has an objective mini lens which is below the sample and whose field does not affect the sample. The object distance of the mini lens is greater than that of the objective but is much smaller than that of the first intermediate lens and consequently, if the free lens control (FLC) is used

which allows the user to determine the excitation of each lens individually, the maximum possible magnification is increased to $\times$ ~5600. The resolution of this microscope with the objective lens as the first imaging lens is 4Å.

2.1.6 The JEOL 2000-FX

This is a 200kV machine which was specially modified to investigate magnetic materials and avoids the problems of the objective field by having a non-immersion or field free objective lens similar to that described by Tsuno and Taoka (1983) which allows the sample to rest in a vertical field of <20gauss. The lens can be thought of as two standard objective lenses at equal distances above and below the specimen. The 2000-FX at Glasgow is fitted with a LaB_6 filament. The advantage of the field free lens is that the magnetic structure of samples is unaffected and can now be studied at much greater magnification i.e. up to 50k$\times$. The consequence of this is a small deterioration of the resolution to ~1.2nm and a reduction in the maximum magnification by a factor of 4 due to the increased object distance.

2.1.7 Lorentz microscopy

All of the imaging techniques employed in this work come under the heading of Lorentz microscopy which is so called because it relies on the strong interaction of electrons with a magnetic field through the Lorentz force which is given by;

$$\underline{F} = \epsilon(\underline{v} \times \underline{B}) \tag{2.4}$$

From this it is possible to calculate a deflection angle, β, for an electron travelling through a magnetic film (see figure 2.1) i.e.

$$\beta_x(x) = \frac{e\lambda}{h} \int_{-\infty}^{\infty} B_y(x,z)dz \tag{2.5}$$

where $B_y(x,z)$ is the y component of the magnetic induction at the point (x,z). Within a domain, the induction is constant and so for a material of thickness t, assuming no stray field, we obtain

$$\beta = \frac{eB_s\lambda t}{h} \tag{2.6}$$

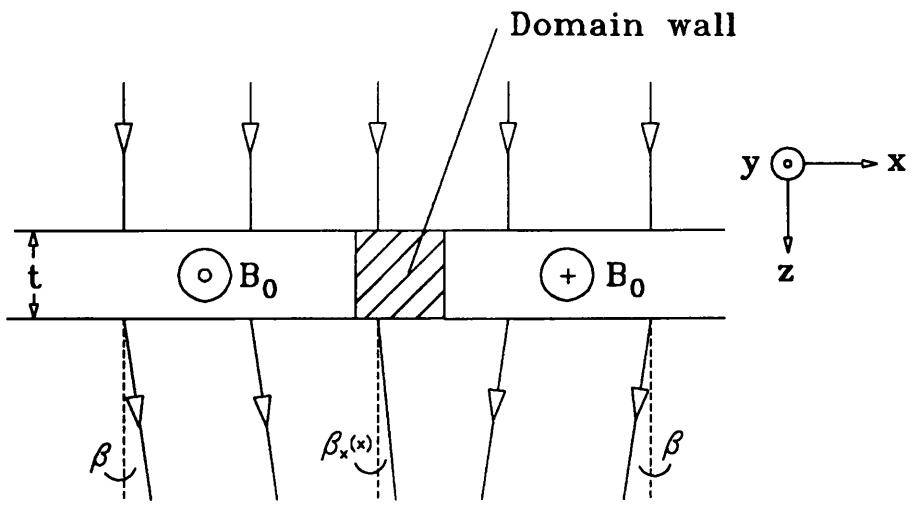

Figure 2.1: *Schematic of electron passing through a thin film*

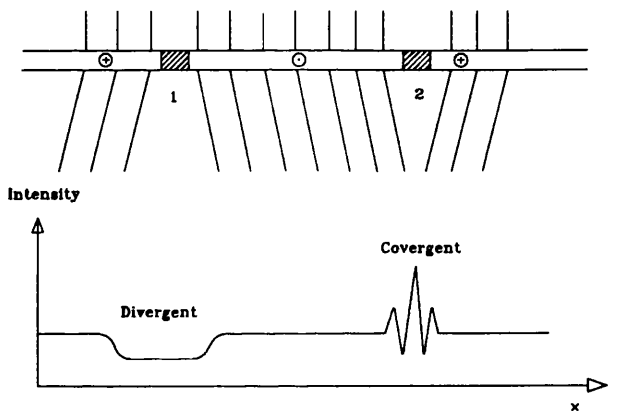

Figure 2.2: *Schematic of the Fresnel mode of Lorentz microscopy*

i.e. for an 80nm grain of NdFeB, a 100keV electron would be deflected by 0.1mrad. For comparison, the first order Bragg angle would typically be 3mrad.

Fresnel mode

Figure 2.2 shows a plane electron wave passing through a magnetic film where the direction of magnetic induction is in the plane of the film. At alternate domain walls, the electron beam either diverges or converges. While the specimen plane and the object plane

are coincident, the final image will reveal no magnetic detail. If the objective excitation is increased (overfocus) or decreased (underfocus) the two planes will no longer be coincident. Consider the case of overfocus, the object plane will now be below the specimen and it is clear from the diagram that below domain wall 1, there is a deficit of electrons which will show up in the final image as a narrow band. Conversely, below domain wall 2, there is is an excess of electrons which interfere with each other to form a fringe pattern. The coherence is rarely good enough to observe this pattern and this area shows up as a narrow bright band in the final image. If the objective lens is underfocussed then this situation is reversed and domain wall 1 will appear bright while domain wall 2 appears dark. The advantages of this mode are that it is easy to implement and the contrast levels are high. It also reveals wall contrast independent of the direction of induction which makes it easy to locate features of interest. This last feature can also be a disadvantage since no information can be deduced about the magnitude of the induction. This mode is non-linear and domain wall information is difficult to obtain. Lastly, Fresnel contrast can also be obtained from non-magnetic features and so magnetic detail may be obscured.

Foucault mode

Figure 2.3 again shows a beam of electrons passing through a magnetic film but it can be seen that in the diffraction plane the beam has been split into two spots by the magnetic induction in alternate domains. If an aperture is used to block one of these beams then some domains in the final image will appear dark while others are bright. Both these techniques rely on having a coherent electron beam which means using small condensor apertures and/or small spot sizes. Use of the LaB_6 filament makes this possible at an acceptable level of illumination. This technique is only feasible on the 2000-FX due to the position of the objective aperture in the diffraction plane of the lens (Tsuno and Taoka, 1983). As well as being an in-focus technique, the Foucault mode has the great advantage of allowing the induction to be mapped in specific directions by careful positioning of the aperture. This mode is highly non-linear and reproducibility of results is difficult since the aperture has to be positioned manually.

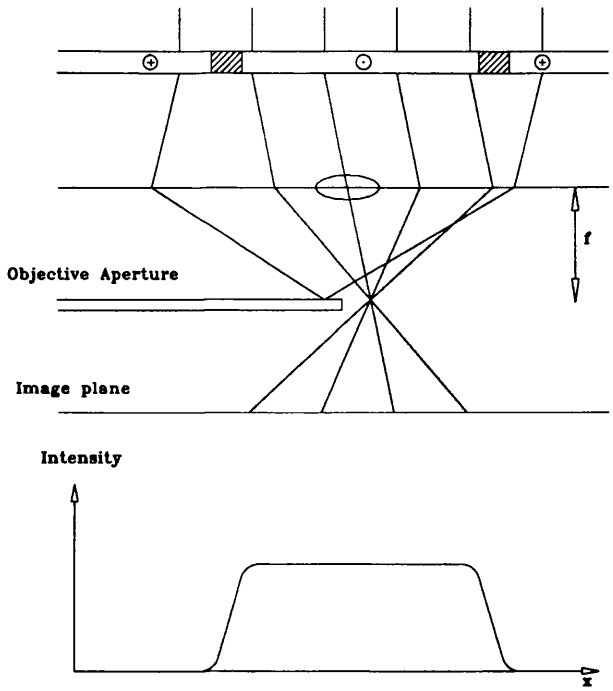

Figure 2.3: *Schematic of the Foucault mode of Lorentz microscopy*

2.1.8 The VG Microscopes Extended HB5 STEM

This microscope has a FEG which operates at an accelerating voltage of 100kV. There are two main modes of operation used in the HB5 i.e. 'low mag' mode and imaging mode. In low mag mode only one lens is used along with one probe forming aperture and a spray aperture. The lens used is one of the condenser lenses, C1 or C2. C2 produces a smaller probe with lower beam current as a result of the position of the aperture. The probe forming aperture is the selected area aperture (SAA) (see figure 2.4) while the virtual objective aperture (VOA) is used as a spray aperture to block any elastically scattered electrons. This mode has a resolution of ~10nm if C2 is used and ~20nm if C1 is used. The probe angle, probe size and probe current have been calculated (Morrison, 1981) for C2 and a probe defining aperture of 100μm leads to α_0 ≈0.5mrad, d_c ≈10nm, d_i ≈6.2nm and I_p ≈0.2nA.

In imaging mode, the objective lens is on and C1 or C2 is used depending on probe size/beam current requirements. The objective aperture (OA) is used to form the probe.

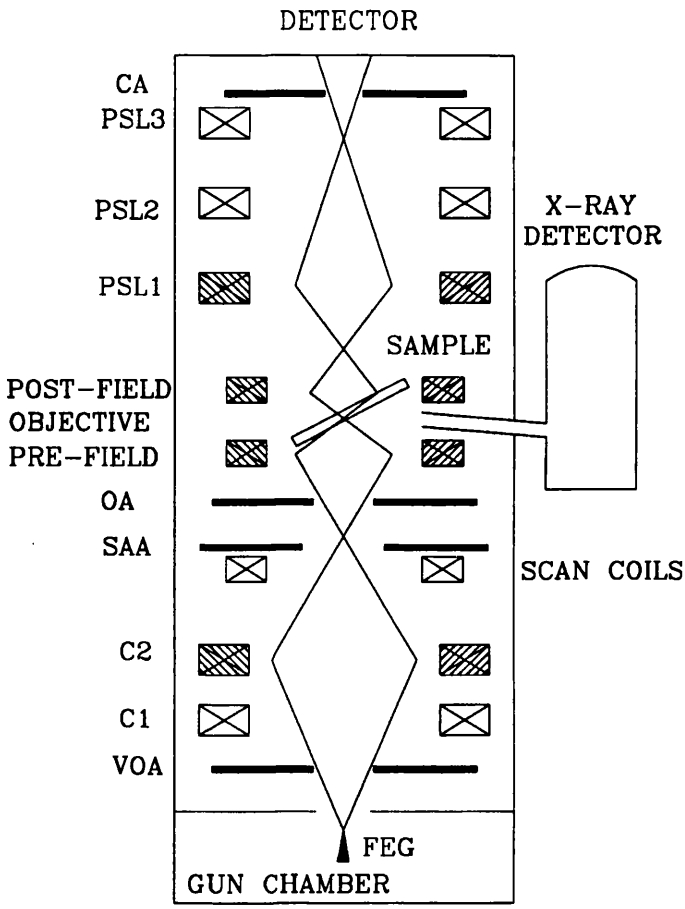

Figure 2.4: *Schematic of the VG HB5*

This is a problem if x-ray analysis is being undertaken since the objective aperture is very close to the x-ray detector and would produce a massive Mo signal from the aperture material which could obscure some of the peaks. More importantly,it produces a much larger background count which could swamp any smaller peaks. As a result, it is preferable to use a slightly modified form of the imaging mode where the VOA, which is approximately conjugate with the OA, is used to form the probe. A schematic of the electron trajectory is shown in figure 2.4, the lenses that are switched on are shown shaded. For a 100μm VOA, $\alpha_0 \approx$11mrad, $d_c \approx$2.4nm, $d_i \approx$0.3nm and $I_p \approx$0.2nA.

The HB5 has three post specimen lenses (PSLs) which transfer the signal to the detector. There are in fact three available detectors (1) a bright field (BF) with outer

diameter 5.5mm, (2) an annular dark field (ADF) with a hole of 2mm, an inner diameter of 3.5mm and an outer diameter of 11mm, (3) an ADF with a hole of 4mm, an inner diameter of 5.5mm and an outer diameter of 11mm. These detectors are easily interchanged and consist of a scintillator coupled to a photomultiplier tube. The signals are then displayed on a CRT. The various detectors allow great flexibility in deciding which part of the scattered electron beam is used to form the image. The microscope is also equipped with a PEELS (Parallel Electron Energy Loss Spectroscopy) detector and the stability of the FEG allows an energy resolution of 0.2eV to be achieved.

Differential Phase Contrast (DPC) Microscopy

The presence of the PSLs allows the beam to be carefully manipulated and matched to the detectors which is necesary for DPC. The method was first proposed by Deckers and de Lang in 1974 for non-magnetic specimens but the technique was extended to magnetic materials by Chapman et al (Chapman et al, 1987, 1990; McFadyen, 1992). It relies on a quadrant detector and is set up so that when the probe does not pass through the sample, there are equal currents on each quadrant. When the specimen is present, the magnetic deflection results in an imbalance of current. By taking difference signals from opposite quadrants the induction integrated along the electron path can be deduced. The major disadvantage of this mode is that it is technically difficult to implement but it has a great advantage over the other modes discussed in that the difference signals are linearly proportional to the induction if the probe deflection is much smaller than the probe angle. It can only be implemented on a STEM, in this case the HB5, which means that the objective lens must be switched off. Since the probe is formed by one of the condensor lenses, the resolution is limited to 10nm.

2.1.9 Philips CM-20

This machine is a recent acquisition which was designed specifically for the investigation of magnetic materials. The disadvantage of DPC on the JEOL 2000-FX is that it is primarily a TEM and its STEM performance could be improved. The HB5 has the disadvantage already mentioned that the objective has to be switched off and therefore, the maximum magnification available is reduced and the resolution drops. The CM-20 aims to combine

the best features of both machines and overcome these problems. It has three lenses around the specimen area i.e. a standard immersion objective lens and two lenses at equal distances above and below the specimen which results in a field free environment at the specimen similar to that on the 2000-FX. The standard lens and the two lenses which act as a Lorentz lens may be used seperately or in conjunction. It has a thermally assisted FEG operating at an accelerating voltage of 200kV. All the modes of Lorentz microscopy previously mentioned are available on this machine.

2.2 Digital Acquisition

The Link eXL digital acquisition system allows 8 or 16-bit images to be acquired with resolutions of 256×256 or 512×512 pixels. The system scans the beam and the detected signal at each point on the image is passed to a voltage to frequency converter (VFC). This produces a frequency in the range 100Hz–5MHz with the lower value corresponding to 0V and the upper value corresponding to 1V. The frequencies are then passed to a counter which has a dwell time of 51μs resulting in a range of values between 0 and 255 (51μs×5MHz=255). The acquisition time of an 8-bit image is of the order of 10 seconds. It also allows integration of images to improve the signal to noise ratio. Multiple signals can be acquired at the same time so that when DPC is being used, different signals are fed to different channels allowing two orthogonal magnetic images and a bright field image to be recorded. These images are then in perfect registration and connections may be more easily established between microstructure and magnetic behaviour.

2.3 References

F.Bitter, *Phys.Rev.*, **38**, p1903, (1931).

J.N.Chapman, *J.Phys.D: Appl.Phys.*, **17**, pp623–647, (1984).

J.N.Chapman and G.R.Morrison, *J.Microsc.Spectrosc.Electron.*, **9**, pp329–340, (1984).

J.N.Chapman, S.McVitie and I.R.McFadyen. *Scanning Microscopy Supplement*, **1**, pp221–228, (1987).

J.N.Chapman, *Materials Science and Engineering*, **B162**, (1989).

J.N.Chapman, I.R.McFadyen and S.McVitie. *IEEE Trans.Mag.*, **26**, pp1506–1511, (1990).

C.Colliex and C.Mory, Quantitative Aspects of STEM. Proceedings of the 25th Scottish Universities Summer School in Physics. 1983.

J.M.Cowley, *Appl.Phys.Lett.*, **15**, p58, (1969).

N.H.Deckers and H.de Lang, *Optic*, **41**, p454, (1974).

J.Fidler, *Science and Technology of Nanostructured Magnetic Materials*, Edited by G. C. Hadjipanayis and G.A.Prinz, Plenum Press, New York, (1991A).

J.Fidler, *Magnetism, Magnetic Materials and their Applications, Section I*, Cuba, May, (1991B).

I.R.McFadyen and J.N.Chapman, *EMSA Bulletin*, **22.2**, pp64–75, (1992).

G.R.Morrison, PhD Thesis, University of Glasgow, (1981).

J.C.H.Spence, Experimental High-Resolution Electron Microscopy, Clarendon Press, 1981.

K.Tsuno and T.Taoka, *Jap.J.Appl.Phys.*, **22**, p1047, (1983).

Chapter 3

NdFeB

3.1 Crystalline structure

The structure of NdFeB was determined in 1984 by Givord et al and Herbst et al both using x-ray diffraction. The crystal was found to be tetragonal with a=8.8Å and c=12.2Å. It consists of 4 $Nd_2Fe_{14}B$ units per cell giving a total of 68 atoms. The Nd and B atoms are in the z=0 and z=0.5 planes whereas all but four of the Fe atoms form puckered hexagonal nets (see figure 3.1). The majority of the crystalline anisotropy arises from the 4f levels of the Nd. The lattice can be considered as two sublattices viz. the rare-earth Nd sublattice and the transition metal Fe sublattice (Franse et al 1990). These are indirectly coupled through a 4f-5d-3d interaction which allows the anisotropy of the Nd to be coupled to the strong moment of the Fe. All the moments are aligned parallel to the c-axis.

3.2 Material production

The properties of a permanent magnet are strongly influenced by its microstructure which is itself determined by the method used to prepare the material. Crystals of NdFeB can be grown using Czochralski growth but this is only useful for analysing the crystal structure and measuring the magnetic properties. It is not a practical method of large scale magnet production but more importantly, single crystals grown by this method do not exhibit hysteresis (CEAM brochure). Current production methods are aimed at producing magnets which consist of small grains of single crystal $Nd_2Fe_{14}B$ surrounded by

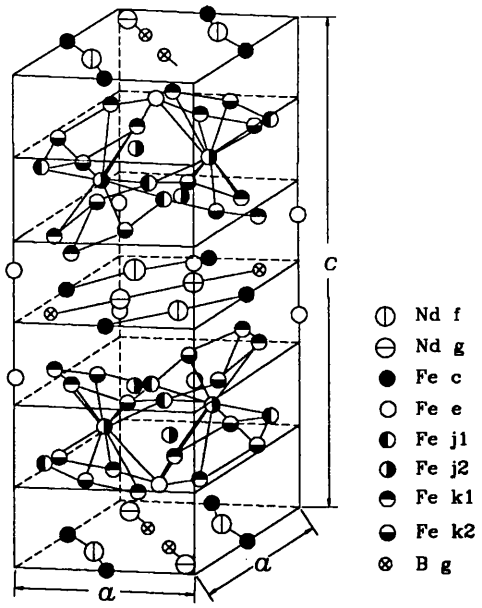

Figure 3.1: *Crystalline structure of NdFeB*

a thin layer of a Nd-rich compound which isolates the grains magnetically and prevents any magnetisation reversal spreading from one grain to another. NdFeB magnets start out as a cast alloy which contains all the required elements in the appropriate quantities. At this stage, the grain size is much larger than in the final product and the grains are randomly oriented i.e. there is no anisotropy and the material does not have very good magnetic properties. Despite this, coercivities of 0.2T have been observed in the cast alloy (Stadelmaier et al, 1983). The two most important methods of large scale magnet production are described below.

3.3 Sintered Magnets (HD route)

In this method (McGuiness et al, 1989), a mixture of N_2 and H_2 is passed over the alloy causing it to break up in an exothermic reaction. This is known as hydrogen decrepitation (HD) and is an alternative to mechanical milling. The HD process greatly reduces milling times, sintering temperatures are lower and finer grain sizes can be achieved. The presence of hydrogen reduces the opportunity for oxidation. All of this results in higher coercivities

and greater mechanical strengths. The alloy is further broken up by jet milling where air jets force the coarse powder around a circular milling chamber, the particles collide and break up into micron sized particles. As a result of their reduced mass, they move to the centre of the chamber and fall into a collection jar. The powder is very reactive at this stage and will ignite if exposed to air for any length of time, consequently, it is kept under vacuum until required. The magnets are then formed using a hydraulic press to compact the powder. This is done in a magnetic field which is used to align all the c-axes of the powder and thereby increase its final coercivity. Finally the compacts are sintered at 1000°C under vacuum for 1hr. The sintering temperature is also above the melting point of the Nd rich phase (903°C) and the subsequent liquid phase helps to increase the density from 4.2 to 7.5gmcm^{-3} and produce smooth grain boundaries. This large increase in density clearly leads to a reduction in size which must be allowed for i.e. the shrinkage in each dimension must be estimated and the compact made proportionally larger so that the final magnet is as close as possible in size to that required although some machining is usually needed to achieve the exact size. The final grain size is 5-20μm. Some magnets receive an additional heat treatment at 630°C for 1hr which helps to remove any dislocations and thereby increase the coercivity. Magnets produced by this method have $B_r \geq 1$T and energy products in the range 20-50MGOe.

3.4 Melt-spun materials

In this method (Croat et al, 1983, 1988) the cast alloy is heated until molten and ejected on to a cooled spinning copper wheel where it rapidly solidifies. This is done in an inert atmosphere since the molten rare earths are very reactive. The resulting ribbon is approximately 1-3mm wide, ~40μm thick and a length of a few mm to 1 cm depending on the wheel velocity. The final magnetic properties are determined by the quench rate which is directly related to the surface velocity of the wheel. If the melt is optimally quenched then the resulting ribbon consists of ~30nm sized crystallites. This is the theoretical critical size for a single domain particle. If the melt does not cool quickly enough then significant grain growth may occur and the grains will be large enough to behave as sintered material i.e. the grains will be multi-domain. If on the other hand, the melt is cooled

too rapidly then the grains will be too small and the coercivity and energy product will be small. These ribbons are often used to make bonded magnets by embedding flakes of ribbon in resin. They have inferior magnetic properties to sintered material since the ribbons are isotropic i.e. there is no way of aligning the grains in a particular direction. A bonded magnet prepared in this way can have B_r=0.7T and an energy product of 9MGOe. The advantage of melt spun materials is that they are cheaper and much easier to shape. Further processing techniques such as die upsetting where the magnet is subject to hot deformation can be applied to the basic ribbon to introduce an element of anisotropy (Croat et al 1988). This produces magnets with greatly improved properties e.g. B_r=1.3T and $(BH)_{max}$=40MGOe.

3.5 HDDR method

Although not yet a commercial production route, the Hydrogen, Disproportionation, Desorption and Recombination (HDDR) method (McGuiness et al, 1992) is a promising extension of the HD method. Once the HD process has taken place, the material is heated up in the hydrogen atmosphere and disproportionation of the matrix phase takes place. This reaction is reversible and so when the hydrogen is removed, the matrix phase reforms. This produces a powder with a grain size close to the single domain limit which can subsequently be used to make bonded magnets with an energy product of 18MGOe

3.6 Additions to the basic alloy

Although the material processing is of great importance, the composition of the initial alloy plays a vital role in determining the final magnetic properties. The magnetic behaviour of the NdFeB alloy arises from the Nd and the Fe. It is not believed that boron plays any part in the magnetic properties but is simply there to stabilise the compound (Sagawa et al, 1984) . A vast array of elements has been added individually and in various combinations to the basic alloy to alleviate the problems mentioned in chapter 1 (Besenicar et al, 1992; Bala et al, 1990; Kowalczyk et al, 1989; Sun et al, 1991; Szymura et al, 1991; Tokunaga et al, 1987b; Xaio et al, 1988; Xie et al, 1989;). These are divided into two classes, the first

class are those which substitute into the lattice and can therefore affect the fundamental properties of the material while the second class are dopants which form compounds and can only affect the microstructure. The dividing line is not sharp and it is possible for an element to fall into both classes e.g. Al can substitute into the lattice for Fe but it can also act as a dopant.

3.6.1 Substitutions

This class of additives is split into two sub-classes i.e rare-earths and transition metals.

Nd substitution

A rare-earth added to the basic alloy will generally subtitute for Nd in the 2:14:1 lattice. $R_2Fe_{14}B$ compounds have been made for each of the rare-earths in order to compare their properties. $Gd_2Fe_{14}B$ has the highest T_c at 661K (Herbst, 1991) but this is still poor compared to $SmCo_5$ It addition, it has a very low anisotropy ($\times$ $\sim$10 smaller than that of $Nd_2Fe_{14}B$ at 4K and half of the Nd value at room temperature) (Herbst, 1991). The highest anisotropies are provided by R=Tb and R=Dy but these couple antiferromagnetically to Fe having average magnetic moments of -9.1μ_B and -10.1μ_B respectively as compared to 3.2μ_B for R=Nd. Consequently, the highest net moment of any $R_2Fe_{14}B$ compound is provided by R=Nd but the room temperature anisotropy is less than half that of the R=Tb and R=Dy compounds (Xaio et al, 1988). $Pr_2Fe_{14}B$ has a slightly higher anisotropy than that of $Nd_2Fe_{14}B$ but has slightly lower M_s and $(BH)_{max}$. On a more practical level, Pr is less abundant than Nd and hence more expensive.

Fe substitution

Elemental iron has a Curie temperature of 1043K which is at least 200K higher than any $R_2Fe_{14}B$ compound and therefore much work has been done to enhance T_c. T_c is determined by the Fe sublattice and so much work has concentrated on Fe replacements. The only element which can replace Fe over the whole concentration range (x=0–14) in $Nd_2Fe_{14-x}Co_xB$ is Co and this produces the best enhancement of the Curie temperature with $Nd_2Co_{14}B$ having $T_c \simeq$1000K but since research into 2:14:1 magnets was prompted

by the shortage of Co this is a somewhat retrograde step. All others elements tried have only partially substituted for Fe. Ga, Ni, Sc and Si enhance T_c but lead to a reduction in M_s whereas Al, Cr and Ru degrade T_c severely. The RT value of M_s for $Nd_2Fe_{14-x}Co_xB$ has a maximum at x=2 (Herbst, 1991). It has been observed that increasing values of x lead to a reduction in the anisotropy field. It has also been observed that substitution of 10 at% Co for Fe reduces the temperature coefficients α and β to -0.09%/°C and 0.54%/°C respectively (Xaio, 1991).

3.6.2 Dopants

The addition of dopants has been observed to improve the bulk magnetic properties but since they do not substitute into the lattice, their effect must be microstructural. Fidler (1991) has separated the dopants into two types.

Type 1

Type 1 are those which form Nd-containing intergranular phases such as Al, Ga, Cu, Ge or Sn. These new phases have a lower melting point than the usual Nd rich phase (Sagawa, 1984) which increases the wetting of the grains by the liquid phase at the sintering temperature. This improves the magnetic isolation of the grains with a consequent increase in the coercivity. The addition of type 1 dopants also leads to an improvement in the corrosion resistance of the material, since the Nd, having already formed compounds, is less easily oxidised. Xiao et al (1988) showed that addition of Al produced a magnet with values of α and β larger than the basic alloy and its ability to improve the coercivity must be offset against this.

Type 2

Type 2 are those which form boride phases such as V, Mo, W, Nb or Ti. Yin et al (1992) have studied NdFeB with additions of V and have observed two types of precipitates ranging in size from 0.1μm to several μm embedded in both the intergranular phase and the matrix grains. They deduced that these were both borides i.e. V-boride and V-Fe-boride.

Nb ($\leq$1at%) is observed to enhance the bulk magnetic properties but the reasons for this are not fully understood (Allibert, 1989; Parker et al, 1987A; Parker et al 1987B; Tokunaga, 1987a). It forms small ($\sim$50nm) precipitates which have been observed to pin the domain walls (Sagawa et al, 1984), but only in applied fields up to 0.5T. This pinning effect cannot be strong enough to produce any significant increase in coercivity but Nb does appear to inhibit grain growth during sintering which increases coercivity. Weizhong et al (1991) fabricated samples from powders milled for different lengths of time leading to samples with different grain sizes ranging from 7–16μm. They observed a clear inverse relationship between grain size and intrinsic coercivity and proposed that larger grains impose a larger field on their neighbouring grains leading to a reduction in coercivity. Higher levels of Nb (up to 3%) do not lead to a deterioration of the magnetic properties but above that, the proportion of the 2:14:1 phase decreases and is replaced by the soft magnetic 2:17 phase (Xaio et al, 1988).

3.7 Materials in this project

The samples investigated in this project were produced by the sintering method and had compositions as follows

Sample A $Nd_{15.5}Fe_{76.7}B_{7.34}Nb_{0.36}$

Sample B $Nd_{13.5}Fe_{74.7}B_{7.44}Dy_{2.6}Nb_{0.5}Al_{1.3}$

A third sample, C, had the same composition as B but had not been subject to the heat treatment given to B. Table 3.1 shows the properties of each sample as well as those of $SmCo_5$ for comparison It is clear from table 3.1, that apart from the Curie temperature, NdFeB offers great improvements over SmCo. Coercivities three times greater than and energy products twice that of SmCo can be obtained (although unfortunately not yet at the same time). The addition of Dy to the alloy has increased the coercivity to greater than 4 times its base value although at the expense of a $\sim$10% drop in the saturation magnetisation. Figures 3.2, 3.3 and 3.4 show the hysteresis loops for each of the samples measured at the University of Sheffield using a VSM with a superconducting magnet and a maximum field of 5T. It is clear from the rapid rise of the initial magnetisation curves

Bulk property	Sample A	Sample B	Sample C	$SmCo_5$
M_s(T)	1.34	1.16	1.14	0.98
M_r(T)	1.21	1.00	1.06	0.95
H_c(T)	0.73	2.89	1.96	0.87
$(BH)_{max}$(MGOe)	35.4	25.2	26.1	20.1
T_c(K)	585	~700	~700	993

Table 3.1: *Properties of samples A, B, C and $SmCo_5$*

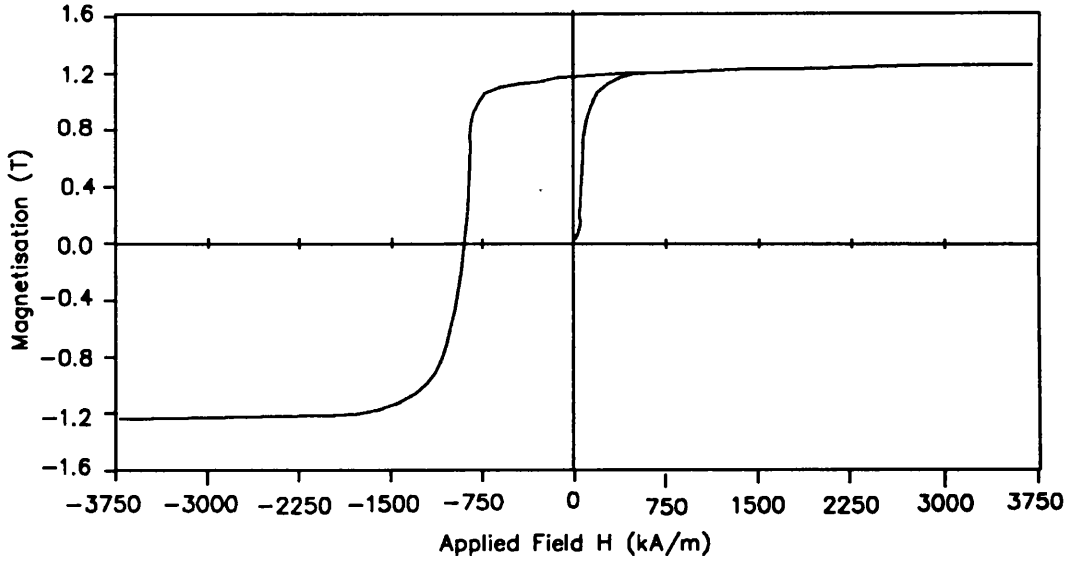

Figure 3.2: *Hysteresis loop for material A*

that the coercivity mechanism is dominated by the nucleation of reverse domains.

3.8 Corrosion in RE-TM magnets

Rare-earth magnets suffer greatly from corrosion and this, in conjunction with their low Curie temperature and their high cost, has limited their widespread use. The primary problem is the reactivity of the rare earth materials which means that the Nd oxidises very easily. This results in an apparent excess of Fe which appears as α-Fe on the suface of the material which, because it is magnetically soft, reduces the coercivity. Although the addition of dopants tends to improve the corrosion resistance, the improvement is not

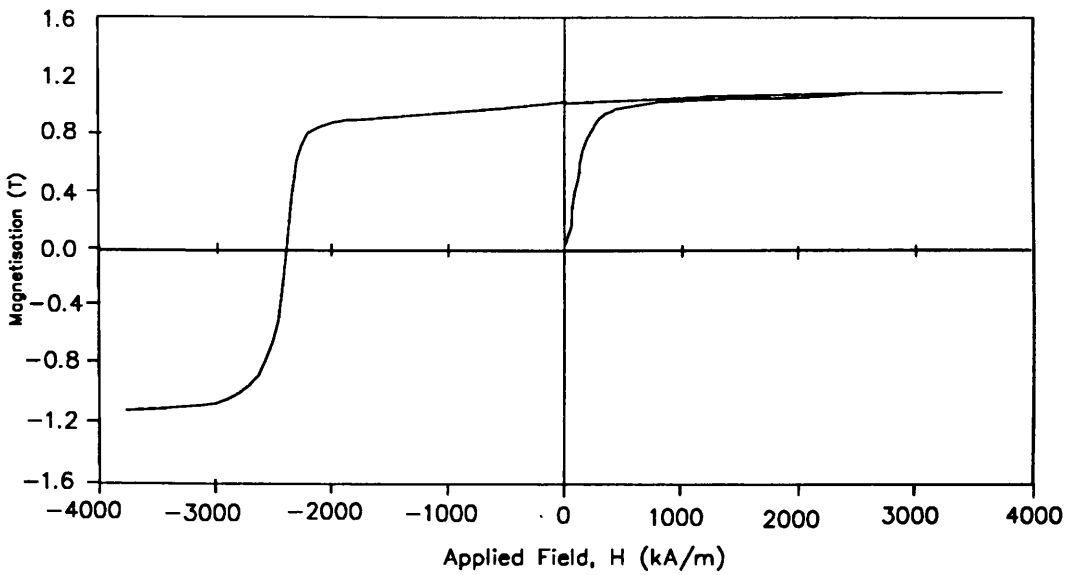

Figure 3.3: *Hysteresis loop for material B*

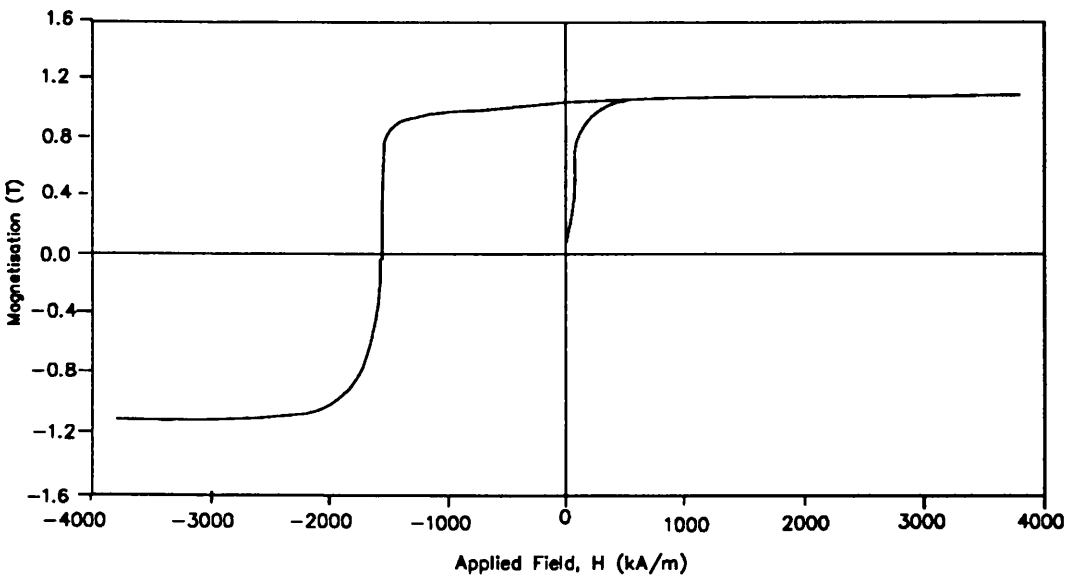

Figure 3.4: *Hysteresis loop for material C*

sufficient to enable them to be used without some further protection. The most common method to counter this problem is to coat the magnets in another material e.g. Ni. This requires pretreatment of the magnet to ensure that the Ni adheres. A soda-silica glass treatment has been found to give good results with melt-spun materials

3.9 TEM Specimen Preparation

The two most important requirements of a TEM sample are that it should transmit electrons at the working accelerating voltage and that it should be in a suitable form to fit in the specimen holder, in this case 3mm discs with a maximum height of $\sim 200\mu m$ (this height requirement is only important in the VG HB5). The material supplied came in the form of standard production components which were generally discs of diameter 25mm and height 2-5mm. The powder had been aligned normal to the plane of the disc. Initially, the discs were sliced either parallel or perpendicular to the alignment direction using a rotating diamond saw to produce slices of thickness 300-500μm. These slices were stuck to a glass slide using wax and mechanically ground using 220 grade silicon carbide paper until they were $\sim 200\mu m$ thick. This grade of paper is very coarse and leaves many scratches on the sample which are removed using 400 and then 600 grade paper. This helps to polish the surface and removes the scratches which may cause the sample to break at a later stage. The slices were turned over and ground and polished to a thickness of $\sim 150\mu m$. An ultrasonic drill was used to cut 3mm discs from the slices. The cutting action is provided by the vibrating drill bit and 240 grade carborundum powder. The discs are then cleaned of all wax using inhibisol. Since the material consists of a compacted powder, the ultrasonic drill tends to roughen the surface of the discs by simply shaking them to pieces, these surfaces must be polished in order to reduce channelling effects in the ion beam thinning process i.e. where there is preferential thinning along a topographical feature. This is done using a dimple grinder. The dimple grinder has a grinding wheel rotating in the vertical plane which rests on the sample which itself rotates in the horizontal plane, the grinding is produced by diamond paste (in this case 3μm paste). The edge of the grinding wheel orthogonal to the plane of the wheel is usually curved with a radius equal to that of the wheel itself and the grinding action produces a dimple of increasing depth and radius.

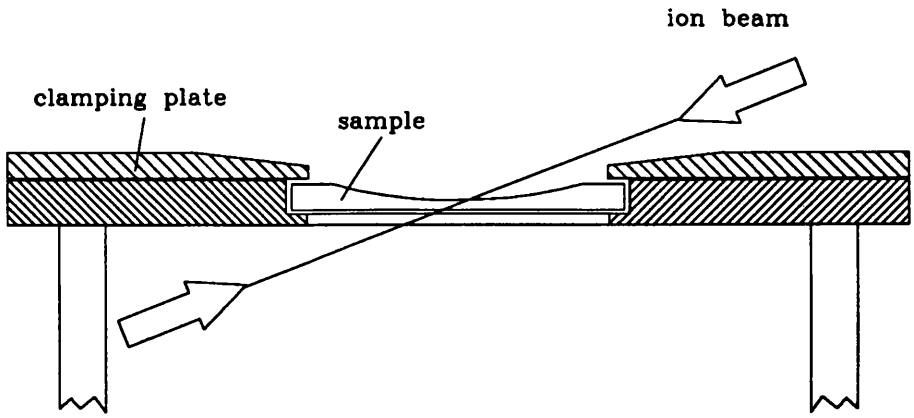

Figure 3.5: *Schematic of specimen and specimen stage*

The advantage of this method is that the end product is a disc whose thickness at the centre is $\sim 30\mu$m but with edges thick enough to support itself and to allow handling. This also avoids the use of supporting washers. In the first instance, a 15mm diameter wheel with a flat edge of width 3mm was used to polish one surface, this simply polishes the surface flat and removes the damage caused by the ultrasonic drill. The opposite side is dimpled using a standard 20mm wheel. The increased wheel diameter means that lower thinning angles can be used. All wax is cleaned from the sample using inhibisol since after the ion beam thinning, the sample will be too fragile to withstand much cleaning. The thinning is done on a Gatan Duomill which has two thinning stages each of which can be liquid nitrogen cooled to reduce beam induced damage. The majority of specimens were cooled although no major differences were observed between those that were and those that were not. Each stage has two argon ion guns which can be rotated in the vertical plane so that they are both at the same angle to the plane of the specimen (which is in the horizontal plane) The specimen is lightly clamped to increase thermal contact and to keep the sample fixed in the holder (see figure 3.5). The machine is operated in current limited mode where the gun voltages are kept fixed and the gun current is monitored to take account of any temperature change and/or erosion of the cathode aperture. This usually means that the gun current drops slowly throughout the thinning process and the gas flow has to be increased at regular intervals in order to maintain the desired value.

The Duomill also has a laser terminator which illuminates the sample from above and has a sensor below which trips at a predetermined light level. When the sample has been holed by the ion beams the machine shuts down. The sensitivity of this device can be varied to determine at what light level the sensor trips but here it was generally operated at its most sensitive since this produces a greater useful area in the centre of the specimen without there necessarily being a hole which is visible to the naked eye. It is preferable to keep the operating voltage low to minimise the damage which would result from highly energetic Ar ions. All the specimens were thinned at a voltage of 4-5kV with a gun current in each gun of 0.5mA. The Duomill has a specimen current monitor which measures the current falling on the specimen but this is not reliable since it depends on the conductivity of the sample and the electrical contact between it and the specimen stage, both of which would be affected if there were any residual wax on the specimen. This was not a problem since there was no evidence of beam induced damage. Clearly, the angle of the guns will have an effect on the thinning rate, the higher the angle the greater the thinning rate but the smaller the area which will be thinned. Since it is desirable to maximise the thinned area, the gun angle was set at a shallow angle. The minimum angle available is determined by the shadow effect of the specimen clamping plate i.e. below a certain angle, the beam will ion beam thin the plate instead of the sample. In order to optimise the thinning time, the angle of the guns was set to $\sim 15°$ until the specimen had been holed and it was then given a further half hour thinning at a reduced angle of $\sim 13°$ in order to try to maximise the usable area. Typical thinning rates were $\sim 4\text{–}5 \mu m h^{-1}$.

The electron transparent areas were close to the hole and in practice were found to extend to a distance of 1-2 grain diameters from the edge of the hole. There is an inevitable thickness variation across the grains as a result of the preparation method but this was not found to be significant for the experiments undertaken. This will be discussed further in chapters 4 and 5.

3.10 References

Advances in Permanent Magnet Technology, Concerted European Action on Magnets (CEAM) brochure.

C.H.Allibert, *J.Less Common Metals*,**152**, L1 (1989).

H.Bala, S.Szymura, Y.M.Rabinovich, V.V.Sergeev, G.Pawlowska and D.V.Porowskii, *Revue Phys.Appl.*, **25**, pp1205–1211, (1990).

S.Besenicar, B.Saje, G.Drazic and J.Holc, *J.Mag.Mag.Mat.*, **104–107**, pp1175–1178, (1992).

J.J.Croat, J.F.Herbst, R.W.Lee and F.E.Pinkerton, *Appl.Phys.Lett.*, **44**, pp148–149, (1983).

J.J.Croat, J.F.Herbst, R.W.Lee and F.E.Pinkerton, *J.Appl.Phys.*, **55**, p2078, (1988).

J.Fidler and J.Bernadi, Proceedings of the Second International Symposium on Physics of Magnetic Materials Vol 2, (1992).

J.Fidler, paper presented at Magnetism, Magnetic Materials and their applications, Cuba (1991).

J.J.M.Franse, R.J.Radwanski and R.Verhoef, *J.Mag.Mag.Mat.*, **84**, pp299–308, (1990).

D.Givord, H.S.Li and J.M.Moreau, *Solid State Comms.*, **50**, 6, pp497–499, (1984).

J.F.Herbst, J.J.Croat, F.E.Pinkerton and W.B.Yelon, *Phys.Rev.B*, **29**, 7, pp4176–4178, (1984).

J.F.Herbst, *Rev.Mod.Phys.*, **63**, pp819–898, (1991).

T.Ishikawa, Y.Hamada and K.Ohmori, Paper No 19P0212 10th International Conference on Rare-Earth Magnets and Their Applications (1989).

L.Jinfan, L.Helie and W.Jiang,*J.Mag.Mag.Mat.*, **103**, p65, (1992).

A.Kowalczyk, P.Stefanski and A.Wrzenciono, *J.Mag.Mag.Mat.*, **79**, pp109–112, (1989).

P.J.McGuiness, E.J.Devlin, I.R.Harris, E.Rozendaal and J.Ormerod, *J.Mater.Sci.*, **24**, p2541, (1989).

P.J.McGuiness, X.J.Zhang, K.G.Knoch, X.J.Yin, M.J.Wyborn and I.R.Harris, *J.Mag.Mag.Mat.* **104–107**, pp1169–1170, (1992).

S.F.H.Parker, R.J.Pollard, D.G.Lord and P.J.Grundy, *IEEE Trans.Mag.*, **MAG-23**, p2103, (1987A).

S.F.H.Parker, P.J.Grundy and J.Fidler, *J.Mag.Mag.Mat.*, **66**, p74, (1987B).

M.Sagawa, S.Fujimura, N.Togawa, H.Yamamoto and Y.Matsuura, *J.Appl.Phys.*, **55**, pp2083–2087, (1984).

H.H.Stadelmaier, N.A.El-Masry and S.Cheng, *Materials Lett.*, **2**, pp169–172, (1983).

X.K.Sun, G.F.Zhou, Y.C.Chuang, R.Grossinger and H.R.Kirchmayer, *J.Mag.Mag.Mat.* **96**, pp197–205, (1991).

S.Szymura, H.Bala, Y.M.Rabinovich, V.V.Sergeev and G.Pawlowska, *J.Mag.Mag.Mat.*, **94**, pp113–118, (1991).

M.Tokunaga, H.Harada and S.R.Trout, *IEEE Trans.Mag.*, **MAG-23**, p2284, (1987a).

M.Tokunaga, H.Kogure, M.Endoh and H.Harada, *IEEE Trans.Mag.*, **MAG-23**, pp2287–2289, (1987b).

T.Weizhong, Z.Shouzeng and H.Bing, *J.Mag.Mag.Mat.* **94**, pp67–73, (1991).

J.Q.Xie, C.H.Wu, Y.C.Chuang and F.M.Yang, *Solid State Comms.*, **71**, pp329–332, (1989).

Y.Xaio, S.Liu, H.F.Mildrum, K.J.Strnat and A.E.Ray, *J.Appl.Phys.*, **63**, pp3516–3518, (1988).

X.J.Yin, I.P.Jones and I.R.Harris, *J.Mag.Mag.Mat.* **116**, ppL325–L335, (1992).

Chapter 4

TEM Investigations of NdFeB

4.1 Experimental Conditions

All of the work in this chapter was done on the JEOL-2000FX. The first samples investigated were prepared with the plane of the sample perpendicular to the alignment field - figure 4.1 is a schematic of the bulk material showing how the samples were cut from it. The high saturation magnetisation meant that Fresnel and Foucault images were relatively easy to obtain under any conditions but the work was generally undertaken using a condensor aperture of 120μm and a spot size of 2. This produced a beam where the spot size was less than the Lorentz deflection while also giving acceptable illumination levels.

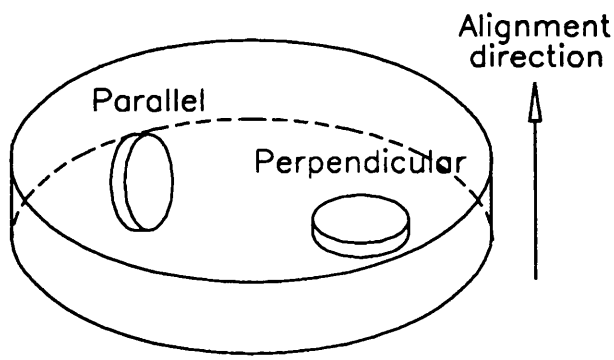

Figure 4.1: *Schematic showing orientation of TEM samples with respect to the bulk material and the alignment direction*

The images of the sample were taken using x-ray reflex film which allowed the exposure to be only a few seconds at a magnification of ×26K. Exposure times were determined using the current meter which is integral to the small viewing screen since the use of the faster film means that the auto-exposure system will greatly over expose the film. The current density for a Foucault image under the illumination conditions discussed was $\sim$1pAcm^{-2} which requires an exposure time of 4 seconds. For bright field and Fresnel images, the illumination may easily be varied using the condensor lens but was usually set to be $\sim$1pAcm^{-2}. Fresnel images were obtained with an objective defocus of approximately 12μm as determined from the JEOL calibration of the focus. For the diffraction patterns, the sample was adjusted to be at the eucentric height and a 100μm SAA was inserted. The spot size was reduced to 3 to minimise the size of the diffraction spots and prevent the pattern being overexposed (at spot size 1, even the shortest exposure time available can lead to overexposure in the thinner areas of the sample). The microscope was switched to diffraction mode and the goniometer tilt (θ_G) was varied until a clear single crystal diffraction pattern was obtained i.e. a zone axis was found. Diffraction patterns (DPs) were recorded as close to $\theta_G = 0°$ as possible for reasons discussed in section 4.3. The goniometer tilt was also recorded for each pattern. Generally three diffraction patterns were taken at exposures of 0.5, 1 and 2.8 seconds. The patterns were all taken at a nominal camera length of 40cm in order that as much of the pattern as possible could be recorded without the spots being too close together. Diffraction patterns were obtained from single crystal Au and polycrystalline Ni so that the camera length could be calibrated.

4.2 Magnetic Structure and Behaviour

Figure 4.2 shows a bright field image of material A taken on the 2000FX with a diffraction aperture to enhance the contrast. The grain structure of the material is apparent with a grain size in the range 3–10μm The micrographs in figure 4.3 are a Fresnel/Foucault pair of the same area of material A. These micrographs illustrate many points which will be dealt with in depth in the next sections. The pictures show four grains with the grain boundary between the two central grains being very clear. As described in chapter 2, the Fresnel image highlights the domain walls as narrow alternate black/white

Figure 4.2: *Bright field image of material A*

bands. The Foucault image shows the domains alternately dark and bright. The series of micrographs in figure 4.4 shows Foucault images of a number of grains all taken at the same magnification. The variation in the domain widths is quite clear and it can be seen that in the first image, the domains are relatively narrow and the walls have little directional preference in the plane of the sample. This tendency to meander is reduced as the domain width increases and the last image shows domains which are much wider with fairly straight walls.

4.3 Diffraction Patterns

Figure 4.5(a) shows an electron diffraction pattern of a grain. The grain is clearly single crystal as expected. The calibration of the camera length produced a value of 1.42±0.01m (the great difference between this value and the nominal camera length of 40cm is due to the software on the JEOL-2000FX not being calibrated for the modified polepiece). It was assumed that the grains were tetragonal 2:14:1 and that the lattice constants are a=8.80Å and c=12.19Å (Givord et al, 1984; Herbst et al, 1984). Figure 4.6 shows a schematic of the diffraction pattern which has been indexed. Determination of the zone axis from the DP is straightforward and the inclination of the c-axis with respect to the beam (θ_B) follows through simple trigonometry. Figure 4.7 is a schematic of a single grain. The axis of rotation of the goniometer and hence the grain is the y-axis, the beam is in the negative z direction and **n** is the sample normal. The angle between the c-axis and the sample normal, θ, is fixed but, as the diagram shows, its inclination with respect to the beam will vary with the goniometer tilt, θ_G. It can be seen that;

$$\theta_B - \theta_G \leq \theta \leq \theta_B + \theta_G \tag{4.1}$$

As a consequence, the goniometer tilt was kept as low as possible - generally $< 5°$. The second DP (4.5 (b)) again shows a single crystal material but also contains polycrystalline rings. These rings are too diffuse to index accurately but are very close to the d-spacings expected for α-Fe as seen by other researchers (Parker et al, 1987). As mentioned in chapter 1 this arises as a result of the Nd oxidising, leaving an apparent excess of Fe which shows up as α-Fe. The measured d-spacing of the first ring is 2.03±0.01Å which agrees

Figure 4.3: *Fresnel/Foucault pair of 4 grains*

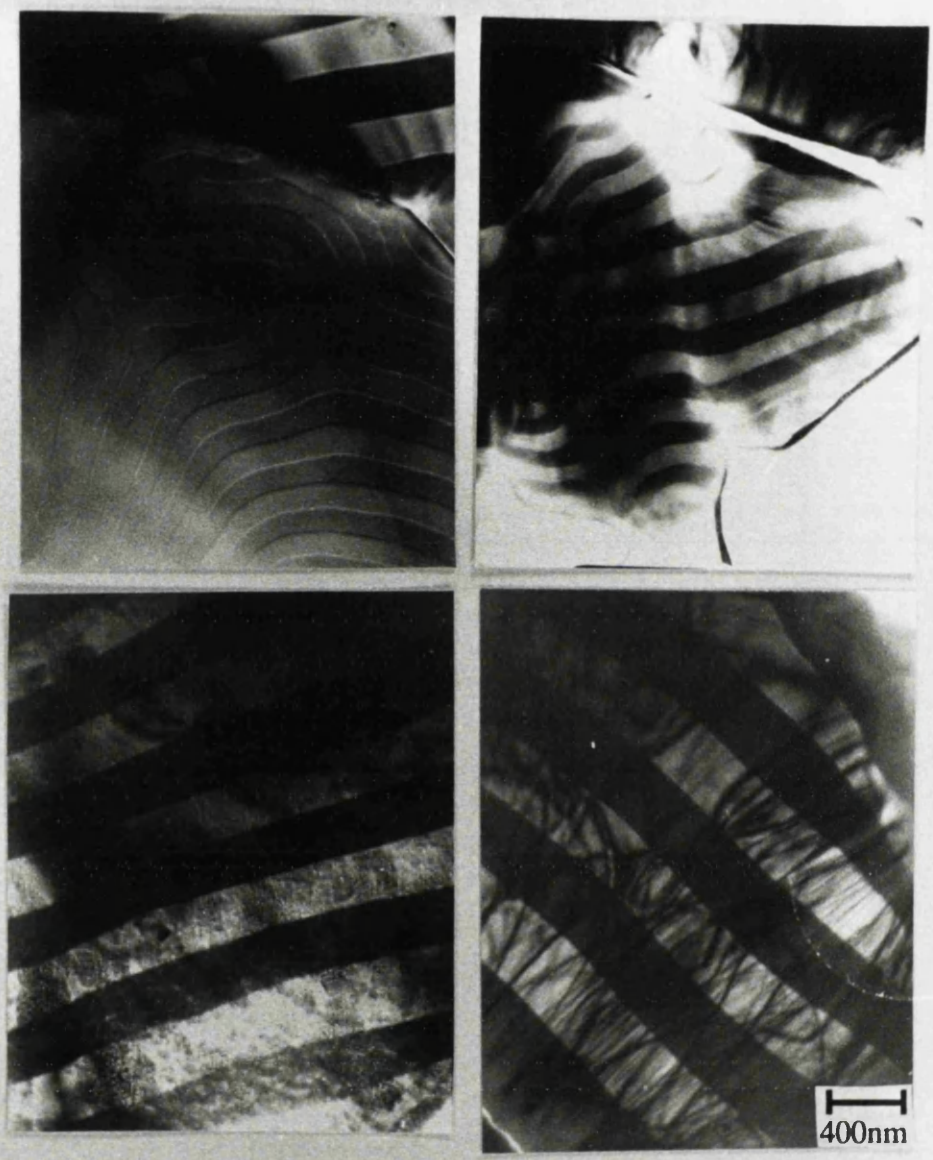

Figure 4.4: *Various Foucault images*

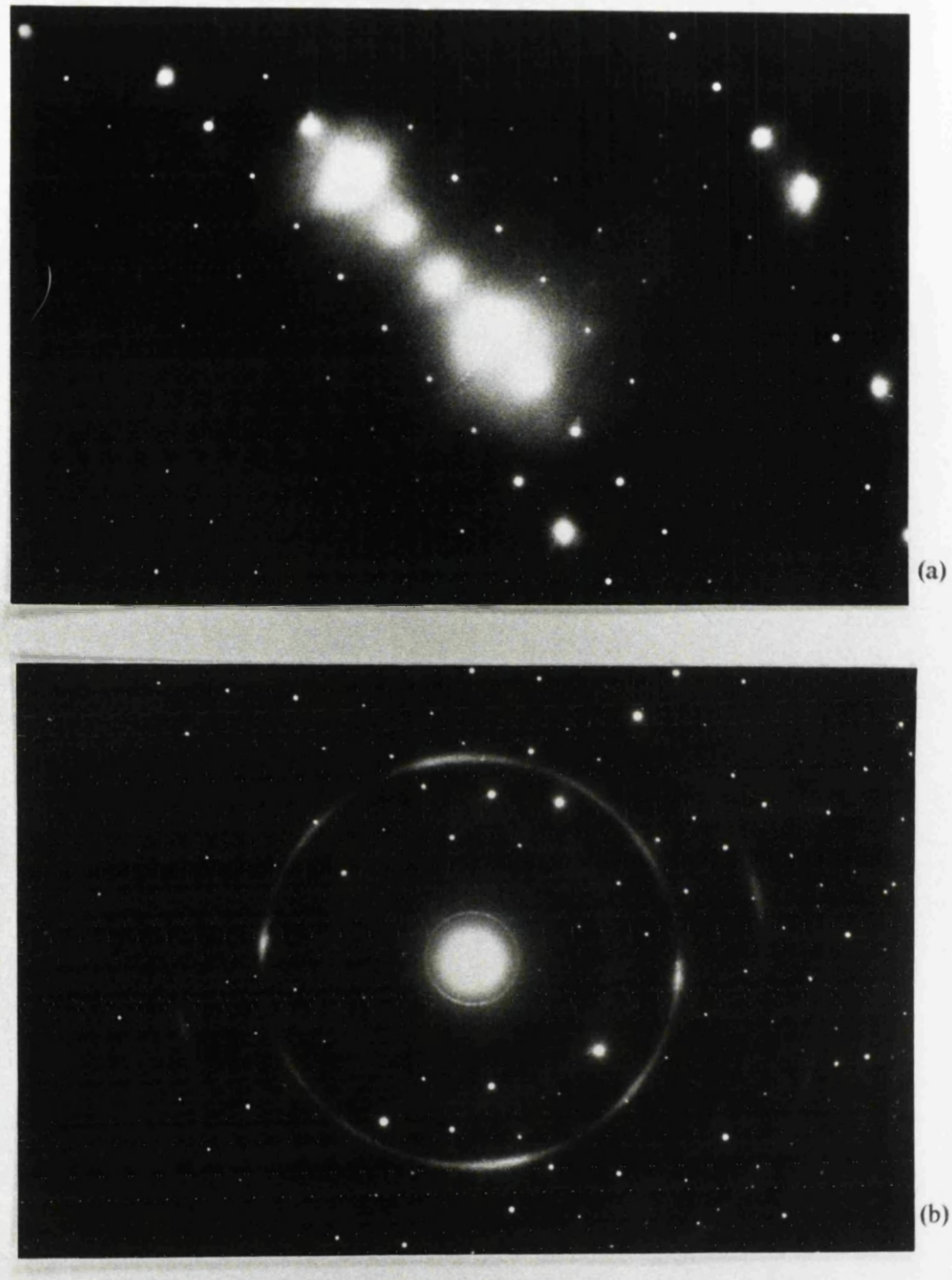

Figure 4.5: *(a) A typical diffraction pattern from material A. (b) A typical diffraction pattern from material A showing α-Fe*

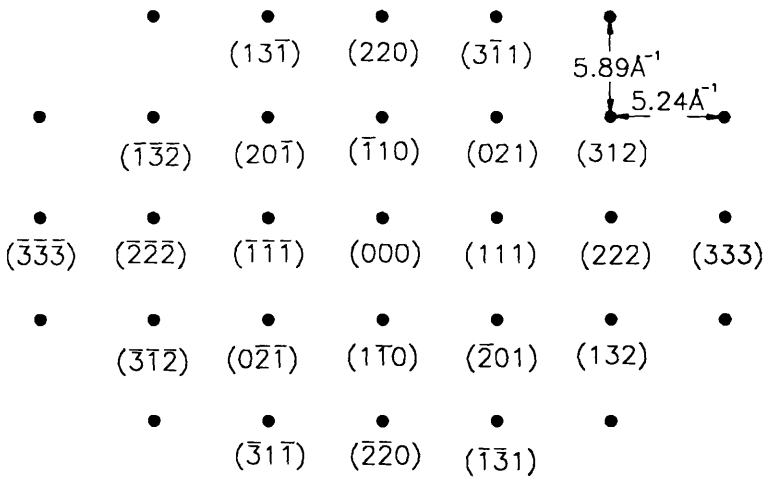

Figure 4.6: *Schematic of diffraction pattern*

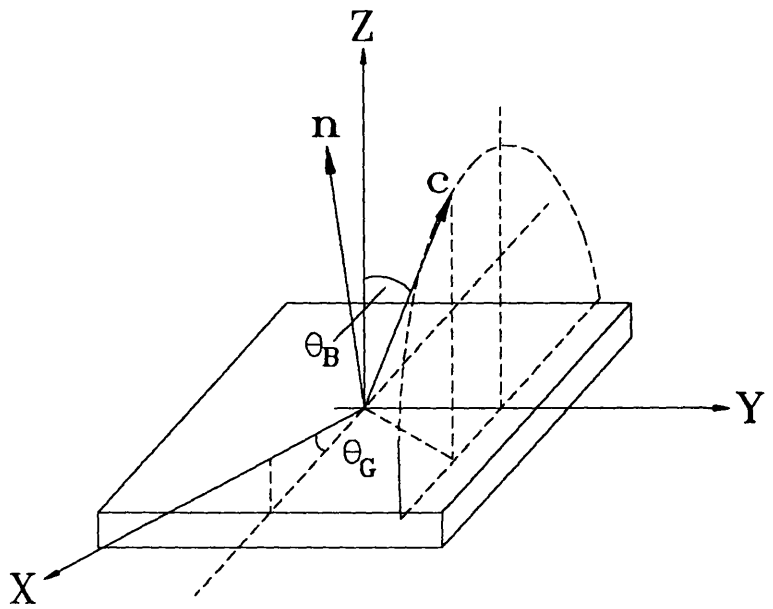

Figure 4.7: *Schematic showing geometry of individual grain and goniometer*

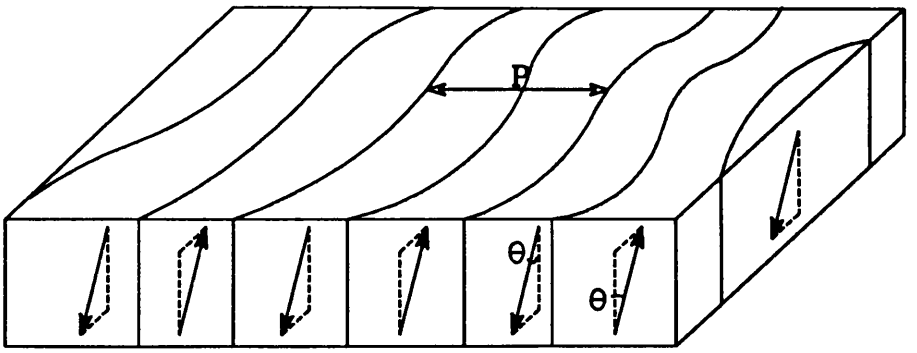

Figure 4.8: *Schematic of grain with small θ*

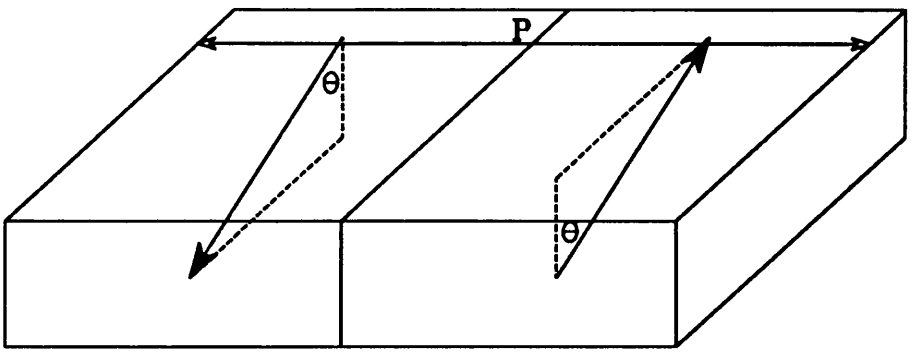

Figure 4.9: *Schematic of grain with large θ*

well with the accepted value of 2.027Å.

As introduced in chapter 1, the magnetic structure arises as a result of the system trying to minimise its energy. All of the observed structures can be explained in terms of this. The orientation of the c-axis relative to the sample normal is very important since the large anisotropy will mean that the magnetisation will essentially be parallel to the c-axis; therefore, the magnetostatic energy will be strongly influenced by its orientation Figure 4.8 is a schematic diagram of a grain with θ small i.e. the main component of anisotropy is directed out of the plane of the sample and there is only a small directional preference within the plane of the sample. The large magnetocrystalline anisotropy of NdFeB results in a significant component of anisotropy within the plane of the sample even at small θ and some directionality will be inevitable. Reduction of the magnetostatic

energy is brought about by the formation of domains leading to a small domain period. The next diagram (figure 4.9) is a schematic of a grain with a much larger value of θ. There are far fewer free poles at the surface leading to a smaller value of magnetostatic energy and so domains will not be formed since this would increase the wall energy unnecessarily. The moments will tend to align in a direction which is in the plane of the sample and so the walls are very straight with a clearly defined direction.

4.4 Parallel Samples

Figure 4.10 shows a micrograph, obtained at the same magnification, of a sample of material A whose plane is parallel to the alignment direction. It is clear that the domains are very much wider than those observed in the perpendicular samples with a period in this case of 2.8μm (this is deduced by doubling the width of a single domain since only one domain can be seen). This increased width is consistent with the previous discussion since the majority of moments in this sample would be expected to lie in the plane of the sample. In addition, the finite size of the grains must now be taken into consideration when the system is minimising its energy. The domain structure will, as a result, not be at a true equilbrium and as will be discussed in much greater detail in chapter 5, little further information can be deduced from samples prepared in this orientation.

4.5 Variation of P with θ

The nature of the material preparation results in there being a spread of grain orientations centred around the alignment direction (Miyajima et al, 1992). This meant that the variation of P with θ could be easily investigated by studying various grains within the same sample. For each of the materials A, B and C, a series of sets of micrographs was obtained from various grains consisting of a BF image, a Foucault image and a DP. The average domain period, P, was measured directly from the micrograph and the diffraction patterns were indexed to find θ. The accuracy of θ was assumed to be $\pm 5°$ and that of P to be $\pm$10nm.

Figures 4.11, 4.12 and 4.13 shows the data from all three materials. It is clear that as

Figure 4.10: *Micrograph of a parallel sample of material A*

θ increases, P increases which is expected from the earlier discussion. The rate of increase appears to be different but the significance of this is unclear. All the θ values lie between 10° and 50°. As would be expected, the alignment of the moments is strongly affected by the field applied during pressing (Jahn et al, 1991). Miyajima et al (1991) found that even in an alignment field of 1T, the moments are distributed in a cone with a semi-angle of 33° and at lower fields, this angle can be as large as 82°. They proposed that this angle could be calculated using an alignment parameter, η which is defined as the ratio between the remanence and the saturation magnetisation. The value of the semi-angle, Ω, is deduced from the equation;

$$\eta = \frac{(1 + \cos \Omega)}{2} \tag{4.2}$$

which for the values of M_s and M_r given in chapter three leads to a value of $\Omega = 58°$ for sample A which agrees well with the observations. There is no obvious explanation as to why very few grains with $\theta \approx 0°$ were observed. In a normal distribution of c-axes, the probability of finding a grain with the c-axis between θ and $\theta + d\theta$ is proportional to $\sin\theta d\theta$. This would imply that the probability of finding grains with $\theta \approx 0°$ is small. Inspection of the graph reveals that for a given value of θ, the corresponding values of P for materials B and C are consistently higher than those for material A. Further analysis of these data is given in chapter 5.

4.6 Domain Wall Behaviour at Grain Boundaries

The behaviour of domain walls at grain boundaries is of great importance in determining the magnetic properties of the bulk material. As discussed in chapter 3, it is preferable that each grain is magnetically independent so that any domain reversal within one grain will not spread to others and lead to a partial or full demagnetisation of the material.

Images were taken of domain walls at grain boundaries in materials A and B and the photgraphs in figure 4.14 show some of the types of behaviour observed. ϕ_1 and ϕ_2 are defined to be the orientation of the domains within the plane of the sample.

4.14(a): In the first micrograph, $\theta_1 \approx \theta_2$ which is apparent from the similar domain sizes. $\mid \phi_1 - \phi_2 \mid \approx 0°$ and the boundary is orthogonal to both sets of domains. The domains appear to cross the boundary with negligible perturbation.

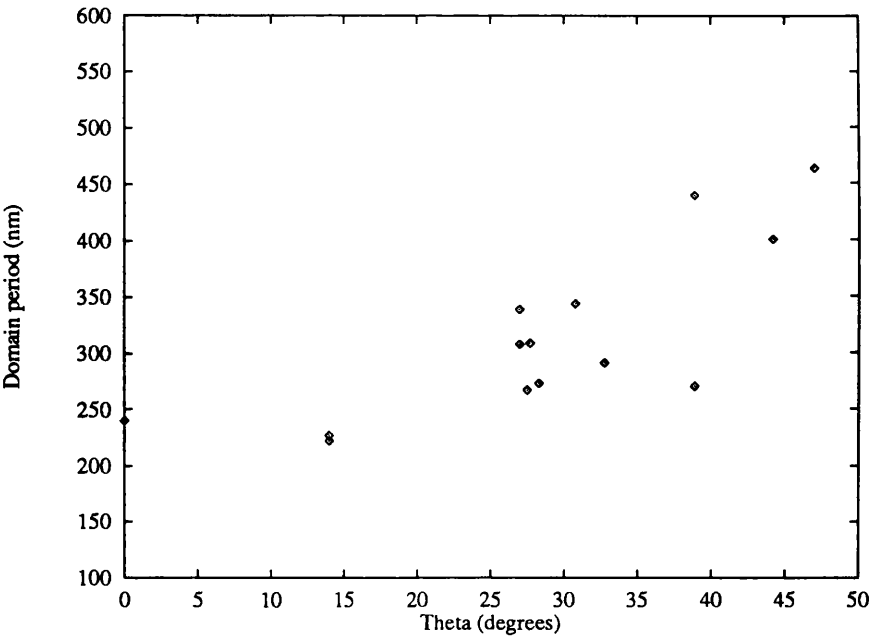

Figure 4.11: *Variation of p with θ for material A*

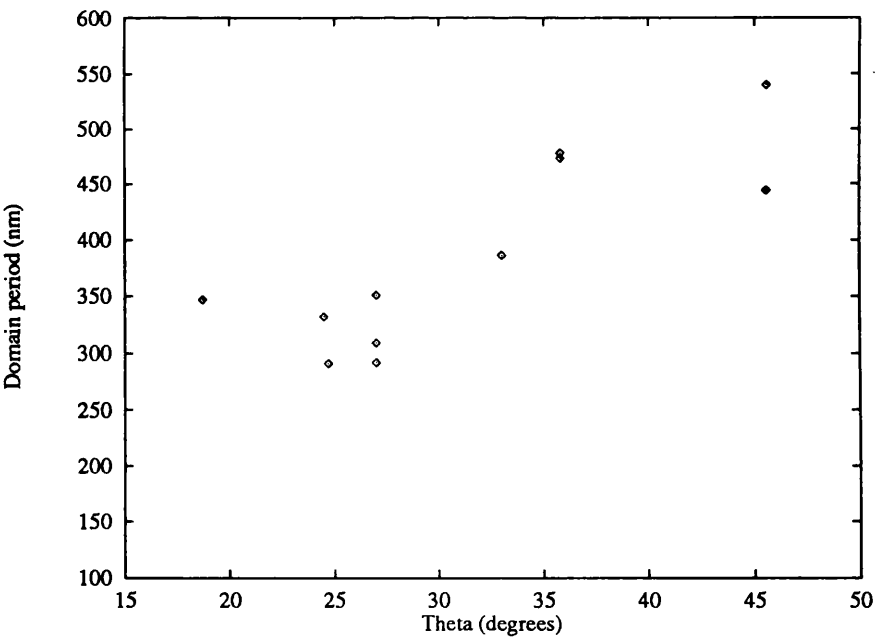

Figure 4.12: *Variation of p with θ for material B*

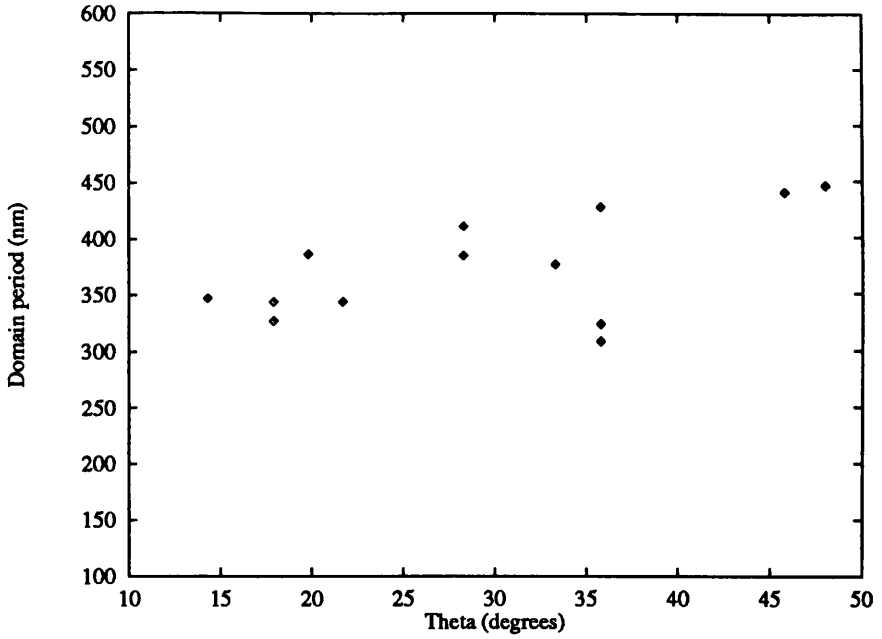

Figure 4.13: *Variation of p with θ for material C*

4.14(b): θ_1 and θ_2 are no longer similar and $\mid \phi_1 - \phi_2 \mid \approx 45°$. The boundary, though its orientation with respect to the domains varies, is essentially orthogonal to one set of domains and at 45° to the other. The domain structure appears to be continuous but it is very distorted at the boundary in order to accommodate this boundary.

4.14(c): θ_1 and θ_2 are again similar but small; $\mid \phi_1 - \phi_2 \mid \approx 90°$ and the boundary runs parallel to one set of domains. It can be seen that alternate domains in the upper grain terminate before the boundary. Although the variation in contrast at the boundary in the upper grain suggests there is no simple explanation for the behaviour of the domains, it clear that the 'darker' of the domains in each grain are on either side of the boundary. This would result in excess magnetostatic energy at the boundary if these domains were similarly magnetised but the horizontal mapping direction obsures the fact that their vertical components are oppositely directed. Figure 4.15 shows this schematically; the enlarged areas show how there would be an excess of magnetostatic energy if the domain walls were to continue right to the grain boundary and how the system reduces this excess.

4.14(d): θ_1 and θ_2 small, $\mid \phi_1 - \phi_2 \mid \approx 90°$. This situation is similar to case (b), but

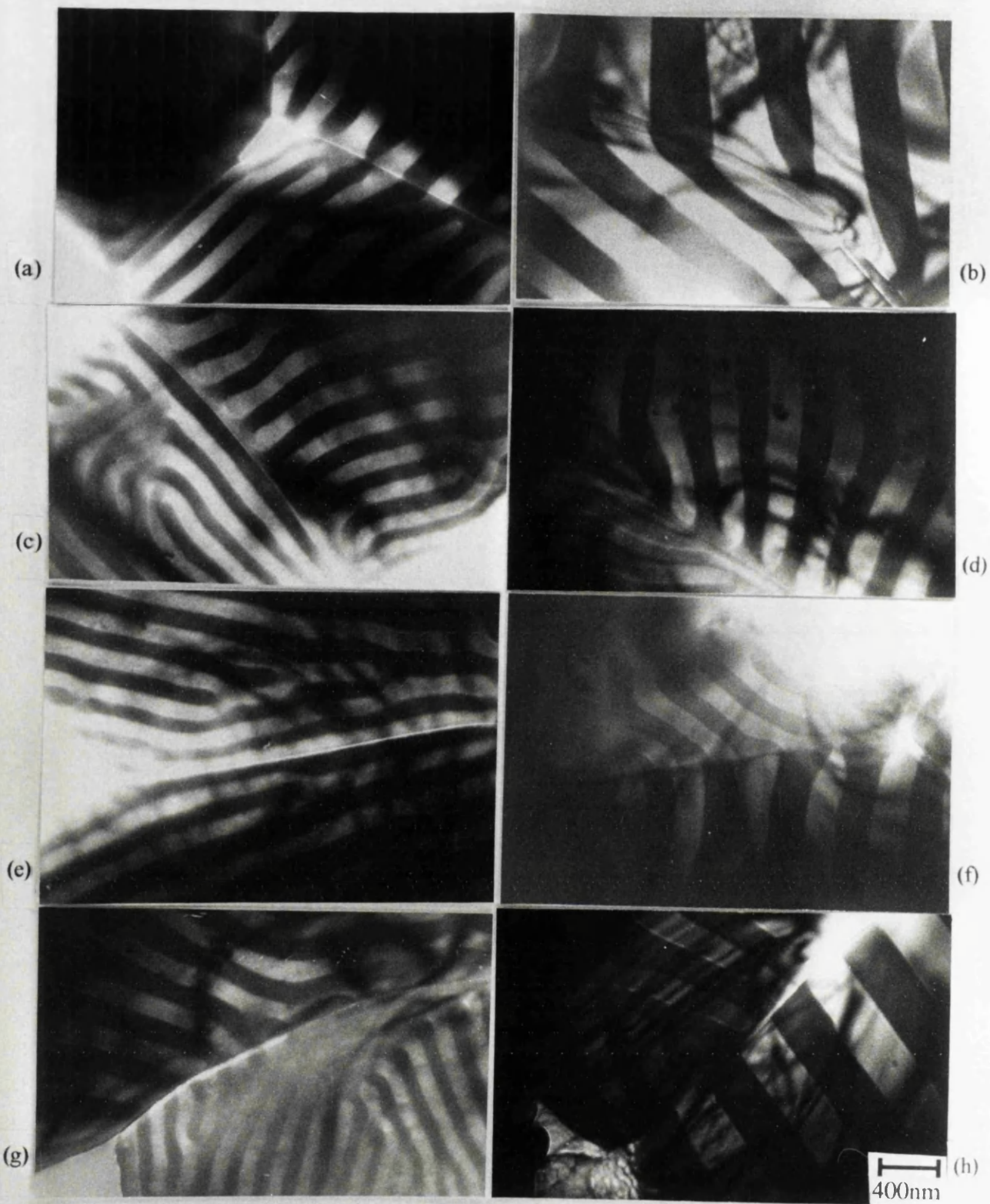

Figure 4.14: *Micrographs of domain wall behaviour at grain boundaries*

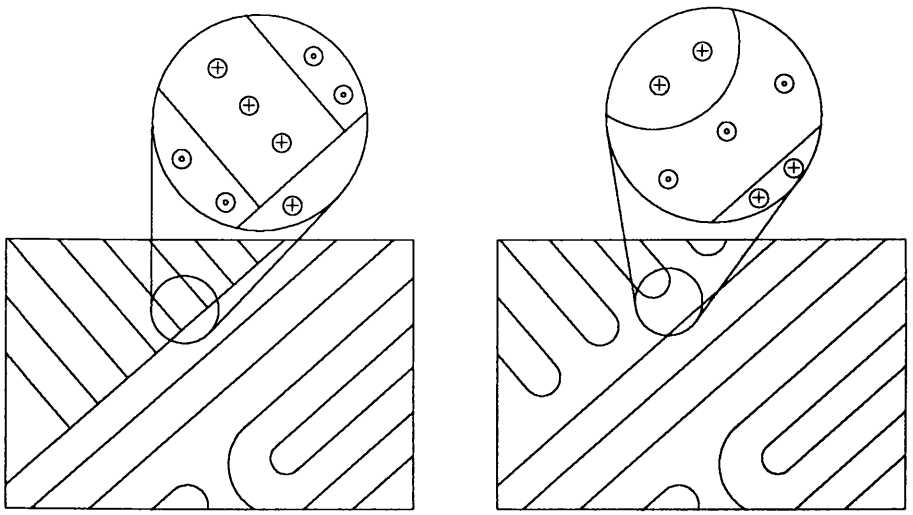

Figure 4.15: *Schematic of domain behaviour at grain boundary*

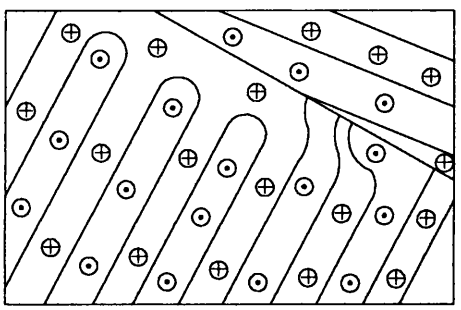

Figure 4.16: *Schematic of domain behaviour at grain boundary*

since one set of domains meets the boundary at such a shallow angle, the free poles at the boundary will alternate in polarity, see figure 4.16. As a result, some of the domains orthogonal to the boundary terminate to minimise the magnetostatic energy but at other regions on the boundary, it is domains of opposite polarity that attempt to terminate although as the schematic shows, this has not completely succeeded.

4.14(e): θ_1 and θ_2 small, $\mid \phi_1 - \phi_2 \mid \approx 0°$. The boundary is parallel to both sets of domains. The domains on either side of the boundary are oppositely magnetised.

4.14(f), (g): θ_1 and θ_2, $\mid \phi_1 - \phi_2 \mid$ small. There is clearly no continuity of domain walls across the boundary with domain walls on one side reaching the boundary in the centre

of a domain on the other. In some areas of the boundary, the domains appear distorted suggesting that the grains are not completely independent.

4.14(h): The last case has $\theta_1 \gg \theta_2$, $\mid \phi_1 - \phi_2 \mid \approx 0°$. One of the domains in the upper grain has terminated in a similar way to case (b) but in the lower grain, the large anisotropy means that the walls continue right to the edge of the grain.

It is tempting to think that in cases (a) and (b), the domain walls are exchange coupled across the grain boundary but there is not enough evidence to support this. An attempt by the two grains simply to minimise the magnetostatic energy at the boundary would result in the same structure. Detection of the presence or otherwise of a Nd rich phase between the boundaries (e.g. by x-ray analysis) would allow us to deduce which of the situations was more likely but this is not possible on the 2000-FX i.e. if the Nd rich phase were present, it is probable that the coupling would only be magnetostatic although if it were not present, this may not guarantee that the walls are exchange coupled. In examples (f) and (g), it is highly likely that the grain boundary phase is present since there is a total absence of wall continuity.

Many more micrographs than those shown were taken and these were studied in order to determine if any material exhibited a preference for one sort of behaviour over another but no differences were found. This may simply be a result of a relatively small data set (A total of $\approx$40 in all) but could also suggest that the magnetic behaviour at a grain boundary is determined by the processing method alone. Lastly, it is important to note that all types of behaviour were observed in all materials.

4.7 Conclusions

Thinned sections of NdFeB have been studied using bright field imaging and the Foucault mode of Lorentz microscopy. As expected from the large uniaxial anisotropy of the material, stripe domain patterns have been observed. These have a periodicity and directionality which is related to the inclination of the c-axis of a grain with respect to the grain normal. The dependence of P on θ has been investigated for each of the three materials and P has been found to increase with θ. In addition, for a given value of θ, materials B and C have a consistently higher value of P. The behaviour of domain

walls has also been studied. Various types of behaviour have been observed and these have been explained in terms of the misorientation between two grains. The magnetic structure alone does not allow us to deduce if the Nd-rich grain boundary phase is present although in certain situations, we may be justified in assuming that it is.

4.8 References

D.Givord, H.S.Li and J.M.Moreau, *Solid State Comms*, **50**, 6, pp497–499, (1984).

J.F.Herbst, J.J.Croat, F.E.Pinkerton and W.B.Yelon, *Phys.Rev.B*, **29**, 7, pp4176–4178, (1984).

L.Jahn, S.Hirosawa, V.Christoph and K.Elk, *Jpn.J.Appl.Phys*, **30**, pp489–492, (1991).

H.Miyajima, T.Yamamoto and Y.Otani, *J.Mag.Mag.Mat.*, **104–107**, pp1117–1118, (1992).

S.F.H.Parker, R.J.Pollard, D.G.Lord and P.J.Grundy, *IEEE Trans.Mag*, **MAG-23**, p2103, (1987A).

Chapter 5

Calculation of specific domain wall energy

Understanding the behaviour and properties of domain walls is vital for a better understanding of coercivity mechanisms. There are two parameters which characterise a domain wall i.e. its energy and its width. this chapter will deal with the domain wall energy.

The domain wall energy (see chapter 1) is usually expressed in terms of a specific energy (σ_w) which is the energy per unit area of the wall. The general expression for σ_w for a one dimensional wall is given by

$$\sigma_w = 2\sqrt{\mathrm{A}} \int_{-\pi/2}^{\pi/2} \sqrt{\mathrm{g}(\theta)} d\theta \tag{5.1}$$

where $\mathrm{g}(\theta)$ is the anisotropy energy. In a simple system an expression can be determined for σ_w by integrating the anisotropy and exchange energies across the width of the domain wall to give

$$\sigma_w = 4\sqrt{\mathrm{AK}} \tag{5.2}$$

In a more complex system it is unlikely that the integral could be evaluated algebraically and numerical integration would be required.

5.1 Kooy and Enz model

This model (Kooy and Enz, 1960) was originally devised to describe Barium Ferrite layers with a low coercivity and perpendicular anisotropy. It assumes the material has the following properties

1. Uniaxial anisotropy perpendicular to the layer.
2. Uniform thickness and infinite lateral dimensions.
3. No closure domains.
4. The domain structure consists of 180°domain walls.

We may apply this model to thinned sections of NdFeB if:

- The value of M in the model is replaced by $M\cos\theta$ where θ is the angle between the c-axis of the material and the section normal.
- The domain period is sufficiently small with respect to the grain size and therefore we can assume that the domain structure is unaffected by the finite extent of the grain. In the samples studied here, the grain size is 5–10μm while the domain widths are a few 100nm.
- We assume that the large anisotropy of the material inhibits the formation of closure domains but any deviation of the moments from the easy axis at the surface - the μ^* effect (Chikazumi, 1967) - can be accounted for.

$$\mu^* = 1 + \frac{\mu_0 M_s^2}{2K_1} \tag{5.3}$$

The values here are $\mu_0 M_s^2 = 1.43\times10^6 \mathrm{Jm}^{-3}$ and $2K_1 = 8.6\times10^6 \mathrm{Jm}^{-3}$ giving a value for $\mu^* = 1.2$.

The Kooy and Enz model is an energy minimisation model which consists of three terms i.e. the domain wall energy E_w, the energy due to an external field E_H and the demagnetising energy of the domain configuration E_d. These terms, per unit area of the material, are given by the following expressions:

$$E_w = \frac{2\sigma_w d}{P} \tag{5.4}$$

$$E_H = -\mu_0 M H d \tag{5.5}$$

$$E_d = \frac{1}{2}\mu_0 M^2 d + \frac{4\mu_0 M_s^2 P}{\pi^2(1+\sqrt{\mu^*})}\sum_{n=1}^{\infty}\frac{1}{n^3}\sin^2\left(\frac{n\pi}{2}\left(1+\frac{M}{M_s}\right)\right)\left(1-e^{-2n\pi\alpha}\right) \tag{5.6}$$

where P is the domain period, σ_w is the specific domain wall energy, d is the grain thickness and M is the magnetisation. α is defined to be

$$\alpha = \frac{d\sqrt{\mu^*}}{P} \tag{5.7}$$

The equilibrium domain period and magnetisation can be calculated by minimising the total energy with respect to the relevant parameters;

$$\frac{H}{M_s} = \frac{M}{M_s} + \frac{2}{\pi^2(1+\sqrt{\mu^*})}\frac{P}{d}\sum_{n=1}^{\infty}\frac{1}{n^2}\sin\left(n\pi\left(1+\frac{M}{M_s}\right)\right)(1-e^{-2\pi n\alpha}) \tag{5.8}$$

$$\begin{aligned}\frac{\sigma_w}{\frac{1}{2}\mu_0 M_s^2} &= \frac{4}{\pi^3(1+\sqrt{\mu^*})}\frac{P^2}{d}\sum_{n=1}^{\infty}\frac{1}{n^3}\sin^2\left[\frac{n\pi}{2}\left(1+\frac{M}{M_s}\right)\right] \\ &\cdot \left[1-\left(1+\frac{4\pi n\alpha\sqrt{\mu^*}}{1+\sqrt{\mu^*}}\right)e^{-2\pi n\alpha}\right]\end{aligned} \tag{5.9}$$

It would be expected from the large anisotropy of $Nd_2Fe_{14}B$ that the μ^* effect would be negligible and calculations showed that setting μ^*=1 made no difference to the final result. For M=0 and μ^*=1 and introducing the cosθ term previously discussed, the equation simplifies to

$$\frac{\sigma_w}{\frac{1}{2}\mu_0 M_s^2} = \frac{4\cos^2\theta}{\pi^3}\frac{P^2}{d}\sum_{n=1}^{\infty}\frac{1}{n^3}\sin^2\left[\frac{n\pi}{2}\right]\left[1-(1+2\pi n\alpha)e^{-2\pi n\alpha}\right] \tag{5.10}$$

The left hand side of this equation is the ratio of the domain wall energy to the maximum magnetostatic energy density and for simplicity is referred to as τ (Draaisma and de Jonge, 1987). This quantity has units of metres and is referred to as a characteristic length.

A 'C' programme was written using Borland C to evaluate this equation on a PC for the experimental values of P and θ. It was calculated for n between 1 and 50 since examination of the equation shows that the maximum value of the term being summed is proportional to an expression of the form $2\pi n\alpha e^{-2\pi n\alpha}/n^3$ which quickly becomes insignificant. The only unknown in the above equation is d. It must lie between certain limits i.e. the sample

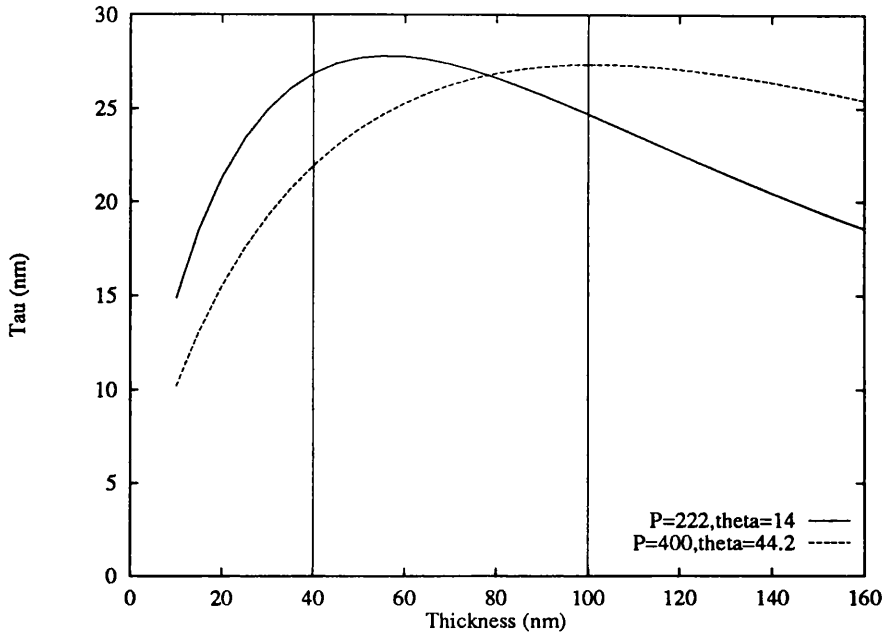

Figure 5.1: *Theoretical dependence of d vs τ*

200keV electrons. The equation was used to establish the theoretical dependence of τ on d. Two experimental points were chosen with small and large values of θ and the value of τ was calculated for d=10 to 160nm. This variation is shown in fig 5.1 for (P,θ)=(222nm,14°) & (400nm,44.2°) and it can be seen that τ varies by ±11% of the mean value for larger θ and only ±6% for smaller θ over the range 40<d<100nm.

5.2 Thickness Measurements

An estimate of the thickness for representative areas was obtained using Parallel Electron Energy Loss Spectroscopy (PEELS). This procedure involves measuring the areas under the zero loss peak, I_o and the entire spectrum, I_t (Egerton, 1986). The thickness can then be calculated as a multiple of the total inelastic mean free path length, L;

$$t = L \ln(I_t/I_o) \tag{5.11}$$

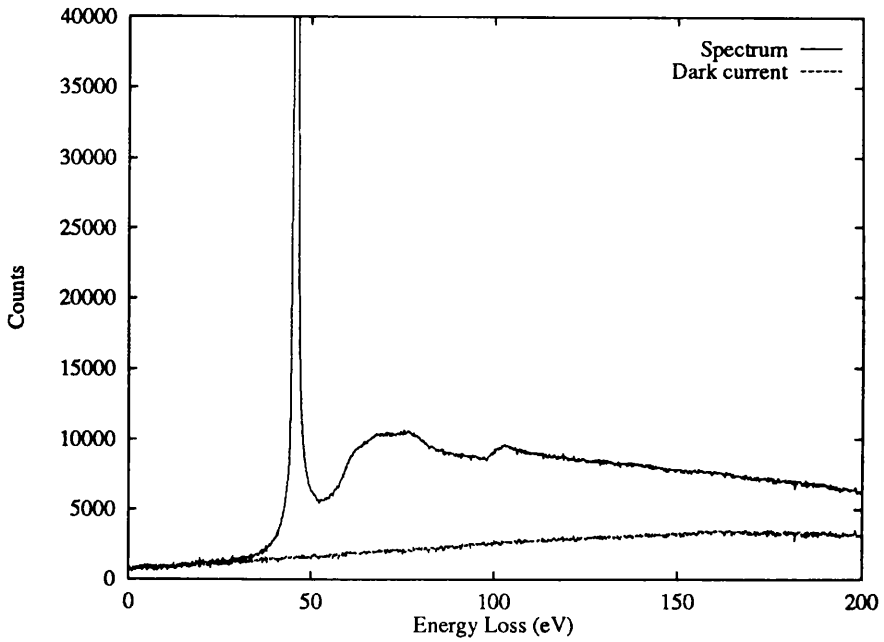

Figure 5.2: *PEELS spectrum from grain and 'dark current' spectrum*

A formula to calculate L in nm to an accuracy of ±20% has been determined empirically (Egerton, 1989);

$$L = \frac{0.106T}{E_m \ln(2\beta E_o/E_m)} \tag{5.12}$$

where E_o is the incident electron energy in eV, T is the relativistically corrected electron energy also in eV, β is the collection semi-angle. E_m=7.6$Z^{0.36}$ where Z is the mean atomic number. In this case, Z_{mean}=30.25, E_o=100keV and $\beta \approx$ 12.5mrad. This gives a value for L of 99nm.

The procedure involves obtaining a PEELS spectrum from a grain and then blanking the beam and obtaining a 'dark current' spectrum in the diode detector array. The 'dark current' arises from thermal electrons and other sources. Figure 5.2 shows a typical PEELS spectrum from an individual grain and the signal from the diode array with no beam present. Before any analysis can be done, the background must be subtracted, the resulting spectrum is shown in figure 5.3. In order for the thickness to be measured, the computer used for data acquisition models both the zero loss peak and the remainder of the spectrum minus the zero loss peak. both these are also shown in figure 5.3. A number

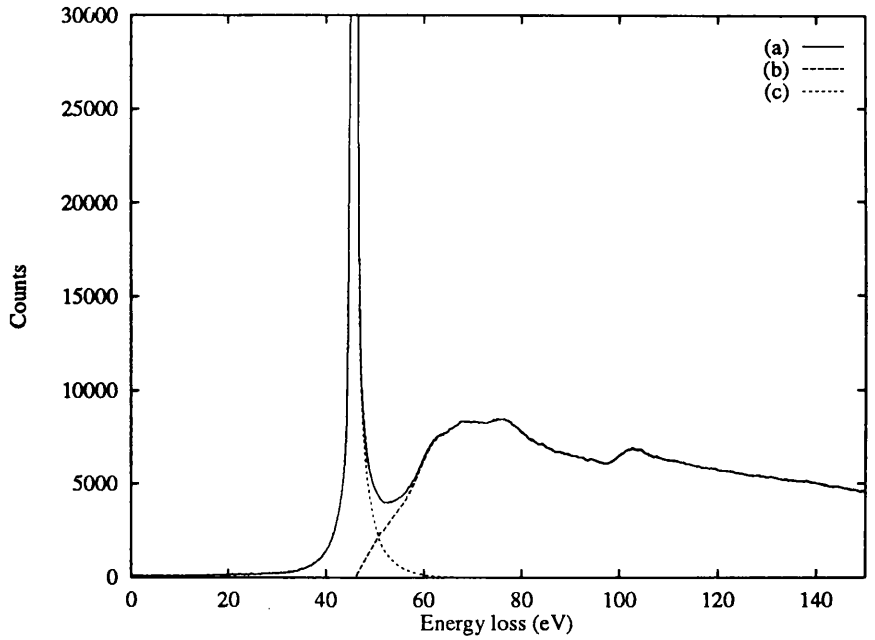

Figure 5.3: *PEELS spectrum after background has been subtracted (a) and computer calculated profiles of zero loss peak (c) and remainder of spectrum (b)*

of spectra were acquired from thin regions at the edge of grains and from thicker regions towards the centre of grains. This method produced thickness values as low as 8nm at the edge of a grain but more typically, 30–40nm. Towards the centre of grains the thickness was in the range 120–170nm. These grains were felt to be thicker than those typically investigated and the presence of the carbon edge in the spectra, due to contamination, would make the grains seem slightly thicker than they are. Consequently, a mean value for d of 80nm was assumed throughout the calculations.

τ was calculated for each (P.θ) and was graphed against θ (see figure 5.4). It is clear that for alloy A, the value of τ is constant over a wide range of θ; this suggests that the value is characteristic of the material rather than of a thinned section. The two marked points on the graph clearly do not fall within the limits of experimental error. The micrographs corresponding to these points show no obvious difference between these domain structures and others observed. Figures 5.5 and 5.6 show plots of τ vs θ for materials B and C. It is clear that for both these materials, τ is consistently higher. The

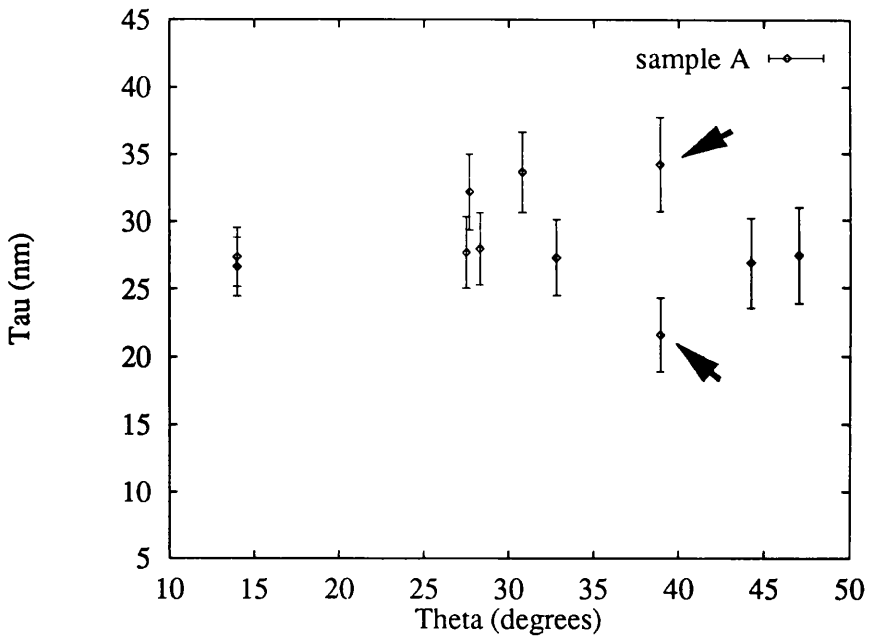

Figure 5.4: *Graph of τ vs θ for sample A*

other major difference is that τ does not remain constant, but tends to decrease slowly with increasing θ. It has been mentioned earlier that the model is only applicable when the domain period remains unaffected by the finite extent of the grain but no evidence of any peculiarities in the domain structures were clear from the micrographs. In the original paper by Kooy and Enz (1960), they observed the variation of domain period with field in Ba ferrite samples and observed that although the domain period increased, implying a reduction in the number of domains, this was not as a result of domain wall annihilation but as a result of unfavourably oriented domains reducing their length. This is clearly only possible when the easy axis is nearly parallel to the applied field i.e. small θ since domains with much larger values of θ will only be able to change their width. Further experimental calculations to investigate the variation of total energy with domain period (see figure 5.7) showed that the energy minimum for a particular (P,θ) if P is allowed to vary from P-50nm to P+50nm becomes progressively more shallow at higher values of θ. This suggests that at larger θ, the grains studied have a greater chance of settling into a non-equilibrium state.

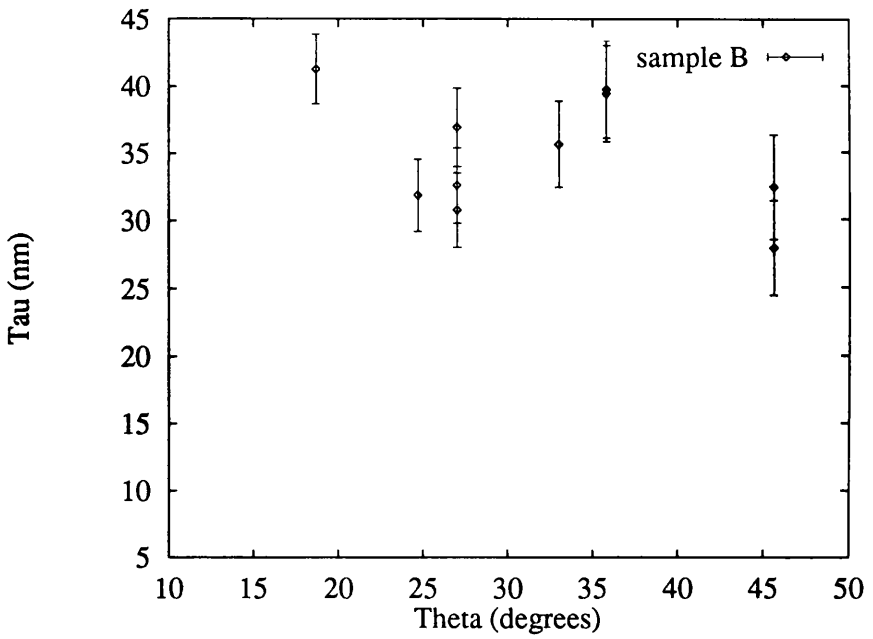

Figure 5.5: *Graph of τ vs θ for sample B*

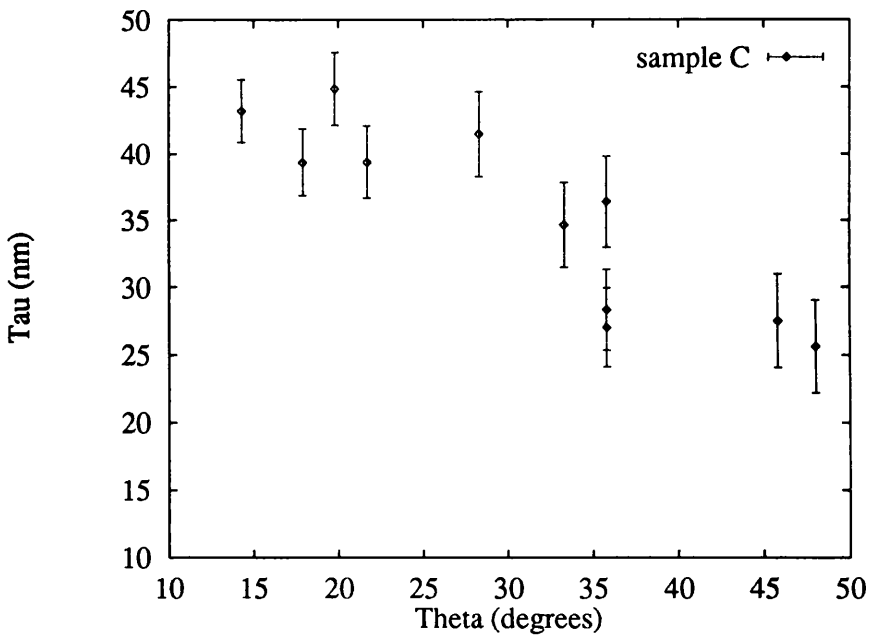

Figure 5.6: *Graph of τ vs θ for sample C*

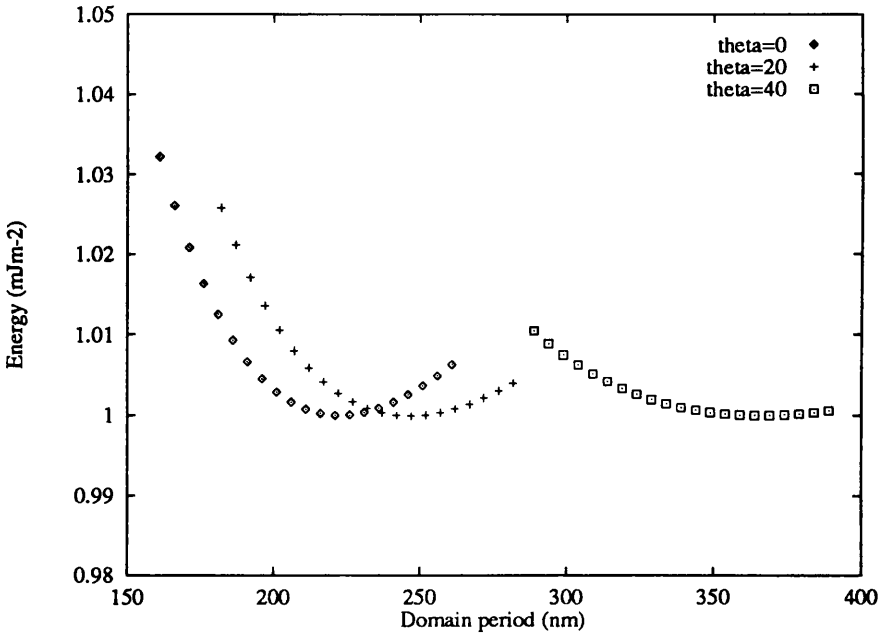

Figure 5.7: *Variation of total energy with domain period. All values plotted relative to the appropiate energy minimum*

	τ (nm)	σ_w (mJm^{-2})	M_s(T)
Sample A	28.4±1.0	20.3±0.8	1.34
Sample B	34.2±1.4	18.4±0.6	1.16
Sample C	36.6±2.4	19.6±2.6	1.16

Table 5.1: *Values of τ, σ_w and M_s for each of the samples*

	σ_w(mJm^{-2})	Method	Reference
1	24	Grain thickness	Pastuchenkov et al, 1991
2	25	Grain thickness	Szymczak et al, 1987
3	22	Grain thickness	Mishra, 1987
4	38	Wall thickness	Bras et al, 1988
5	17	Wall thickness	Mishra and Lee, 1986

Table 5.2: *Values of σ_w obtained by other researchers*

Table 5.1 shows the values of τ and σ_w for each of the samples. The values of τ given are simply the averages. This is certainly justified for sample A and to a lesser extent for sample B; the decrease of τ with θ in sample C is much more marked and so this will produce a less accurate result. σ_w was calculated using the values of M_s which were measured with a VSM at Sheffield University in fields up to 5T. Table 5.2 shows values obtained by other researchers and the methods used to obtain them. The values of σ_w show good order of magnitude agreement with these. The first three values were obtained using models (Hubert, 1967; Szymczak, 1973) which relate the domain width to the sample thickness in grains where the easy axis is perpendicular to the plane of the grain. The remaining two were deduced from electron microscopy studies which allowed the domain wall width to be estimated. This second method is quite inaccurate as is evidenced by the difference in the two results quoted; results from the first method show better consistency. It is also worth noting that for $Nd_2Fe_{14}B$, A=7.7×10^{-10}Jm^{-1} and K_1=4.3×10^{6}Jm^{-3} which, from equation 5.2. gives a theoretical value for σ_w of 23.0mJm^{-2} which again shows good general agreement with the experimental values, given that the assumptions implicit in this approach may not hold for $Nd_2Fe_{14}B$.

The results for B and C seem suprising at first since these, Dy containing, samples have a slightly lower but essentially similar value for σ_w. It is known that $Dy_2Fe_{14}B$ has a much greater anisotropy field than $Nd_2Fe_{14}B$ (see chapter 2) the values being 15.0T and 6.7T respectively (Hirosawa et al. 1986) and it would be expected that an alloy with a composition of the form $Nd_{2-x}Dy_xFe_{14}B$, where in this case x=0.39, would have

a larger anisotropy than the basic alloy. Such an increase would result in an increase of the domain wall energy but this does not seem to be the case. The explantion for this lies in the strength of the coupling between the Fe and the RE atoms. It is known that the coupling between Dy and Fe is a factor of two smaller than that between Nd and Fe (Herbst, 1991) and so it appears that the increase in K is more than offset by the decrease in A. This is confirmed by various researchers (Givord et al, 1988A; Yamada et al, 1988) including Yong et al (1989) who have calculated the RE-Fe exchange fields to be 626T and 320T for Nd-Fe and Dy-Fe repectively. Although clearly an approximation, if we assume that there a linear change in the anisotropy field and the exchange field with x and further assuming that these quantities are proportional to K and A respectively then for x=0.39 there is only a slight increase in σ_w of about 7% which tends to support the experimental evidence i.e. little change in σ_w.

This has further consequences; the domain wall width, δ_w, is given by the expression $\sqrt{A/K}$ (Chikazumi, 1967) and therefore there will be a decrease in δ_w for material B. Continuing the assumptions previously stated, this would lead to a value of δ_w for material B which is 86% of the value for material A. Theoretical modelling of the type undertaken by Kronmuller et al (1988) and Givord et al (1988B, 1988C) relates the coercivity to the domain wall width. In the paper by Givord et al (1988B), the coercivity of an individual grain is inversely related to the activation volume and the saturation magnetisation. The activation volume is the region in which initial magnetisation reversal occurs and is proportional to the cube of the domain wall width. This fact and the reduction in M_s gives a coercivity of twice that of sample A. Whilst not explaining the fourfold increase in coercivity observed in the bulk material, this must certainly contribute.

5.3 Testing the validity of the model

A major assumption of the model is that the domain structures observed are equilibrium structures i.e although they are at some energy minimum, it may only be a local minimum and application and removal of a field may result in some lower energy state.

Some magnetising experiments were undertaken in order to determine if the domain walls behave as the model predicts. No field can be applied to a sample using the Lorentz

lens of the 2000-FX and a magnetising rod designed at Glasgow for the study of low coercivity films is only able to supply a maximum field of 150Oe which is not sufficient for these materials.

5.3.1 JEOL 1200-EX

The bulk coercivity of these materials is such that when imaged using a standard immersion objective lens, the domains can still be observed in Fresnel mode. A Fresnel image of alloy A obtained under standard imaging conditions is shown in figure 5.8. As expected favourably oriented domains are wider than those whose orientation is opposite to the vertically applied field. The objective strength was increased and then decreased to a value where a Fresnel image could be obtained. A second image showing the sample after it had been exposed to the maximum field ($\sim$0.8T) is also shown in figure 5.8. Modifications of the domain structure have taken place and bubble domains of differing sizes can be seen but overall it has returned to a very similar state. A major disadvantage of this method is that while the sample can be subjected to different fields, the domains can only be observed at one field value.

5.3.2 Philips CM-20

The domain structure under different but constant applied fields can be observed using the Lorentz lens of the CM-20 in conjunction with the standard objective lens. With only the Lorentz lens switched on, a Fresnel image of a grain was obtained. The standard objective was then switched on. A series of images were taken under increasing objective field strengths being careful at each stage to keep some reference feature in the image in order to allow magnifications to be determined so that domain widths could subsequently be measured. This was neccesary since the objective field affects the imaging conditions which leads to a change in the magnification and a rotation of the image. This meant that eventually, the image became too large for the reference points to be on the micrograph and the magnification due to the intermediate lenses had to be reduced. The objective field also affects the quality of the image and so the defocus had to be adjusted during the experiment to improve the visibility of the domain walls. This was done for materials

Figure 5.8: *Photos before and after sample has been exposed to max objective field of the JEOL 1200-EX*

A and B. The microscope does not directly provide the objective field strengths but the excitation is indicated by a number between 0 and 100000 where the maximum field strength is equivalent to 100000. It is these numbers that were noted during the experiment and it is assumed that there is a linear relationship allowing intermediate field values to be calculated from the maximum field of 1.3T. Although it proved impossible to image the walls at the maximum field strength, the sample was still subjected to this field to determine what effect it would have.

5.3.3 Results

Figure 5.9 shows some examples of the domain structures in material B at various objective field strengths. As would be expected, some of the domains, which are more favourably oriented, increase in width at the expense of the less favourably oriented ones. There is evidence of domain wall pinning in image (c) from the severe kink in the wall however this pinning disappears above 0.6T. At low fields, the domain walls at the edge move out of the field of view, allowing the overall domain period to increase. It is not possible to say what happens to these walls. At higher fields, some of the domains appear to be pinned at the edge of the grain while others, rather than narrow any further, are becoming shorter as observed by Kooy and Enz. At 0.9T, the walls are no longer pinned at the edge and they recede into the bulk of the grain. The domain period was measured directly from the micrographs taking into account the variation in magnification by scaling each apparent domain period by the calibration distance.

The predicted theoretical variation of the domain period with increasing field strength was calculated using equation 5.8. The experimental value of τ previously calculated for the material (see table 5.1) and the measured value of the saturation magnetisation were used. The value of θ was calculated from a diffraction pattern (see chapter 4) and M was allowed to vary from 0 to M_s and the RHS of the equation was calculated using increasing values of P until the difference between the computed value and the experimental value was less than 1% of P. This value of P was substituted in equation 5.8 to calculate the corresponding field value for the assumed M.

Figures 5.10 and 5.11 show the experimental (points) and theoretical (lines) variations of P with the objective field strength. The graphs illustrate that at low objective field

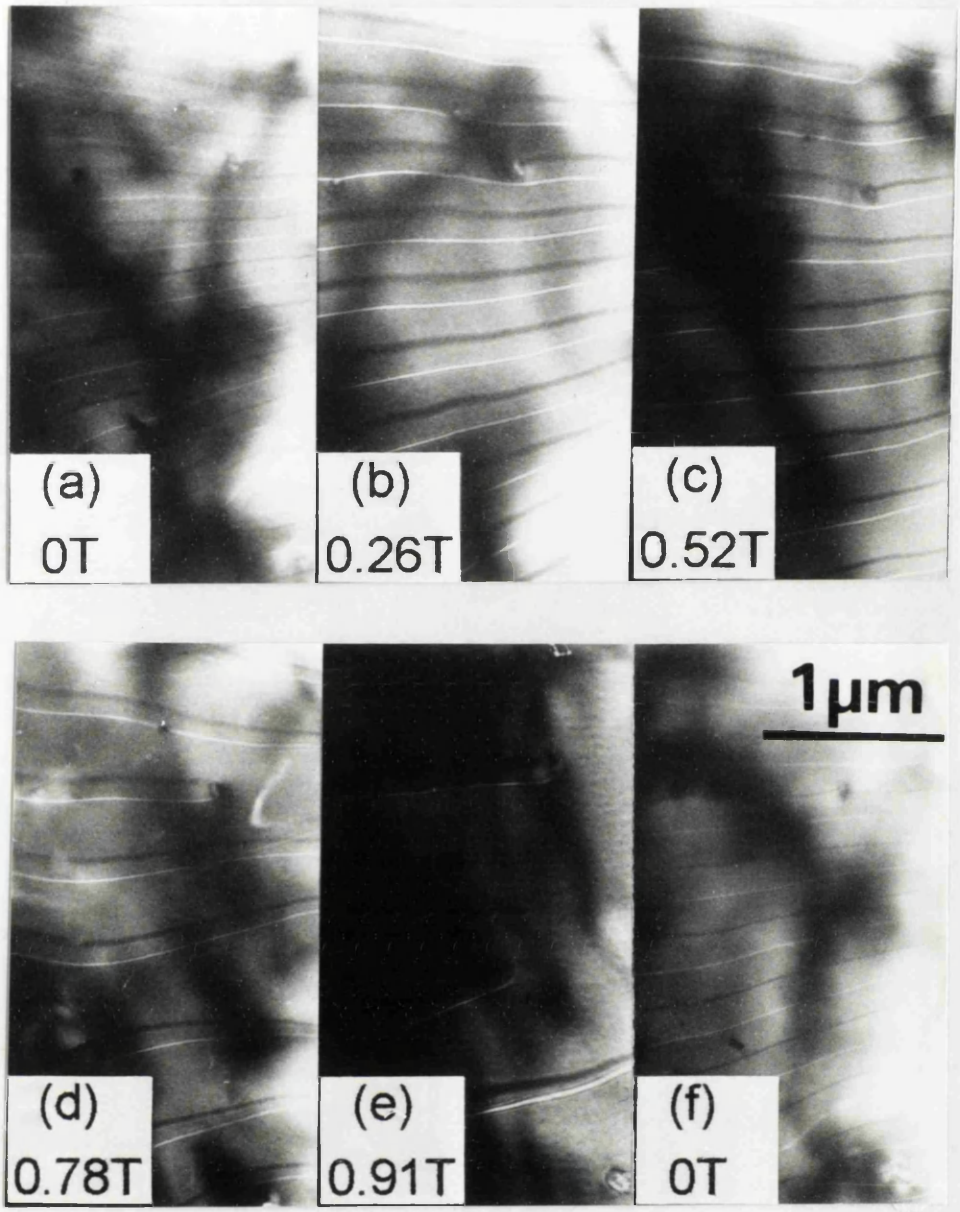

Figure 5.9: *Domain structures in an applied field*

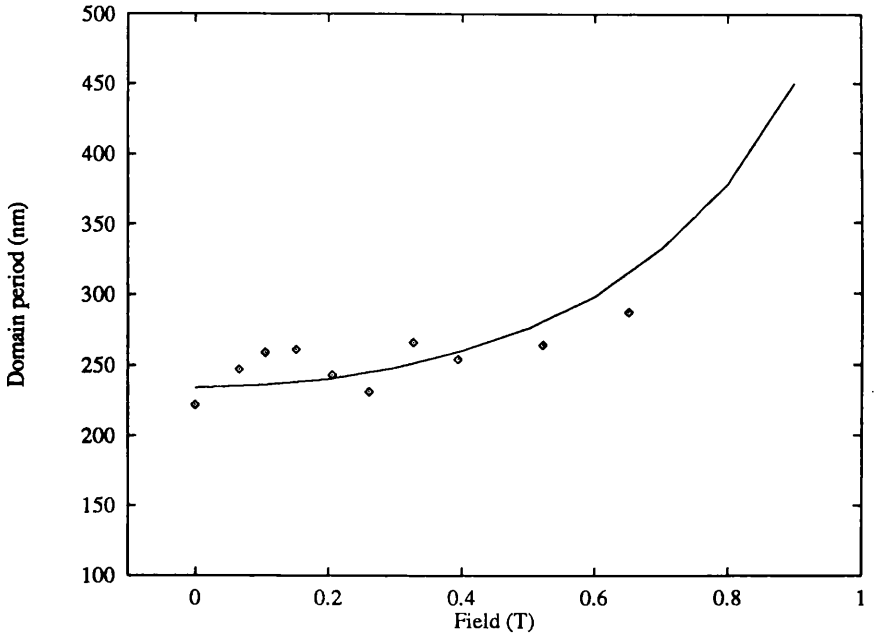

Figure 5.10: *Variation of P with objective field strength for material A*

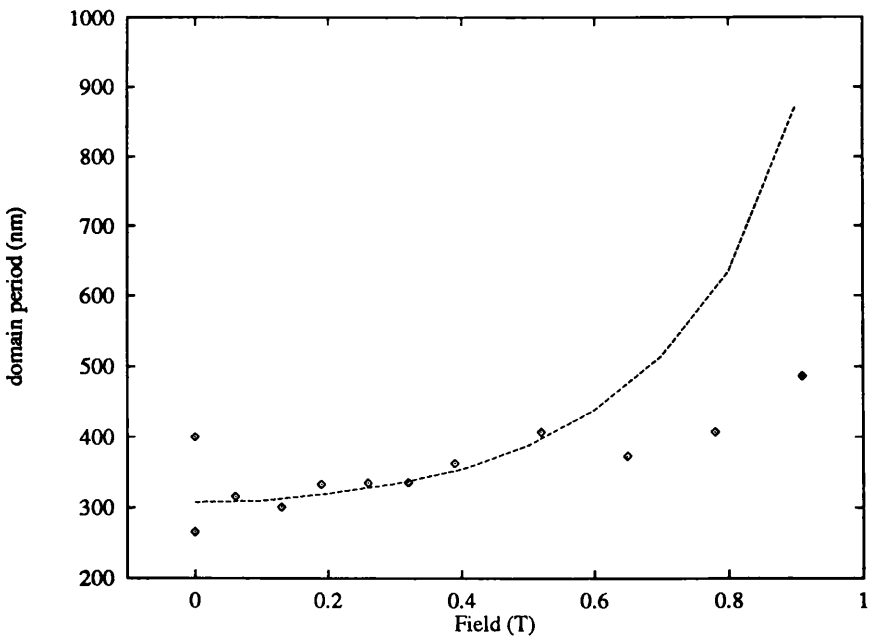

Figure 5.11: *Variation of P with objective field strength for material B*

values, there is good agreement between the model and the experimental results but at higher values, the experimental results fall well short of the predicted values. One definite contributor to this will be the demagnetising field; although the model calculates the demagnetising field, this is for an infinite plate and account must be taken of the finite extent of the sample e.g. Kooy and Enz (1960) set the demagnetising factor, N, to be 0.95 and accounted for this by reducing all the experimental field values by 5%. This would bring the theory and the experiment closer. In addition, the model relies on the field being applied along the easy axis which was not the case here and so actual fields applied along this direction will be smaller than the graph scale suggests.

If the domain periods before and after the sample has been subject to the maximum field are compared it can be seen that it has increased by 134nm or over 50% of the original value. This clearly indicates that there are fewer walls than before suggesting that some have either been annihilated or swept out of the grain.

5.4 Conclusions

The Kooy and Enz model has been used to calculate specific domain wall energies for each of the materials and values of σ_A=20.3mJm^{-2}, σ_B=18.4mJm^{-2}, σ_C=19.6mJm^{-2} have been obtained. This has shown that the addition of Dy does not have a significant effect on σ_w. This is explained by noting that although anisotropy field of $Dy_2Fe_{14}B$ is twice that of $Nd_2Fe_{14}B$, the exchange field is halved. These differences in the exchange and anisotropy constants further suggest that the domain walls in the Dy containing materials are significantly narrower which, theoretical models suggest, may contribute to the increased coercivity. On the rough assumption that the increase in anistropy field and the decrease in exchange coulping are linearly proportional to the Dy content, an increase in the coercivity by a factor of two has been accounted for. The results of the application of a magnetic field to the specimens suggest that, despite their high bulk coercivity, the domain walls within a grain behave as predicted by the Kooy and Enz model under small applied fields. At higher fields, the experimental values are lower than those predicted but the finite extent of the plate and the application of the field along an axis other than the easy axis will contribute substantially to this.

5.5 References

J.Bras, J.Degauque and M.Fagot, *Solid State Comms.*, **68**, pp117–122, (1988).

S.Chikazumi, Physics of Magnetism, Pub. John Wiley and Sons, p216, (1964).

H.J.G.Draaisma and J.M. de Jonge, *J.Appl.Phys.*, **62**, pp3318–3322, (1987).

R.F.Egerton, *Ultramicroscopy*, **28**, pp215–225. (1989).

R.F.Egerton, Electron Energy Loss Spectroscopy in the Electron Microscope, Plenum Press, (1986).

D.Givord, H.S.Li, J.M.Cadogan, J.M.D.Coey, J.P.Gavigan, O.Yamada, D.Givord, P.Tenaud and T.Viadieu, *J.Mag.Mag.Mat.*, **72**, pp247–252, (1988B).

D.Givord, P.Tenaud and T.Viadieu, *IEEE Trans.Mag.*, **24**, pp1921–1923, (1988C).

J.F.Herbst *Rev. Mod. Phys.*, **63**, pp819–899. (1991).

S.Hirosawa, Y.Matsuura, H.Yamamoto, S.Fujimura, M.Sagawa and H.Yamauchi, ***J.Appl.Phys.***, **59**, pp873–879, (1986).

A.Hubert, *Phys.Stat.Sol.*, **A43**, p571, (1967).

C.Kooy and U.Enz *Philips.Res.Rep.*, **15**, p7, (1960).

H.Kronmuller, K.D.Durst and M.Sagawa, *J.Mag.Mag.Mat.*, **74**, pp291–302, (1988).

H.Maruyama, M.Sagawa and S.Hirosawa, *J.Appl.Phys.*, **63**, pp3713–3715, (1988).

R.K.Mishra, *J.Appl.Phys*, **62**, pp967–969. (1987).

R.K.Mishra and R.W.Lee, *Appl.Phys.Lett.*, **48**, pp733–735, (1986).

J.Pastuchenkov, A.Forkl and K.Kronmuller, *J.Mag.Mag.Mat.*, **101**, p363, (1991).

R.Szymczak, *Acta.Phys.Pol A*, **43**, p669, (1973).

R.Szymczak, D.Givord and H.S.Li, *Acta.Phys.Pol A*, **72**, pp113–115, (1987).

M.Yamada, H.Kato, H.Yamamoto and Y.Nakagawa, *Phys.Rev.B*, **38**, pp621–633, (1988).

Z.Yong, Z.Tiesong, J.Hanmin, Y.Fuming, X.Jinqiang, L.Xinwen, Z.Ruwen and F.R.de Boer, *IEEE Trans.Mag.*, **25**, pp3443–3445. (1989).

Chapter 6

X-rays–Production and Detection

An atom consists of a nucleus surrounded by up to six shells of electrons viz the K, L, M, N, O and P shells (Dyson, 1990; Titchmarsh, 1992). Each of these shells is split into various energy levels determined by the relevant quantum numbers (of interest here are the K, L_I-L_{III} and M_I-M_V shells). The energy levels of every element are unique and can be used to identify that element.

When a beam of high energy electrons is incident on a sample, an incident electron can lose energy during a collision with a bound electron in an atom of the sample and in the process eject a bound electron from the atom. This results in an ionised atom which has a short lifetime and quickly reverts to a lower energy configuration by the transition of a higher shell electron to this shell.

6.1 K-lines

If an electron is ejected from the K shell then (selection rules permitting) the resulting hole may be filled by an electron from a higher shell (Dyson, 1990) i.e. the L or M shell or in the heavier elements, the N shell (see figure 6.1). The energy released from this transition may be detected by emission of an Auger electron or by emission of a characteristic x-ray. Auger electrons are emitted when the energy release is sufficient to eject another electron from the atom; this will not be discussed further here. If the transition electron is from the L-shell then a Kα x-ray line is produced. This is the most intense peak since any electrons from the M-shell may simply fill the holes left by electrons which have de-excited from the

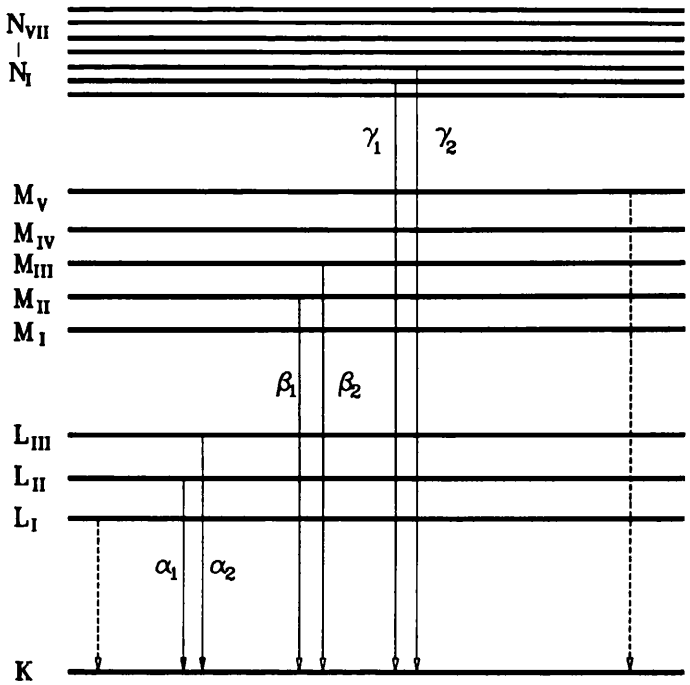

Figure 6.1: *Atomic energy levels showing allowed and forbidden transitions to the K shell*

L-shell. Any electrons which de-excite directly from the M to K shell contribute to the Kβ line which is higher in energy since the energy levels are further apart. Selection rules restrict the number of transitions allowed from each of the higher shells to the K-shell and the energy difference between these subshells is small when compared to the energy of the transition e.g. for Fe the splitting of the Kα line is 0.01keV. Consequently, although there are two transitions involved in each line, the energy resolution of the detector used in this work means that only a single Kα and Kβ peak are observed. The ionisation cross section for an atom is denoted σ_i and calculation of this quantity will be discussed later in the chapter. The proportion of electron transitions which result in x-ray emission (as opposed to Auger electron emission) is given by the fluorescence yield (ω_K). The product of these two quantities is the x-ray production cross section - σ_K. The other important parameter for K shell x-rays is the partition function, s, which is given by;

$$s = \frac{I_{\mathrm{K}\alpha}}{I_{\mathrm{K}\alpha} + I_{\mathrm{K}\beta}} \tag{6.1}$$

where $\mathrm{I}_{\mathrm{K}\alpha}$ and $\mathrm{I}_{\mathrm{K}\beta}$ denote the intensities of the Kα and Kβ lines. In the work presented

Although many of the quantities mentioned have been measured or calculated, their accuracy is less than that for similar quantities pertaining to the K-shells. This, combined with the increased uncertainty due to the increased number of quantities, means that these lines are only used when the K energy is too large to be conveniently detected e.g. in high Z elements. This is the case for Nd.

6.3 Bremsstrahlung radiation

In addition to the characteristic x-rays emitted, there are also the x-rays produced by any accelerating charged particle. This leads to a continuum which underlies all the x-ray peaks and has to be considered if quantitative results are to be obtained. The intensity of this radiation decreases sharply with increasing energy (see figure 6.2) and unlike characteristic x-rays it is anisotropic, being preferentially emitted in the forward direction (of the beam) (Nicholson, 1983). Various expressions have been proposed to model this background (e.g. Koch and Motz, 1959; Elwert, 1939) and considerable work has been done in the Glasgow group to test these experimentally. The most satisfactory model was found to be the modified Bethe-Heitler (MBH) formula with empirically determined parameters. (Chapman et al, 1983, 1984).

6.4 X-ray detection

Although characteristic x-ray radiation is emitted isotropically, practical considerations such as the confined space available within the microscope column and the difficulties involved in detecting large amounts of x-rays mean that only a very small fraction of the emitted x-rays are actually detected (the detector is $30mm^2$ at a distance of 20mm from the sample i.e. the detector subtends an angle of 0.1sr at the sample). The detector is positioned to reduce the detected Bremsstrahlung at an angle of 100° to the forward direction of the beam. The x-ray detector used at Glasgow is supplied by Link Analytical. It consists of a 3mm block of single crystal Si which has been drifted with Li in order to fill any traps in the crystal which could act as recombination sites for electron-hole pairs and reduce the efficiency of the detector. At the back of the detector there is a liquid nitrogen

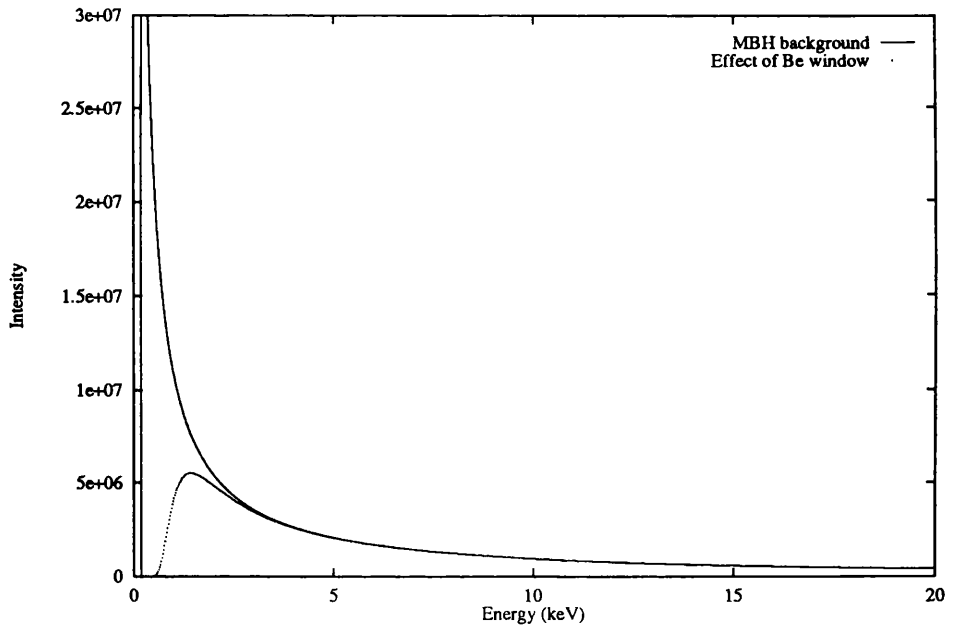

Figure 6.2: *Bremsstrahlung intensity vs energy*

(LN_2) cooled FET which amplifies any signal. There is an 8μm thick beryllium window in front of the Si which prevents both contamination and the build up of any moisture. The presence of this window leads to absorption of low energy x-rays which makes quantitative analysis of low energy peaks more difficult. The effect of this window on the background is shown by the dotted line in figure 6.2.

6.5 Acquisition hardware/software

The acquisition hardware used in this work was an eXL supplied by Link Analytical. This splits the incoming signal into 1024 energy bins, the size of these bins can be set to 10, 20, 40 or 80eV giving rise to a maximum detectable energy of 10.24, 20.48, 40.96, 81.92keV. Clearly the larger the energy range required, the lower the resolution. The work presented here was all done with the energy range set to 20.48keV. The software allows 'windows' to be painted onto a spectrum. This allows the user to define an energy region which covers the peak of interest and which can later be used to quantify the composition of the

sample.

6.6 Quantitative analysis

It is rarely sufficient to know only that an element is present in a sample, it is usual to want to know in what quantity in order that compositional variations may be determined.

6.6.1 Subtraction of background

Having acquired a spectrum, the first stage is to remove the background. As mentioned earlier this can be accurately modelled but for peaks whose centre energy is greater than ~4keV or where the peak to background ratio is very large this is unnecessary. A simpler way is to find the average counts on either side of the peak and assume the background decreases linearly. The background at the centre channel of the peak window can be found and the total background can be calculated by multiplying it by the width of the peak window. This is shown schematically in figure 6.3.

6.6.2 Composition

It is possible to obtain compositional information by studying the variation in the total peak counts between spectra but this has many problems.

1. The sample thickness must be known since a thicker sample will produce more x-rays irrespective of any change in the composition.

2. The beam current must be recorded for each spectrum since x-ray production is directly proportional to it.

3. Any beam current variation during the acquisition of a spectrum must be estimated in order to give an idea of the total charge incident during acquisition period.

All of these problems can be avoided by using the method of ratios.

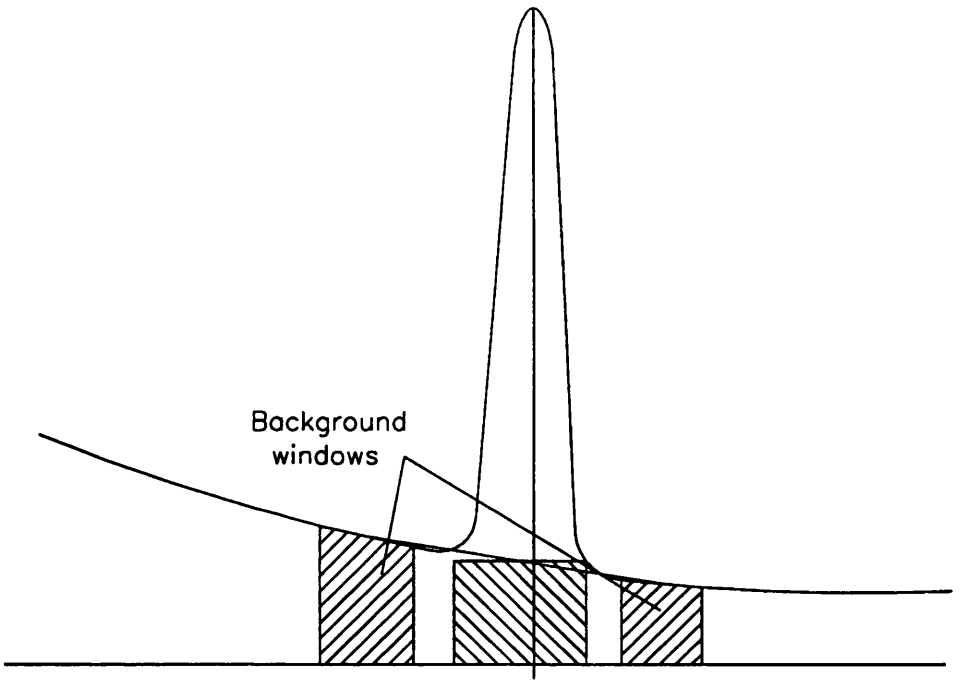

Figure 6.3: *Schematic of peak showing background windows*

6.7 k-factors and the method of ratios

In this method, the ratio of each element is calculated with respect to a chosen peak. Different elements have different x-ray production cross sections and the emitted x-rays are detected with different efficiencies. Consequently, the ratios of the peak counts of two different elements will not be identical to the ratio of the atomic concentrations. The correction factor is known as the k-factor and. for two elements A and B, is defined as follows (Cliff and Lorimer, 1975):

$$\frac{n_A}{n_B} = k_{AB}\frac{N_A}{N_B} \tag{6.6}$$

where $n_{A,B}$ are the atomic concentrations of elements A and B, and $N_{A,B}$ represent the total counts in the x-ray peaks of elements A and B. k_{AB} can be calculated from;

$$k_{AB} = \frac{\sigma_B \omega_B s_B \varepsilon_B}{\sigma_A \omega_A s_A \varepsilon_A} \tag{6.7}$$

	X-ray energy (keV)	ω_K	s	σ_K (barns)	$\sigma_L\omega_L$ (barns)	k_{XFe}
Fe K-lines	6.40,7.06	0.34	0.880	291.8	-	1
Nd L-lines	4.6-6.6	-	1	-	132.9	0.65
Nb K-lines	16.6,18.65	0.747	0.835	67.1	-	2.08

Table 6.1: *Relevant parameters of elements of interest*

Where $\varepsilon_{A,B}$ is the detector efficiency at the characteristic x-ray energy for each element; this is approximately 1 in the range 4–16keV. The theoretical values for σ_K may be calculated using various expressions as reviewed by Powell (1976) but the following expression proposed by Bethe (1930) was determined experimentally by Paterson et al (1988) to have a mean error of ~7%;

$$\sigma_K = \frac{132088}{T_0 I_K} b_K \ln\left(c_K \frac{T_0}{I_K}\right) \tag{6.8}$$

where σ_K is in barns I_K is the ionisation energy in keV of the element under study, T_0 is the accelerating voltage of the electron beam in kV and b_K and c_K are experimentally determined parameters (Paterson, 1988). A similar equation, allowing for the difference in electron occupancy between the K and L shells, may be applied to the L shells to determine σ_{LI-III} (Lorimer, 1983). Table 6.1 shows values of these theoretical parameters for the elements of interest as well as the energies of the characteristic x-ray lines.

6.7.1 Accuracy of Method

X-ray peaks have a Gaussian distribution and therefore, for a peak count of N, the standard deviation is $\sqrt{N}$ although if this peak is on a background then this has to be modified slightly as is described later. For experimental k-factors, the accuracy can be improved simply by measuring them many times. It is important to note that the k-factor for two elements is unique to each microscope/detector configuration. The accuracy of theoretical values varies depending on the atomic number. As stated earlier, the average error in σ_K is calculated using the Bethe expression 7% but the peak error can be as high as 20% (Paterson et al, 1988). The error in quantities such as ω_K is <3% for Z>30 (Krause, 1979). The values of parameters related to L-line emission are much less certain with the minimum error in ω_i being 3–5% for 70<Z<90. Outside these limits errors may be as

high as 30%. The Coster-Kronig yields are only accurate to within 5% at best but more generally 20% reaching to a maximum of 100% again depending on the atomic number (Krause, 1979).

6.8 Beam Broadening

Although the probe size is of the order of 1nm, electron scattering within the sample means that x-rays are produced from a larger area leading to a deterioration in the resolution. A useful estimate of the effects of beam broadening in a sample of thickness t can be deduced from the following equation which was proposed by Goldstein et al (1977);

$$b = 6.25 \times 10^5 (Z/E_0) t^{3/2} (\rho/A)^{1/2} \tag{6.9}$$

where b is the diameter in nm on the exit surface of a sample within which 90% of the electrons emerge. E_0 is the electron energy. A is the atomic weight, Z is the atomic number and ρ is the density in gcm^{-3}. There has been much Monte Carlo modelling of the above equation (Hren et al, 1979) done by calculating the paths of individual electrons through a thin film as they undergo elastic and inelastic scattering. These models agree to within 40% allowing a first order estimate to be made of the source size. For $Nd_2Fe_{14}B$ the average atomic number and weight are 30.25 and 67 respectively. Assuming 100keV electrons and t=80nm, b=1.4nm. A idea of the ultimate resolution can be obtained by summing b and the probe diameter, d$\simeq$1nm, in quadrature to give 1.7nm.

6.9 Data Analysis

The acquired spectra are usually given a rootname followed by a number to identify the spectrum. This greatly simplfies data transfer and analysis. While the spectra are still on the eXL, a windows file is created with windows which cover all the peaks of interest and also the background on either side. The spectra and the windows file are first transferred to a PC using a program supplied by Link which converts the spectra into MS-DOS format. A 'C' program called **WINDOSUM** (listed in appendix A) was written by myself which operates as follows; the user is prompted for the rootname of the series of spectra, the number of spectra, the windows filename and a suitable output filename. The program

then produces an output file containing the following information; the window labels, the width of each window in channels, the centre energy of the window and the total counts in each window for each spectrum. The format of this file is suitable for use in Quattro Pro, a spreadsheet program, thus greatly simplifying the data analysis. Once in the spreadsheet, the background counts were subtracted from the peaks and the ratios of total peak counts of each element to total Fe peak counts were found.

The analysis was carried out as follows, the atomic fraction, f_i, of each element is given by the following equation (McGibbon, 1989).

$$f_i = \frac{n_i}{\sum_j n_j} = \frac{N_i}{N_i + \sum^{j \neq i} k_{ij} N_j} \tag{6.10}$$

which gives for example;

$$f_{Nd} = \frac{R_{NdFe}}{1 + R_{NdFe} + R_{NbFe}} \tag{6.11}$$

where

$$R_{XFe} = k_{XFe}\left(\frac{N_X}{N_{Fe}}\right) \tag{6.12}$$

If we write $f_i = U_i/V_i$ then the statistical error in f_i can be calculated from;

$$\left(\frac{\partial f_i}{f_i}\right)^2 = \left(\frac{\partial U_i}{U_i}\right)^2 + \left(\frac{\partial V_i}{V_i}\right)^2 \tag{6.13}$$

We can write

$$\partial U_i^2 = N_i + 2B_i \tag{6.14}$$

$$\begin{aligned} \partial V_i^2 &= \partial N_i^2 + \sum^{j \neq i} k_{ij}^2 \partial N_j^2 \\ &= N_i + \sum^{j \neq i} k_{ij}^2 (N_j + 2B_j) \end{aligned} \tag{6.15}$$

This follows if we set $G_i = N_i + B_i$ where G_i is the gross number of counts in a peak and B_i is the background, therefore;

$$\begin{aligned} N_i &= G_i - B_i \\ \partial N_i^2 &= \partial G_i^2 + \partial B_i^2 \\ &= G_i + B_i \\ &= (N_i + 2B_i) \end{aligned}$$

This correction is only necessary if the background is comparable with the net counts in the peak.

6.10 References

H.Bethe, *Ann.Physik*, **5**, p325, (1930).

J.N.Chapman, C.C.Gray, B.W.Robertson and W.A.P.Nicholson, *X-ray Spectrometry*, **12**, pp153–162, (1983).

J.N.Chapman, W.A.P.Nicholson and P.A.Crozier, *J.Microsc*, **136**, pp179–191, (1984).

G.Cliff and G.W.Lorimer, *J.Micros.*, **103**, pp203–207, (1975).

N.A.Dyson, X-rays in Atomic and Nuclear Physics 2nd Edition, Cambridge Press, (1990).

G.Elwert, *Ann.Phys*, **34**, p178, (1939).

J.I.Goldstein, J.L.Costley, G.W.Lorimer and S.J.B.Reed *SEM*, p315, ed O.Johari (iitri, O'Hare, Chicago), (1977).

J.J.Hren, J.I.Goldstein and D.C.Joy, *Introduction to Analytical Microscopy*, Plenum Press, p83, (1979).

H.W.Koch and J.W.Motz, *Rev.Mod.Phys.*, **31**, p920 (1959).

M.O.Krause ,*J.Phys.Chem*, **8**, pp307–327. (1979).

G.W.Lorimer, Proceedings of the Twenty Fifth Scottish Universities Summer School in Physics, p305, (1983).

A.McGibbon, PhD Thesis, University of Glasgow, 1989.

W.A.P.Nicholson and J.N.Chapman, *Microbeam Analysis*, p215, (1983).

J.H.Paterson, J.N.Chapman, W.A.P.Nicholson and J.M.Titchmarsh, *J.Microsc.*, **154**, pp1–17, (1988).

J.H.Paterson, PhD Thesis, University of Glasgow, 1988.

C.J.Powell, *Rev.Mod.Phys*, **48**, pp33–47, (1976).

J.M.Titchmarsh, Proceedings of the Fortieth Scottish Universities Summer School in Physics, p275, (1992).

Chapter 7

X-ray Data from Sintered NdFeB

7.1 Experimental Conditions

All the results in this chapter were obtained using the VG HB5. The specimen holder in the HB5 rests in the objective lens and must be put in the microscope well in advance (usually the night before) in order to allow it to thermally equilibriate. This minimises any thermal drift which may occur during spectrum acquisition. To avoid any problem with contamination which occurs as a result of hydocarbons being 'fixed' by the beam, the sample was vapour degreased in inhibisol before being put in the microscope. This method eliminated a common problem which had been exacerbated in the first samples as a result of incomplete removal of the the wax used in the TEM specimen preparation. As described in chapter 2, x-ray analysis can not be done with an objective aperture in place and so the microscope was operated with a 100μm VOA probe forming aperture and a 100μm SA spray aperture and with C2. The current falling on the sample was 0.2nA which, for grains thin enough to be easily imaged, produced a count rate at the detector of 3000–6000 counts/sec. The corresponding deadtime of the detector was 20–30% which is acceptable. The acquisition time was generally 30s livetime which was a compromise between obtaining good statistics and reducing the time spent acquiring - this ensures that any the area of interest does not drift off the probe.

7.2 Experimental k-factors

For every sample studied, a number of spectra were taken of the matrix phase in order that the k_{NdFe}-factor could be determined.

Figure 7.1 shows a typical x-ray spectrum from the matrix phase. The background shape is slightly flatter than expected at the low energy end of the spectrum suggesting that a small amount of absorption had taken place (see chapter 6) but this should not significantly affect the peaks of interest. The Nd $L\alpha^1$, $L\alpha^2$, $L\beta^2$ & $L\ell$-lines and the Fe K-lines are present as labelled with a slight overlap between the Fe-Kα peak and the Nd $L\beta^2$ peak. Clearly it is impossible to put background windows around each individual peak and background windows were placed on either side of the group of peaks. Twenty spectra were obtained from grains of $Nd_2Fe_{14}B$ covering each of the materials under investigation (although no difference was expected or observed). The Nd and Fe are in the ratio 1:7, this allows the k-factor to be determined. The average k_{NdFe} was calculated to be 0.639±0.011 which compares extremely well with the theoretical value of 0.65as calculated using the equations detailed in chapter 6. The experimental value was used in all subsequent calculations of composition.

7.3 Grain Boundaries

As discussed in chapter 3, the magnetic interaction between two adjacent grains is strongly influenced by the presence or otherwise of a non-magnetic Nd-rich layer (Ramesh et al, 1986).

Figure 7.2 shows a relatively low magnification image of various grains in sample A. This image is typical of all samples investigated. Areas K, L and N are clearly different in appearance from the rest of the sample suggesting that these are a different phase. Table 7.1 shows the compositions at the points marked on the micrograph. The errors quoted are the statistical errors and do not include the other sources discussed in chapter 6. Areas A, B, C, D, E, F, G, H, J and M appear to be grains of the 2:14:1 phase Any deviation from the expected Fe:Nd ratio of 0.875:0.125 is put down to the thickness of the area which may result in absorption and therefore make the results slightly less

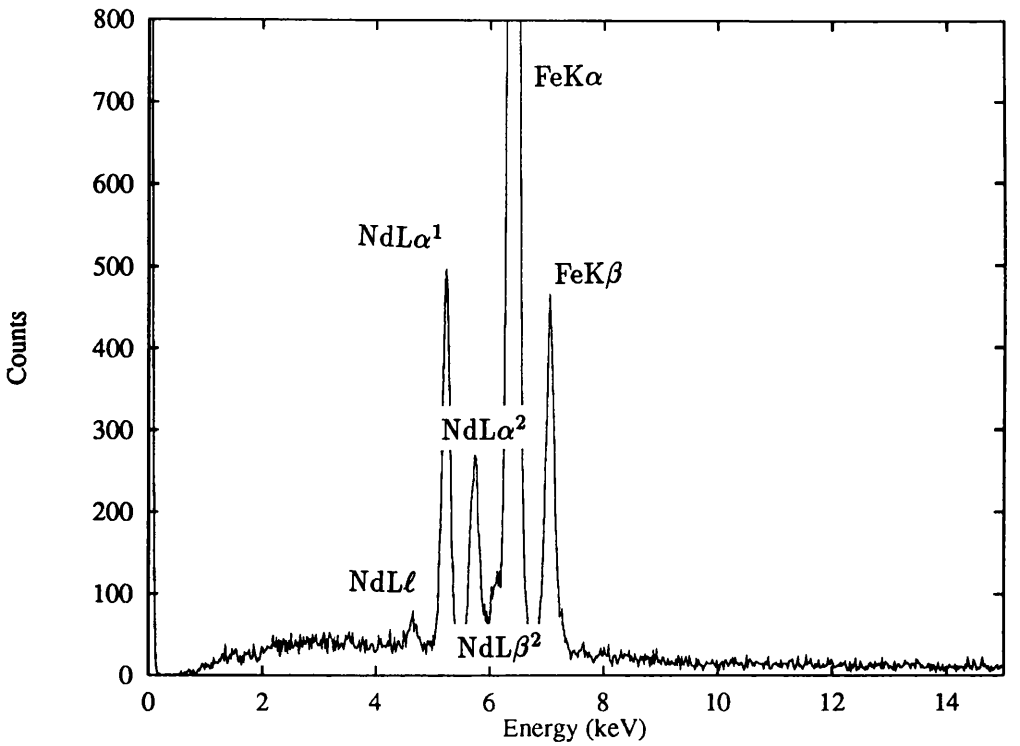

Figure 7.1: *Typical spectrum from* $Nd_2Fe_{14}B$

	%Fe	%Nd	% Nb
A	86.7±1.1	13.3±0.4	0.1±0.2
B	86.7±0.9	13.0±0.3	0.2±0.2
C	87.4±0.8	12.2±0.3	0.3±0.1
D	86.7±1.2	13.3±0.4	0.1±0.2
E	83.3±1.4	16.5±0.5	0.2±0.3
F	87.0±0.9	12.9±0.3	0.1±0.2
G	87.0±1.0	12.4±0.3	0.5±0.2
H	86.4±1.3	12.9±0.4	0.6±0.2
I	52.2±1.0	3.4±0.2	44.4±1.3
J	86.9±0.8	12.5±0.3	0.6±0.2
K	65.4±1.6	33.3±0.9	1.3±0.5
L	20.1±0.7	79.9±0.4	0.0±0.3
M	86.0±0.8	13.7±0.3	0.3±0.1
N	25.4±0.6	74.6±0.8	0.0±0.2
O	81.9±0.6	16.2±0.2	2.0±0.2

Table 7.1: *Composition at various points*

Figure 7.2: *Micrograph of grain boundaries*

accurate. Areas K, L and N are a Nd rich phase. Area I has only a very small amount of Nd and appears to be a compound of Fe and Nb - this will be discussed later. Aside from this area, the percentage of Nb observed was very low and/or with a very high error associated. This suggests that it does not dissolve easily in the matrix phase. Area O is a scan of the whole area and as would be expected, it is, on average, slightly Nd rich and Nb is present. The photographs on the left hand side of figure 7.3 show relatively low magnification images of the boundary between a grain and two of its neighbours. The photographs on the right hand side are much higher magnification images of the area within the box. X-ray analysis was undertaken on these boundaries by acquiring a 30s spectrum at 10nm intervals across them. Figure 7.4 show the percentage of Nd across the two boundaries. The difference is striking. in one case, the %Nd barely changes, rising from 12% to 15% while in the other case it rises to over 50% showing clear Nd enrichment in the boundary. One source of this difference may be the preparation method since it has been suggested that the boundary phase is preferentially etched by the ion beam (Parker et al, 1987B) but the fact that the two behaviours were observed in the same grain suggest that the grain was incompletely wetted by the liquid Nd sintering phase (see chapter 1) allowing any magnetisation reversal in one of the grains to spread to the other.

7.4 Investigation of Nb containing material

Nb is classified as a type II dopant. Allibert (1989) showed that its solubility in the $Nd_2Fe_{14}B$ matrix is only 0.4% therefore, its effect must be microstructural. This could be as a result of the grain growth being inhibited by the Nb or an increase in the number of intergranular phases leading to improved wetting between the grains. (Fidler and Knoch, 1989; Jinfang et al, 1992; Fidler, 1992A, 1992B). Despite this, it has also been observed to substitute directly for Fe at up to 15% of Fe lattice sites (Parker et al, 1987A, 1987B). In the samples investigated, the Nb was present in two distinct ways.

7.4.1 'Small' Precipitates

Figure 7.5 shows Nb precipitates on a background of $Nd_2Fe_{14}B$. These are approximately 50nm in size as observed by other researchers (Allibert, 1989; Parker et al, 1987A, 1987B).

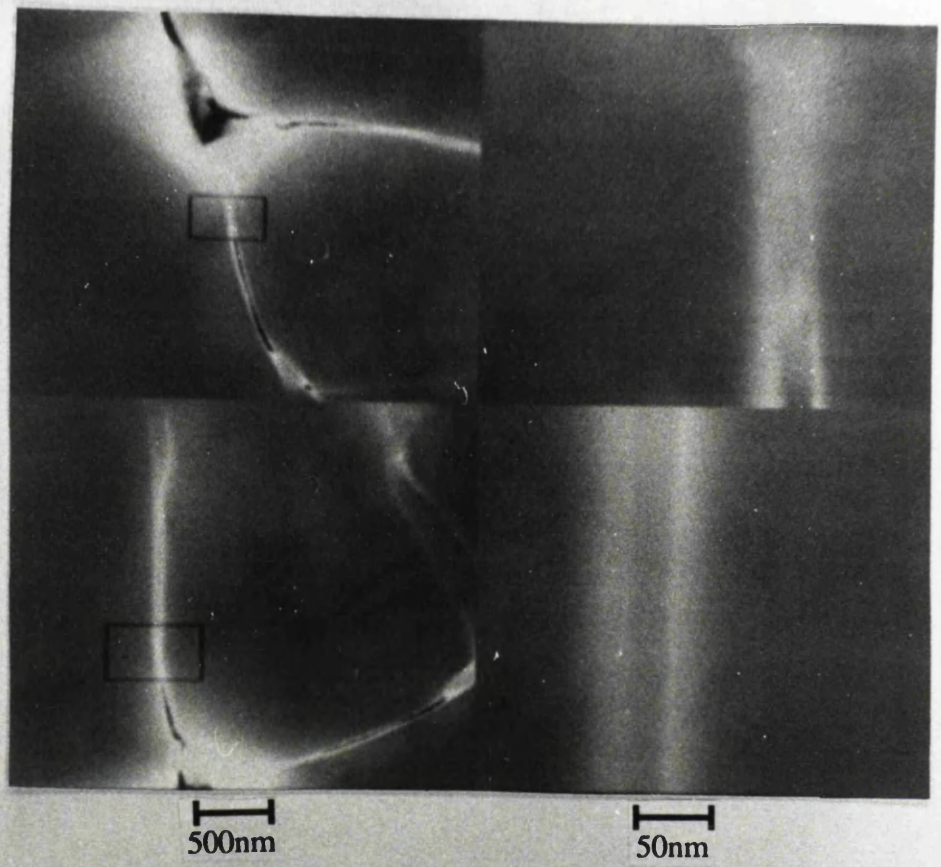

Figure 7.3: *Photograph of a grain boundary*

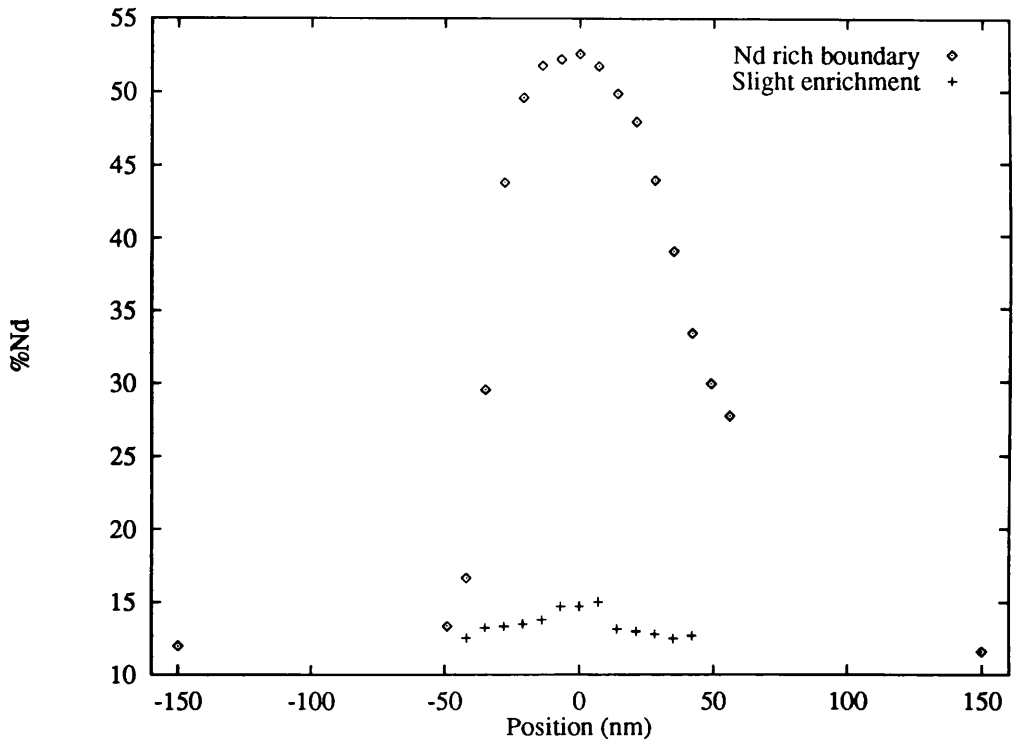

Figure 7.4: *%Nd across two grain boundaries*

The scanned probe was stopped on these precipitates and a typical spectrum from one of them is shown in figure 7.6. The spectrum shows clearly the Nb K and L lines as well as the lines from the matrix phase. In this case, the shape of the background suggests negligible absorption in the sample. The proportion of each element was calculated using a theoretical k-factor for Nb. The results denoted 'probe' are those obtained by stopping the scanned probe on the centre of the precipitate while those denoted 'area' were obtained from an area including the precipitates. Data were obtained from many grains of each of the materials; results from 7 areas are shown in table 7.2.

There is no consistent pattern throughout all the precipitates but despite this, it is still possible to observe that the compositions fall into three categories. In the precipitates marked 'sub', the percentage of Nd varies slightly while there is a large drop in the percentage of Fe. The ratio of (Fe+Nb)/Nd was calculated and was found to be roughly constant suggesting that the Nb has simply substituted for Fe at these points (Parker et al,

Figure 7.5: *Nb precipitates*

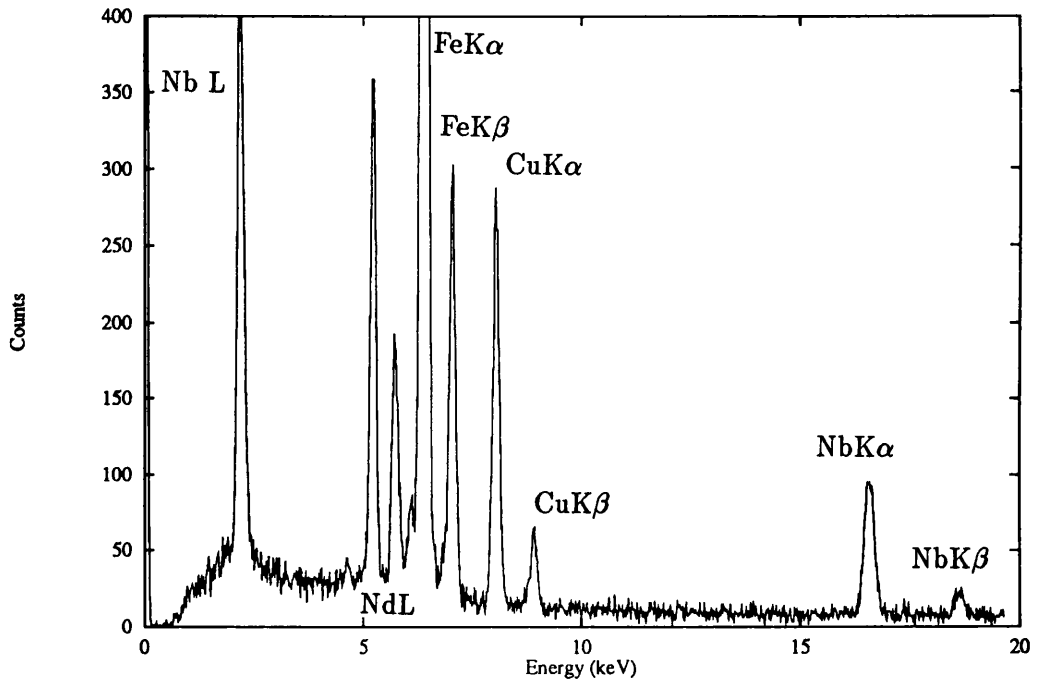

Figure 7.6: *Typical spectrum from a Nb precipitate*

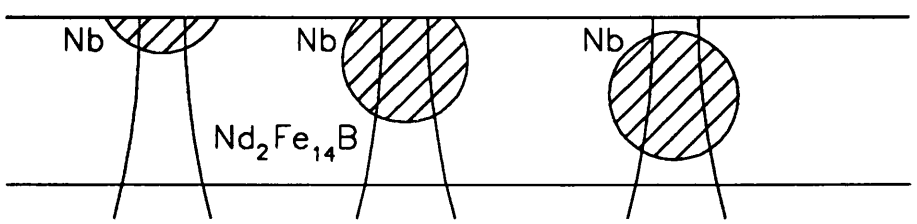

Figure 7.7: *Schematic of precipitates which have undergone varying degrees of thinning*

	%Fe	%Nd	% Nb	
Sample A				
Probe	60.4±0.7	10.4±0.2	29.1±0.6	sub
Probe	76.4±0.8	12.2±0.2	11.4±0.3	sub
Probe	77.3±0.9	12.4±0.2	10.3±0.4	sub
Area	85.0±0.8	14.8±0.2	0.2±0.04	
Probe	68.7±1.3	11.9±0.3	19.4±0.7	sub
Probe	81.3±1.5	12.5±0.4	6.1±0.4	sub
Probe	64.3±1.1	22.7±0.5	13.0±0.6	*
Area	84.3±1.4	15.3±0.5	0.4±0.1	
Probe	78.2±1.4	16.5±0.4	5.0±0.4	*
Probe	63.2±1.5	6.0±0.3	30.8±1.2	prec
Probe	53.4±1.8	18.9±0.8	27.7±1.5	prec
Area	83.6±1.5	15.2±0.4	1.2±0.2	
Sample B				
Probe	56.8±1.0	6.2±0.2	36.9 ±1.4	prec
Probe	71.4±0.8	7.4±0.1	21.1±0.6	prec
Probe	74.5±1.2	8.7±0.2	16.7±0.8	prec
Area	88.3±0.7	11.6±0.1	0.1±0.02	
Probe	55.5±1.1	6.3±0.5	38.2 ±0.4	*
Probe	58.9±1.0	18.9±0.6	22.2±0.2	*
Probe	71.5±0.7	6.9±0.3	21.6±0.1	prec
Probe	75.7±1.3	10.0±0.5	14.3±0.1	sub
Sample C				
Probe	47.2±1.4	21.5±0.7	31.3 ±1.9	*
Probe	73.0±1.5	6.7±0.3	20.2±1.2	prec
Probe	75.6±2.1	7.9±0.4	16.5±1.3	prec
Area	87.7±2.1	11.1±0.4	1.1±0.02	
Probe	78.1±0.8	11.6±0.1	10.3 ±0.3	sub
Probe	82.9±0.6	11.7±0.1	5.35±0.2	sub
Area	87.9±0.8	11.1±0.2	0.9±0.1	

Table 7.2: *Composition of grains containing Nb precipitates*

1987A, 1987B). In the precipitates marked 'prec', the percentage of Nd drops substantially and again there is a decrease in the Fe. Assuming that all the Nd is tied up in the matrix phase, the amount of Fe required to form the $Nd_2Fe_{14}B$ phase was subtracted from the %Fe; this left a surplus of Fe which was very approximately equal to the %Nb. These may be precipitates of FeNbB as observed by Schrey, (1989). In the last category, marked '*', there is a large increase in the percentage of Nd usually at the expense of Fe. These cannot be explained in a similar fashion to the previous two cases and the nature of these precipitates is unknown.

We have studied many precipitates and found Nb in the range 4-37% although the actual Nb percentages are of little value since we cannot tell how much of the volume analysed is precipitate and how much is the matrix phase. This point is illustrated in figure 7.7, three precipitates are shown which have undergone varying degrees of thinning; the volume of sample excited by the beam is also shown. It is easy to see that there will be an increase in the proportion of Nb detected but the image of the precipitates will appear very similar although the apparent size will vary.

None of the materials exhibited any preference for any one 'type' of precipitate. An area spectrum from material A is shown in figure 7.8; The Nb peaks are very small but still visible with the Nb content calculated to be 1.1% and even when the acquisition time was increased to 300 seconds in a different area where small precipitates are visible, Nb was only observed at 0.6%. As stated in chapter 3, the Nb content of these materials is 0.36% for A and 0.5% for B and C and this suggests that the Nb is not homogeneously distributed throughout the sample. The Cu Kα and Kβ peaks are also present but this is due to deposition of Cu from the specimen stage during the ion-beam thinning. Although domain wall pinning by these precipitates has been observed (Ishikawa et al, 1989) the density of such precipitates in the materials studied was not felt to be either large enough or uniform enough to produce the significant effects observed in the bulk magnetic properties, i.e. the temperature coefficients α and β are reduced by $\sim$7% and $\sim$1% respectively, the squareness of the hysteresis loop is improved and the coercivity is increased by $\sim$14% (Tokunaga et al, 1987).

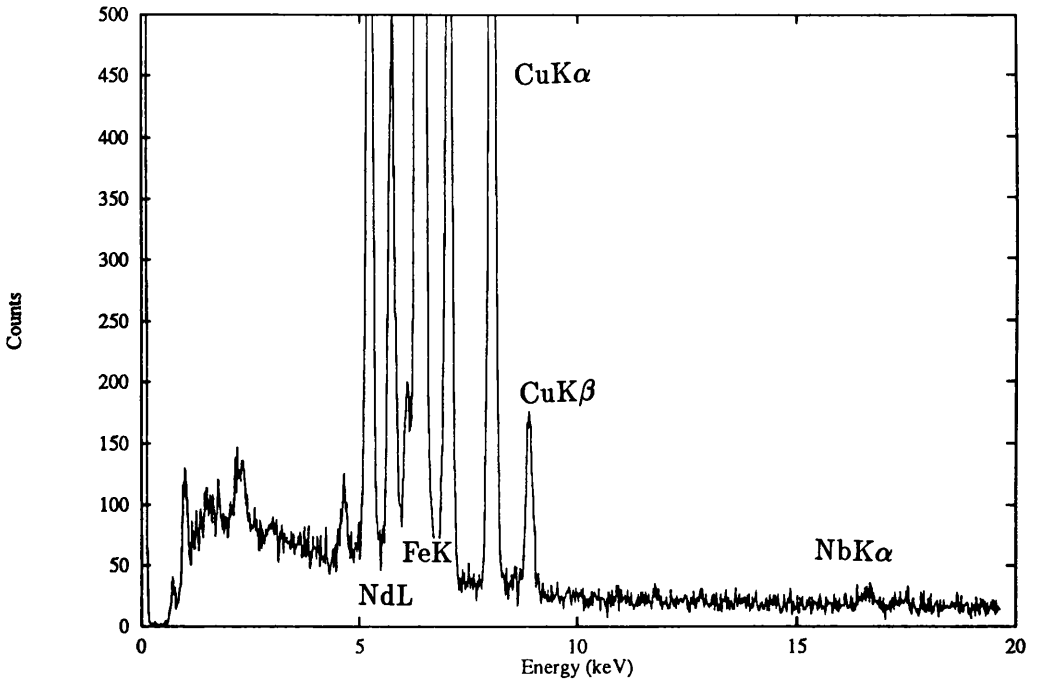

Figure 7.8: *Scan of area containing Nb precipitates*

7.4.2 Fe/Nb Compounds

The Nb was also present in the form of much larger particles, a micrograph of one of which is shown in figure 7.9 These are of the order of μm in size and a spectrum from such a particle is shown in figure 7.10. The spectrum consists mainly of the Fe and Nb peaks with very little Nd. The count rate from these particles is very high (~10kcps) indicating that they are very thick, i.e. they are resistant to the thinning, something which is suggested by the image.

Spectra were obtained and analysed from two of these features and the area surrounding them; the results are shown in table 7.3. Investigation of the surrounding area reveals it to be Nd rich suggesting that the Fe/Nb particle has prevented formation of the $Nd_2Fe_{14}B$ phase in this region. As stated earlier, it is impossible to determine what proportion of the volume analysed is the particle and what proportion is the Nd rich background although the very small amounts of Nd suggests that the particle takes up most of the volume.

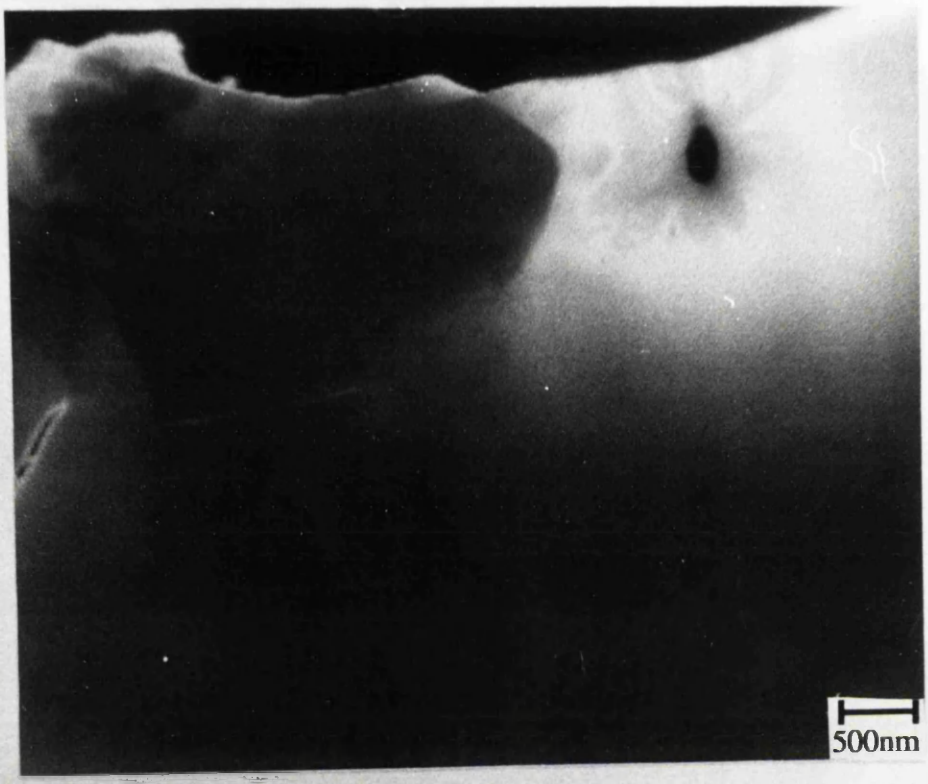

Figure 7.9: *Photograph of Fe/Nb compound*

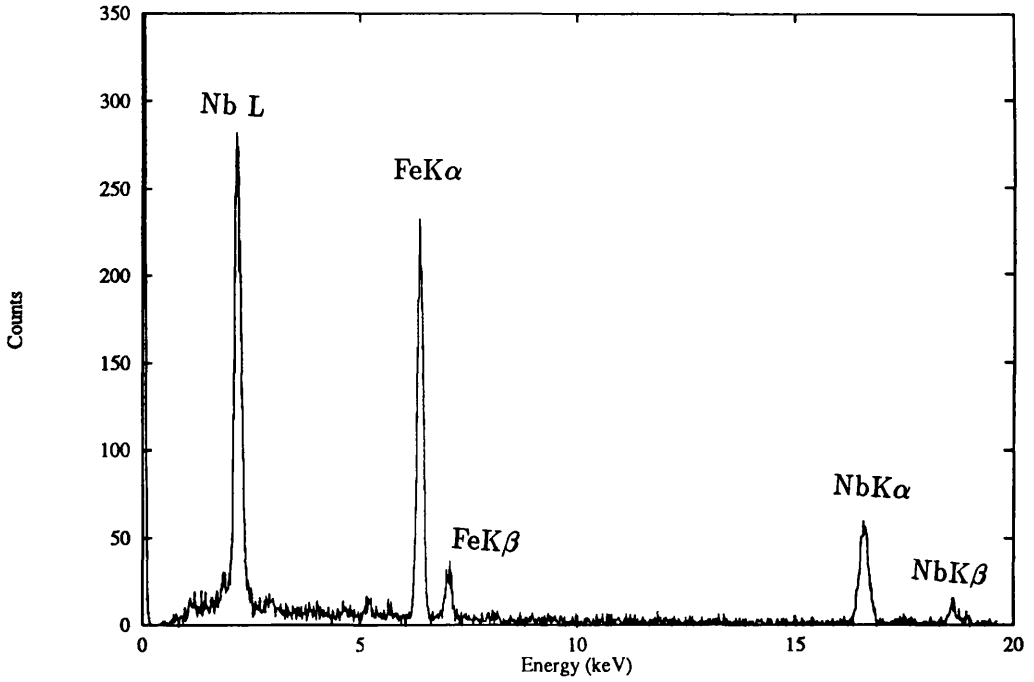

Figure 7.10: *Spectrum from a Fe/Nb compound*

Following the approach taken for the smaller precipitates, if it assumed that all the Nd detected when the probe is on the particle comes from the Nd rich background and that the relative proportion of Fe from the background is the same as that detected beside the particle then the proportion of Fe in the particle may be deduced. This again shows that the particle has similar amounts of Fe and Nb. Schrey (1988) observed μm sized features containing Fe and Nb and deduced that these were in fact coarse FeNbB particles remaining from the primary crystals in the ingot. Its presence is unlikely to improve the magnetic properties. This feature was only observed three times in all the samples investigated and so is unlikely to be of much importance.

7.5 Conclusions

EDX has been used to provide compositional information from alloys of NdFeB. It was observed that the majority of the material consists of grains of the $Nd_2Fe_{14}B$ phase plus

	%Fe	%Nd	% Nb
Fe/Nb compound - Sample A			
Probe	56.3±0.4	5.8±0.1	37.9±0.4
Area	56.0±0.7	8.3±0.2	35.7±0.7
Surrounding area			
Area	68.2±0.7	31.8±0.3	0.1±0.0
Probe	77.4±0.8	22.3±0.3	0.3±0.0
Probe	52.3±0.5	47.5±0.5	0.0±0.0
Fe/Nb compound - Sample B			
Area	50.8±1.1	23.3±0.6	25.9±1.3
Probe	52.4±0.9	3.4±0.2	44.4±1.3
Surrounding area			
Area	40.5±1.1	59.5±1.5	0.0±0.0

Table 7.3: *Composition of FeNb compound*

intergranular regions of Nd rich material (up to 80% Nd). The grain boundaries have been investigated and it has been found that while this Nd rich phase is present between some of the grains, it is not present between them all. This will limit, but not prevent, the spread of any magnetisation reversal. Nb has been observed in two forms, 50nm precipitate like features, and μm sized features. These smaller features fall into three categories; areas where the Nb has substituted into the lattice for Fe, precipitates of FeNbB and precipitates which are rich in Nd and Nb at the expense of Fe but have not be further identified. Although the smaller precipitates have Nb in the range 4–37%, an x-ray spectrum acquired from a grain where the precipitates are visible only reveals Nb to be present at a level of ~1%. This is larger than the amount in the alloy (0.36–0.5%) suggesting that the Nb containing precipitates are not homogeneously distributed throughout the material. The larger features have been identified as FeNbB and are probably particles remaining from the primary crystals in the melt. They are generally to be found in a Nd rich region suggesting that, at these points, the Fe and Nb have not been free to allow formation of the $Nd_2Fe_{14}B$ phase, therefore leaving the Nd to form other phases. No obvious differences were found in the behaviour of Nb in the three materials.

7.6 References

C.H.Allibert, *J.Less Common Metals*.**152**. L1 (1989).

J.Fidler, *Proceedings of VII International Symposium on magnetic anisotropy and coercivity in rare-earth transition metal alloys*, Australia, pp11–22, July 1992.

J.Fidler, *Magnetism, Magnetic Materials and their applications*, Cuba, May 1991.

J.Fidler and K.G.Knoch, *J.Mag.Mag.Mat*, **80**, pp48–56, (1989).

T.Ishikawa, Y.Hamada and K.Ohmori, Paper No 19P0212 10th International Conference on Rare-Earth Magnets and Their Applications (1989).

L.Jinfang, L.Helie and W.Jiang *J.Mag.Mag.Mat*, **103**, pp65–72, (1992).

S.F.H.Parker, R.J.Pollard, D.G.Lord and P.J.Grundy, *IEEE Trans.Mag*, **MAG-23**, p2103, (1987A).

S.F.H.Parker, P.J.Grundy and J.Fidler. *J.Mag.Mag.Mat*, **66**, p74, (1987B).

R.Ramesh, J.K.Chen and G.Thomas, *J.Appl.Phys*, **61**, pp2993–2998, (1987).

P.Schrey, *J.Mag.Mag.Mat*, **73** , pp260–262, (1988).

M.Tokunaga, H.Harada and S.R.Trout. *IEEE Trans.Mag.*, **23**, pp2284–2286, (1987).

Chapter 8

Melt-Spun NdFeB alloys

This work was done in conjunction with Professor H.A.Davies and the group in the department of Engineering Materials at the University of Sheffield. Much work has been done at Sheffield to investigate the microstructure of these materials and also to measure the bulk magnetic properties. The aim in this collaboration was to find out more about the domain structure and behaviour. The production of melt-spun materials was discussed in chapter 3. The surface velocity of the copper wheel, V_r, was 18–20m/s. Croat et al (1984) produced samples at three different wheel speeds and found that the optimum speed was 19m/s, this produced the highest coercivity and energy product. Manaf et al (1991) prepared samples with V_r=13–48m/s and found that the best properties were obtained over a wide range of V_r i.e. 14–20m/s. Samples with the following compositions were prepared;

$Nd_{9.5}Fe_{84.5}B_6$

$Nd_{12}Fe_{82}B_6$

$Nd_{14}Fe_{80}B_6$

The magnetic properties of ribbons with these same compositions were measured using a VSM equipped with a superconducting magnet with a maximum field of 5T, these are listed in table 8.1. It is clear that as the Nd content increases and the Fe content decreases, the saturation magnetisation and the energy product decrease. This is as a result of the reduction in the proportion of the $Nd_2Fe_{14}B$ phase. Since the thickness of the ribbons produced is only $\approx 40\mu$m, sample preparation involved simply glueing small

Alloys	H_c(kOe)	M_r(kG)	$(BH)_{max}$(MGOe)
$Nd_{9.5}Fe_{84.5}B_6$	6.3	11.0	19.8
$Nd_{12}Fe_{82}B_6$	10.5	9.7	18.7
$Nd_{14}Fe_{80}B_6$	16.5	8.4	15.6

Table 8.1: *Magnetic properties of melt-spun ribbons*

pieces of the material to copper washers and then ion beam thinning them, using the same conditions as for the sintered samples, to produce TEM samples (see chapter 3).

8.1 Magnetic Structure

Characterisation of the magnetic structure was carried out using the JEOL 2000-FX. Imaging conditions were as discussed in chapter 4; for each sample a BF image and a pair of orthogonal Foucault images were obtained. Fresnel images were obtained but were not found to be useful since wall contrast was obscured by the microstructure.

8.2 Results

For each area of each material investigated a mean value for the crystallite size and the domain width have been determined. In addition, the figures in brackets after each figure are the minimum and maximum values found. In order to get a characteristic value for the domain width, the number of domains in a given distance perpendicular to the mapping direction in a Foucault image was measured at three locations on each micrograph. This is the 'mean' domain width quoted below. Figures 8.1 and 8.2 show two sets of three images of areas of $Nd_{9.5}Fe_{84.5}B_6$. In the first area, the mean grain size is $\approx$20nm (10–60nm). The domain structure is very irregular but the domain width appears to be larger in the thicker areas of the sample. The mean width was 120nm (45–150nm). In the second area, the grain size has a mean value of 80nm (50–110nm). As mentioned in chapter 3 this occurs when the melt is not cooled quickly enough and grain growth takes place. It is believed that this can occur when an air bubble becomes trapped between the melt and the copper wheel providing sufficient insulation to allow grain growth. The mean domain width was 330nm but domains as wide as 700-800nm can be seen.

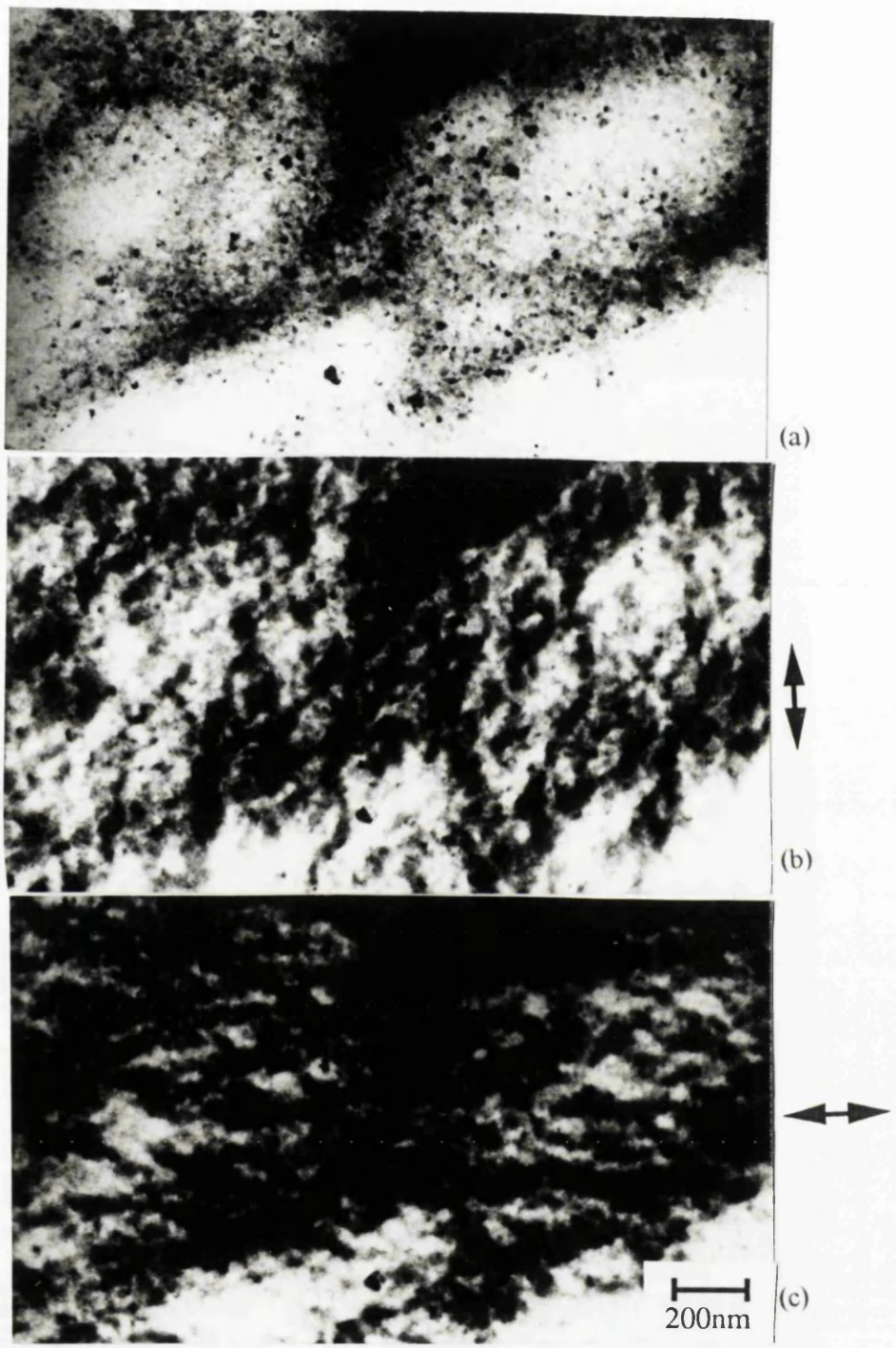

Figure 8.1: *(a) BF image of $Nd_{9.5}Fe_{84.5}B_6$, (b), (c) Orthogonal Foucault images*

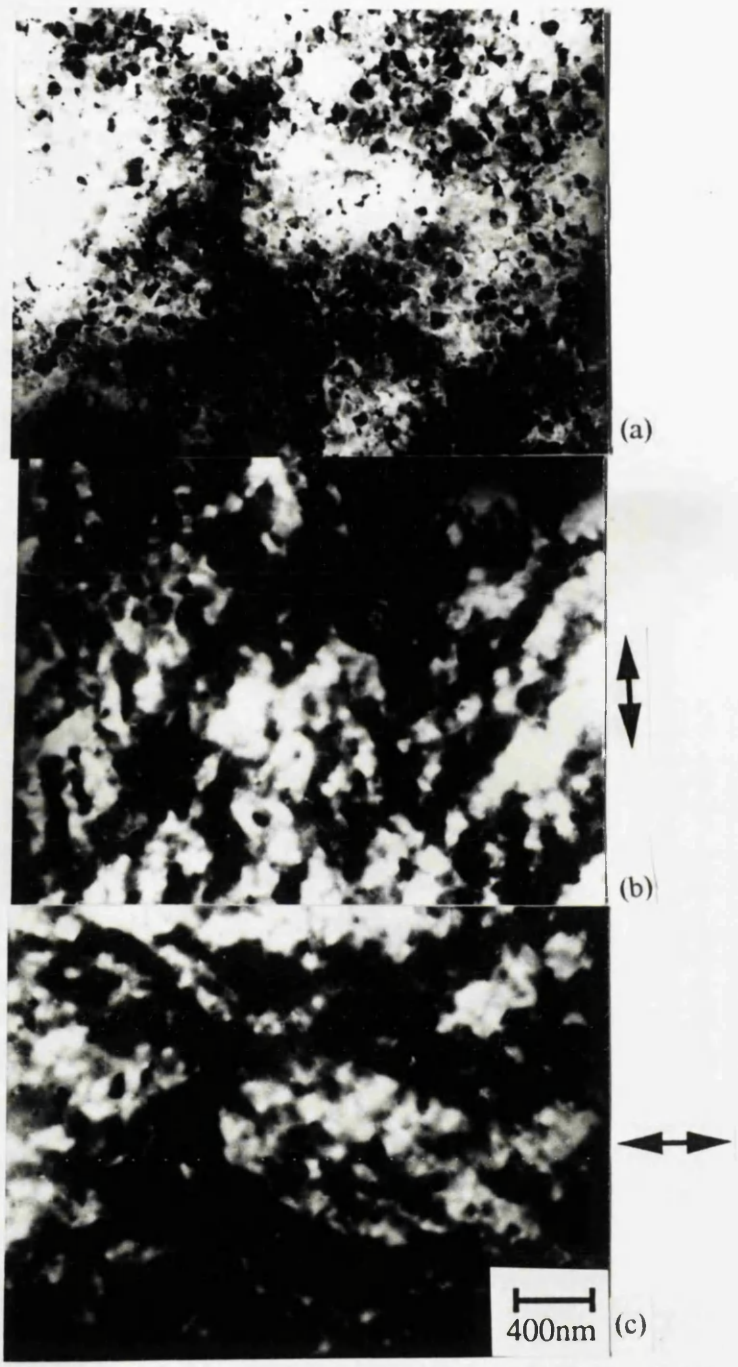

Figure 8.2: *(a) BF image of $Nd_{9.5}Fe_{84.5}B_6$, (b), (c) Orthogonal Foucault images*

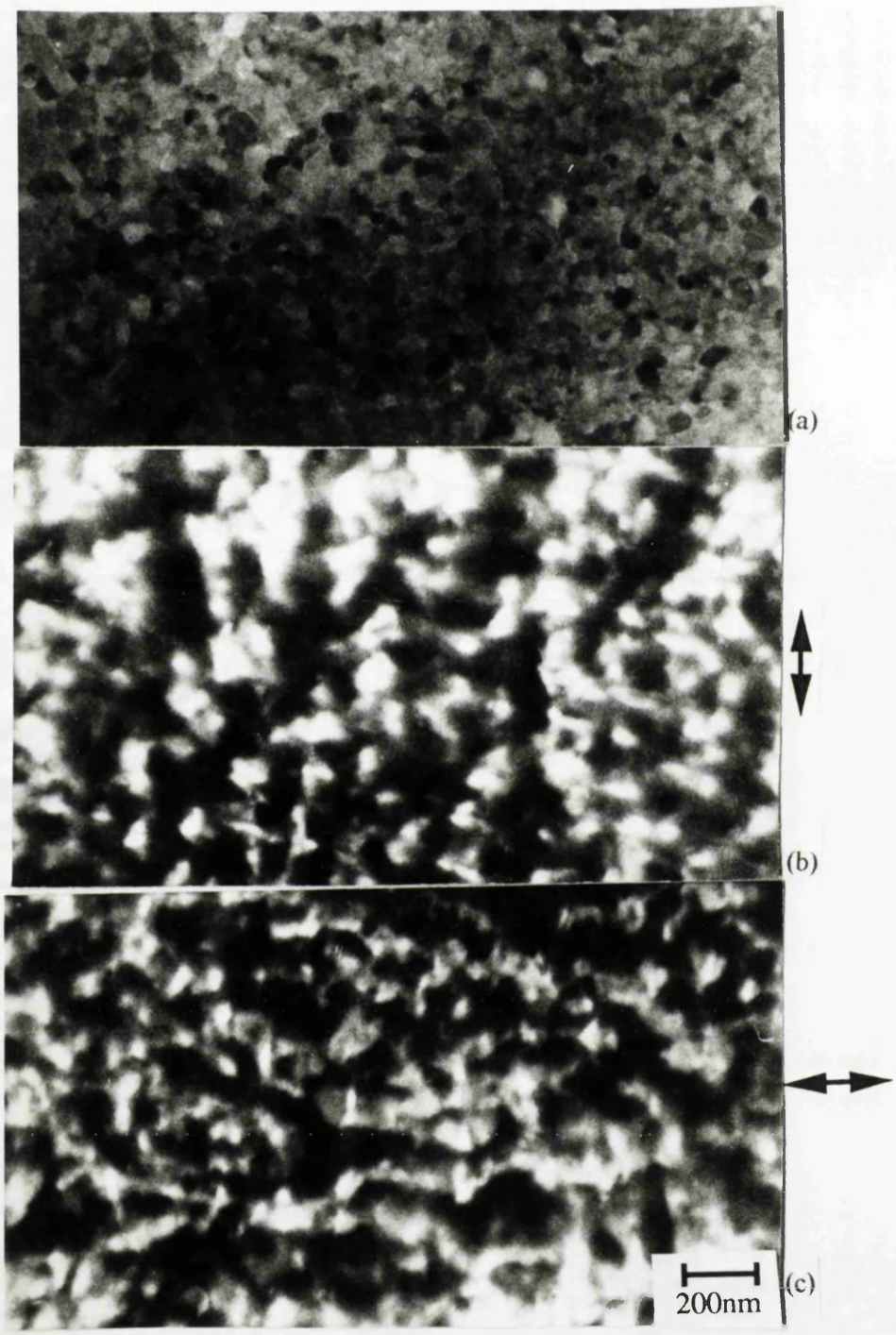

Figure 8.3: *(a) BF image of $Nd_{12}Fe_{82}B_6$, (b), (c) Orthogonal Foucault images*

In sample $Nd_{12}Fe_{82}B_6$ it was only possible to find areas where grain growth had occured despite subjecting the sample to further thinning. The mean grain size was 60nm (15–80nm). The domain width was on average 170nm (60–300nm). The grain size was larger than desired or expected.

In the third sample, $Nd_{14}Fe_{80}B_6$, large areas with a grain size of ≈20nm (15–30nm) were observed. The domain width was 80nm (40–100nm) but despite similar variations in thickness to those observed in the first sample, the domain width varies much less and the domain structure is more regular than before.

8.3 Conclusions

It is apparent from the two areas investigated in the first sample that the domain width increases with increasing crystallite size. The mean domain width is slightly smaller than, but still comparable with, that observed in sintered materials. On the other hand, minimum domain sizes are significantly smaller than those observed in sintered material. As stated in chapter 3, the critical limit at which a crystallite of $Nd_2Fe_{14}B$ will support only a single domain is ~30nm and some of the domains observed here are approaching this limit . At the other extreme, the largest domains in the second sample are undesirable since this implies significant amounts of exchange coupling between the grains. If the first and third samples are compared it can be seen that although regions were found where the grain sizes are similar, the mean domain width is smaller in the latter case. This may well be as a result of the increased Nd content suggesting that the Nd leads to a reduction of the coupling between the grains which is desirable. This is reinforced by the data in table 8.1 which shows a significantly larger coercivity for $Nd_{14}Fe_{80}B_6$ although at the expense of the energy product. In sintered materials, this is associated with, amongst other factors, much better isolation of the grains and it is reasonable to assume that this also occurs in melt-spun materials.

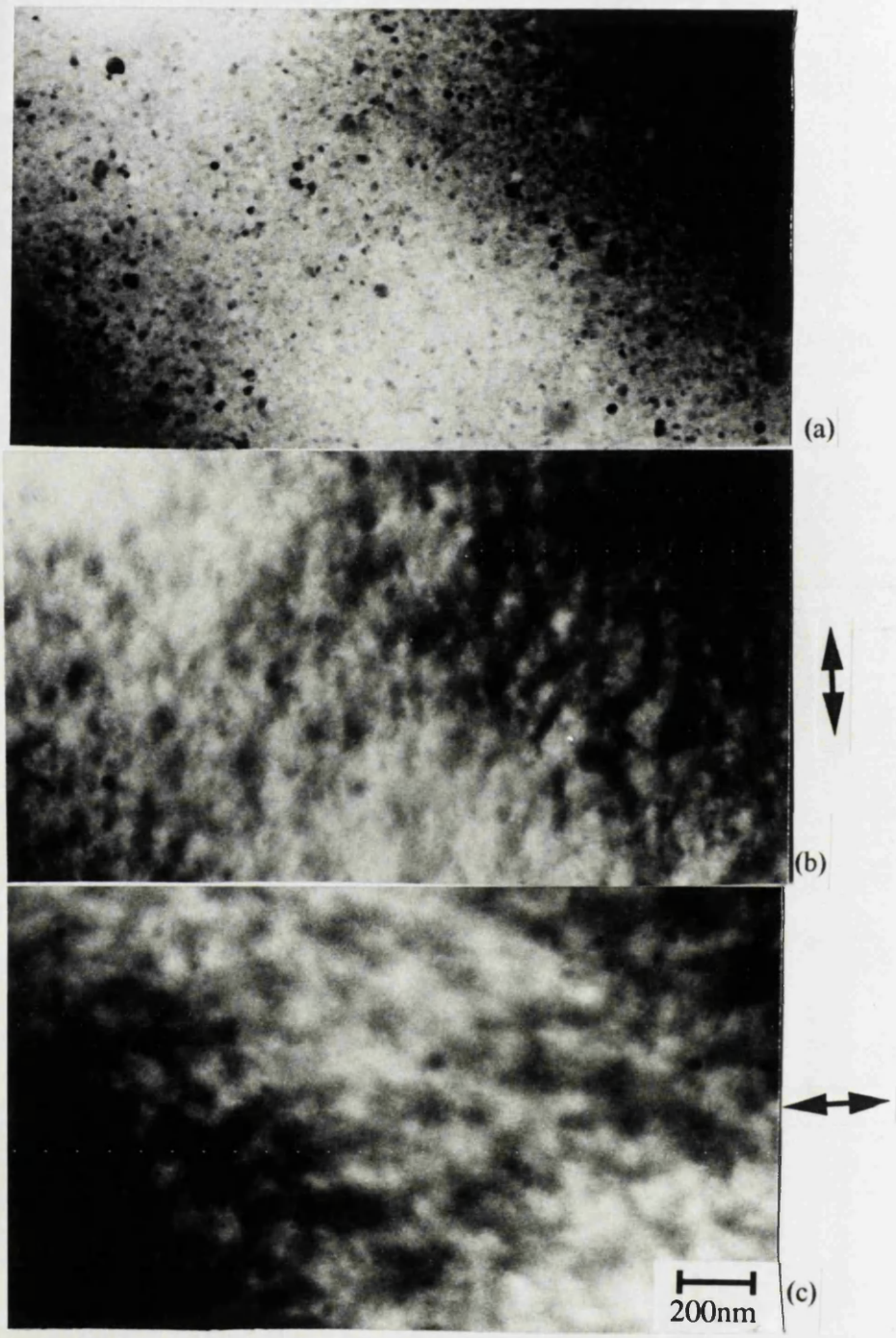

Figure 8.4: *(a) BF image of $Nd_{14}Fe_{80}B_6$. (b), (c) Orthogonal Foucault images*

8.4 References

J.J.Croat, J.F.Herbst, R.W.Lee and F.W.Pinkerton. *J.Appl.Phys.*, **55**, p2078.

A.Manaf, M.Leonowicz, H.A.Davies and R.A.Buckley, *J.Appl.Phys.*, **70**, pp6366–6368, (1991).

A.Manaf, M.Al-Khafaji, P.Z.Zhang H.A.Davies. R.A.Buckley and W.M.Rainforth, *J.Mag.Mag.Mat.* **70**, pp307–312, (1993).

A.Manaf, P.Z.Zhang, I.Ahmad, H.A.Davies and R.A.Buckley, *IEEE Trans.Mag.*, To be published (1993).

H.A.Davies, Proceeding of NATO ASI Nanophase Materials, Corfu July 1993 A.Manaf, R.A.Buckley and H.A.Davies, *J.Mag.Mag.Mat.*, **128**, pp302–306, (1993).

Chapter 9

Magnetoresistive Multilayers

This area of work, while still involving magnetic materials, was an extension of the x-ray analysis side of the project.

9.1 Material Background

A magnetoresistive material (MR) is one whose electrical resistivity varies with applied magnetic field. The simplest type of magnetoresistance is the galvomagnetic effect which occurs in current carrying conductors under the influence of a magnetic field (Ciureanu and Middelhoek, 1992, p254). There are three distinct effects which are classified according to the relative orientations of the current flow and the magnetic field i.e.

- The longitudinal effect in a longitudinal field where the current and magnetic field are parallel and the effect is measured parallel to the current - this is known as the longitudinal magnetoresistance, $\rho_{||}$.
- The longitudinal effect in a transverse field where the current and magnetic field are perpendicular and the effect is measured parallel to the current - this is known as the tranverse magnetoresistance, $\rho_{\perp}$.
- The tranverse effect in a transverse field where the magnetic field, the current and the direction in which the effect is measured are mutually perpendicular - this is the Hall effect.

In an ordinary non-magnetic conductor, both $\rho_{||}$ and $\rho_{\perp}$ increase with field (Chien et al 1993). If the current carrying conductor is ferromagnetic then anisotropic magnetoresistance may be observed. In this case, the interaction of the domain structure with the magnetic field will influence both $\rho_{||}$ and $\rho_{\perp}$. These quantities do not vary identically with applied field; in fact $\rho_{||}$ increases and $\rho_{\perp}$ decreases with field. The anisotropic magnetoresistivity, $\Delta\rho$, is defined as the maximum difference between the two i.e. $\Delta\rho = \rho_{||} - \rho_{\perp}$. The variation of the resistivity, ρ, of the materials is given by the following equation;

$$\rho = \rho_0 + \Delta\rho \cos^2\theta \tag{9.1}$$

where ρ_0 is the resistivity in the absence of a field and θ is the angle between the applied field and the current density. This equation is illustrated in figure 9.1. In order to maximise both the sensitivity and linearity of the sensor, it must be operated at $\theta \simeq 45°$. It can be shown that the resistivity varies in a similar fashion as a function of applied field (Ciureanu and Middelhoek, 1992, p291; NATO Summer School, 1992) but the sample must be 'biased' by applying a constant magnetic field so that the sensor is operating in its most sensitive region. The applied field must be along the hard axis since application of the field along the easy axis would not affect the domain structure significantly since the majority of moments will already be in the direction. In addition, the response of the magnetisation will be linear over as large a range of applied field as possible (see figure 9.1) and a relative magnetic permeability of several thousands can be obtained (μ_r=M_s/H_K). Application of the magnetic field can be done using a current carrying conductor but is more elegantly achieved using permanent magnetic films sputtered over the sensor (Hill et al, 1987; Hill and Birtwistle, 1987).

The materials discussed here are multilayers whose basic unit consists of NiFe layers separated by a spacer layer which is either Cu or Ta. They are used in magnetoresistive sensors for detection of very small magnetic fields - down to 10^{-5}Oe (Hill and Birtwistle, 1987; Hill et al, 1989; Hoffman et al, 1983, 1984, 1986). For maximum sensitivity, we require the films to have as small a coercivity as possible and for this to be achieved, it is necessary to understand the physical mechanisms at work in multilayer systems e.g. the coupling between magnetic layers. This can be done by investigating multilayers

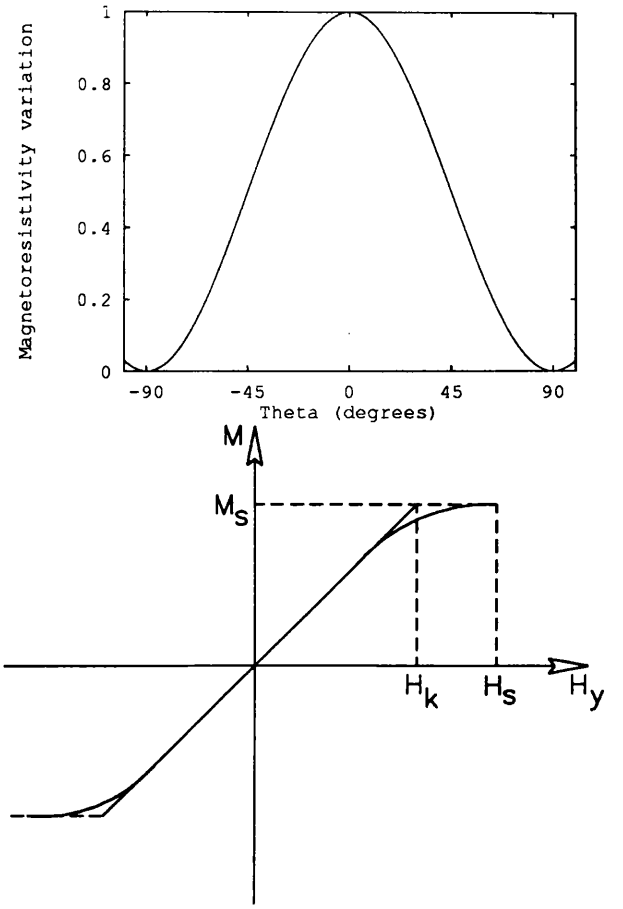

Figure 9.1: *Graph of the variation of resistivity with θ; Hard axis hysteresis loop*

which consist of permalloy and a non-magnetic spacer layer (Hill et al, 1991; Hill and McCullough, 1988).

9.2 Sample Preparation

The samples were prepared by Dr E.W.Hill and colleagues in the Department of Electrical Engineering at Manchester University by electron beam evaporation onto glass substrates. This was done in an applied field of 300Oe with the substrate temperature maintained at either 40 or 300°C. Details of each sample are shown in table 9.1. TEM cross section samples were prepared by sandwiching the films between two glass sheets. The sandwich

NiFe Å	Spacer layer	NiFeÅ	Temp (°C)	Coercivity (Oe)
500	50Å Cu	500	40	0.25
500	50Å Cu	500	300	2.87
500	50Å Ta	500	300	0.3

Table 9.1: *Properties of samples investigated*

was then sectioned using a diamond saw and 3mm discs were drilled. The sample was then thinned mechanically and finally using ion milling as described in chapter 3.

The work was carried out on the HB5 using the same conditions as those described in chapter 7. Digital images were obtained of the interfaces and then x-ray spectra were obtained at 10nm steps across them. Spectrum acquisition time was again 30 seconds. This produced spectra with peak counts for Ni and Fe of $\simeq$10000 and $\simeq$1000 respectively in the permalloy region whilst in the spacer layer, peak counts were $\simeq$500 for Cu and $\simeq$2000 for Ta.

9.3 Results

Figure 9.2 shows a bright and a dark field image of each of the multilayers. It appears that the spacer layer can be seen in the room temperature Cu sample but given the similar atomic numbers of Ni, Fe and Cu it would be expected that there would be little contrast between them and so this is likely to be an artefact of the imaging conditions. There is little evidence of the spacer layer in the high temperature sample. Ta, on the other hand, has a much greater atomic number resulting in much more atomic number contrast and clearly revealing the Ta layer. At this scale, the Ni/Fe-Ta interface appears to be smooth and the Ta layer appears to be continuous. The compositions were deduced using similar equations to those given in chapter 6. This was done using theoretical k-factors involving the Fe, Ni and Cu K-lines and the Ta L-lines. The k-factors are shown in table 9.2. Following the discussion of the accuracy of theoretical k-factors in chapter 6, the values given in the table were deduced to be accurate to approximately $\pm$11%.

Figures 9.3, 9.4 and 9.5 show the variation in the composition across the interface in each sample. The position of the glass substrate is marked on each graph. When the two

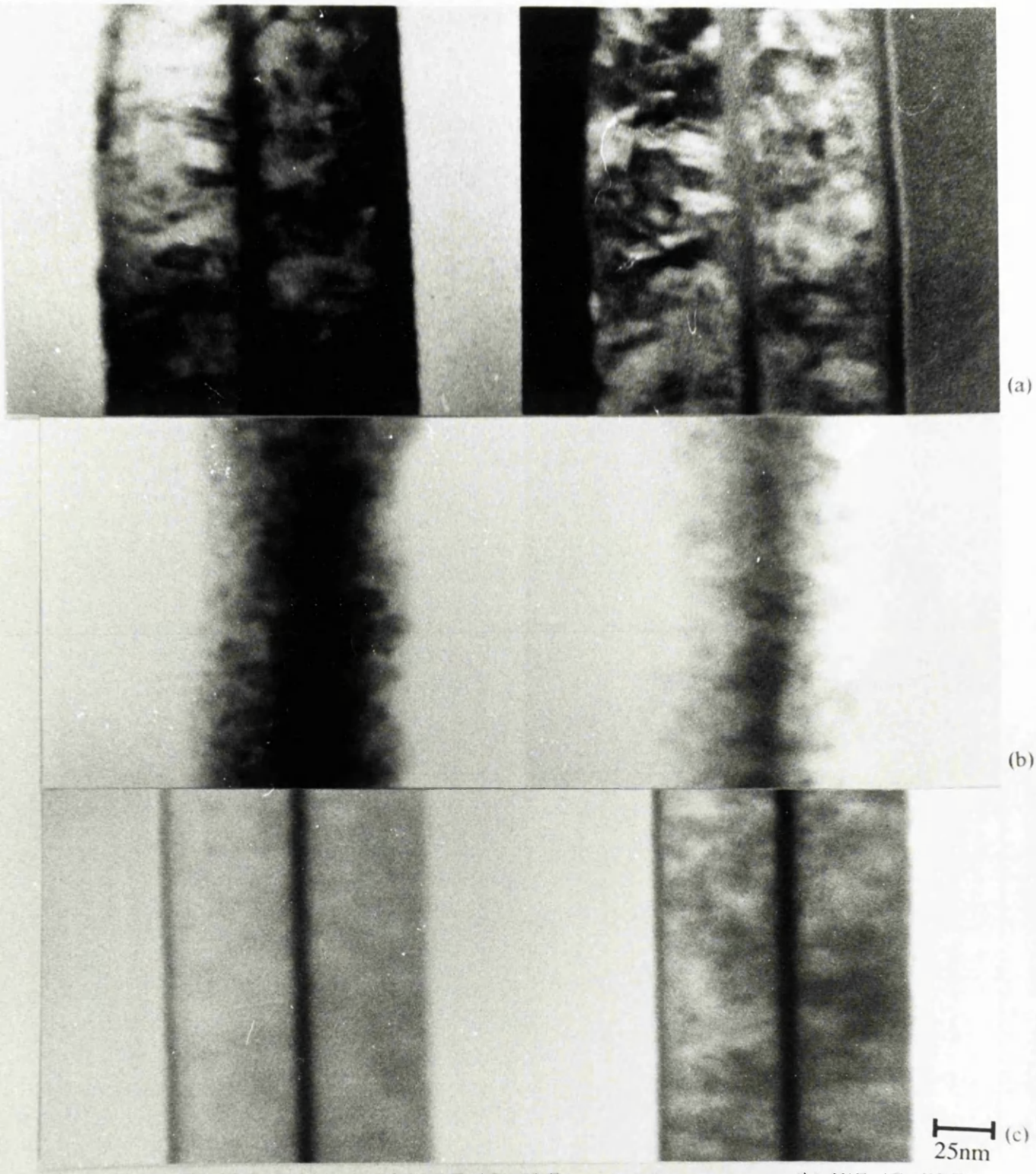

Figure 9.2: *Photographs of (a) NiFe/Cu/NiFe grown at room temp, (b) NiFe/Cu/NiFe grown at 300° C and (c) NiFe/Ta/NiFe*

k_{XFe}. X=	Value
Ni	1.090
Cu	1.066
Ta	0.702

Table 9.2: *Theoretical k-factors*

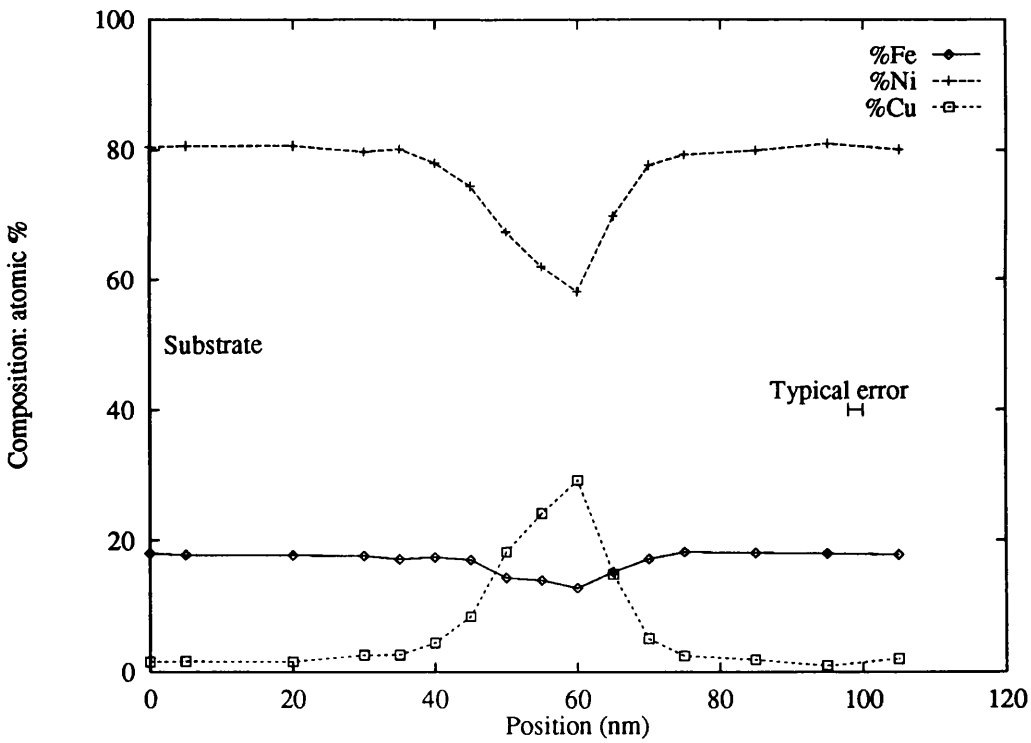

Figure 9.3: *Percentages of Ni, Fe and Cu across the interface; room temp sample*

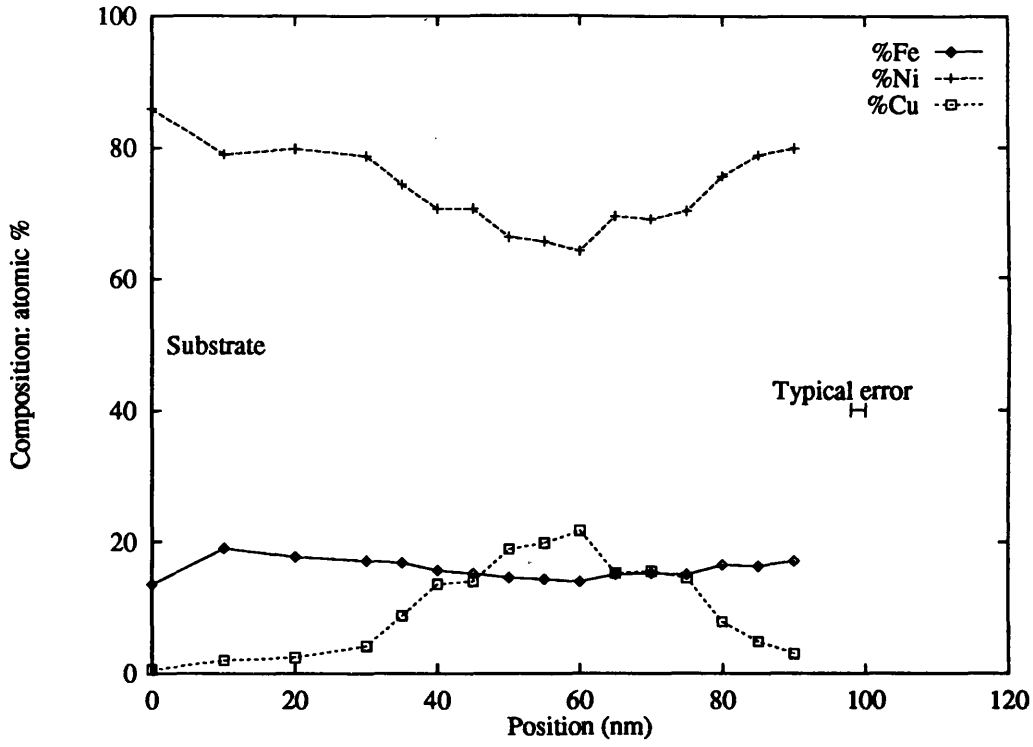

Figure 9.4: *Percentages of Ni, Fe and Cu across the interface; high temp sample*

samples with Cu spacer layers are compared, it is clear that there is a marked difference in the distribution of the Cu across the boundary. The lower temperature evaporation has produced a much sharper boundary whereas in the high temperature evaporation, the Cu has diffused further into the NiFe layers. This is not surprising since there will be increased diffusion at higher temperatures which will certainly lead to a much rougher interface between the permalloy and Cu layer. The Cu distribution in the room temperature is asymmetric within the limits of the error and there is a suggestion that this may also be the case for the high temperature sample. Further work is required to explain exactly why the Cu diffuses into the lower NiFe layer but the subsequent NiFe layer does not diffuse as far into the Cu layer. The rougher interface is expected to increase the coupling between the permalloy layers (Hill et al, 1991; Hill and McCullough, 1988) and thereby increase the coercivity as the measurements confirm. The Ta containing sample shows a sharper interface than that of Cu at the same evaporation temperature. This is a result of the

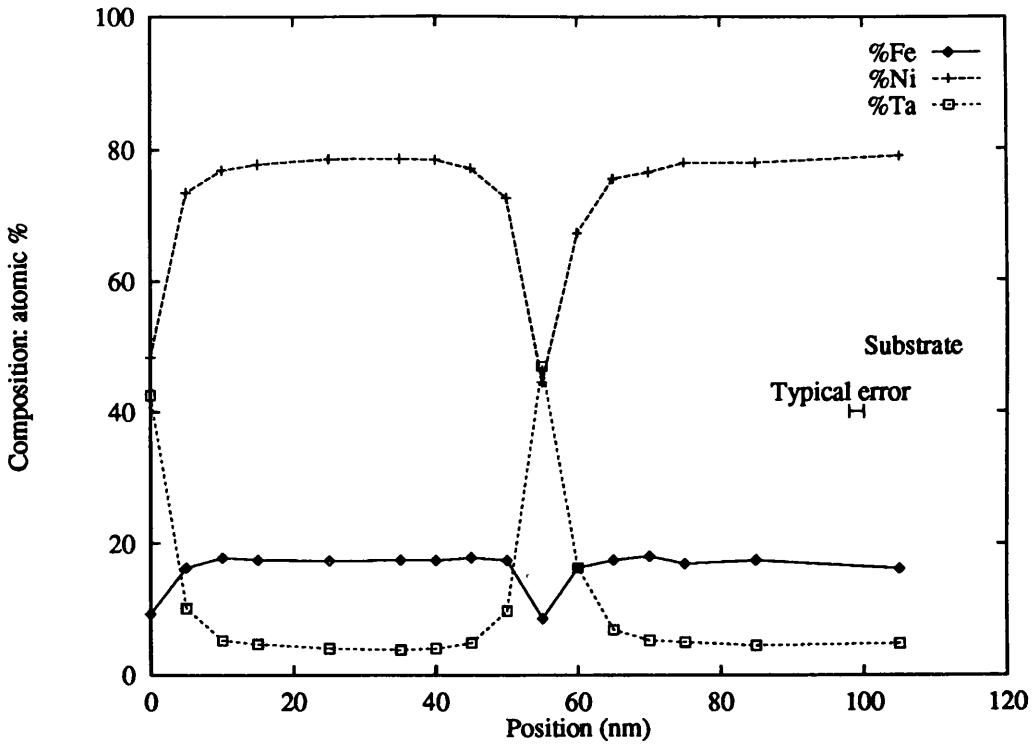

Figure 9.5: *Percentages of Ni, Fe and Ta across the interface*

permalloy/tantalum interface being chemically stable even at high temperature (Hill et al, 1991). As a consequence, the coupling between the NiFe layers will be greatly reduced and the coercivity will again be reduced. Figure 9.6 shows the ratio of Ni to Fe across the interface for each sample which is clearly very consistent except in the spacer layer and at the substrate. This suggests that the Ni and Fe diffuse at different rates into the Cu. Clearly it is to be expected that different elements diffuse at different rates but given the proximity of these two in the periodic table the difference shown in the graph is surprising and inexplicable at this stage. The total variation in the ratio, excluding the values in the spacer layer, is $\pm 5\%$ emphasising the consistency of the method.

9.4 References

C.L.Chien, J.Q.Xiao and J.S.Jiang, *J.Appl.Phys.*, **73**, pp5309–5314, (1993).

P.Ciureanu and S.Middelhoek, Thin Film Resistive Sensors IOP Publishing, (1992).

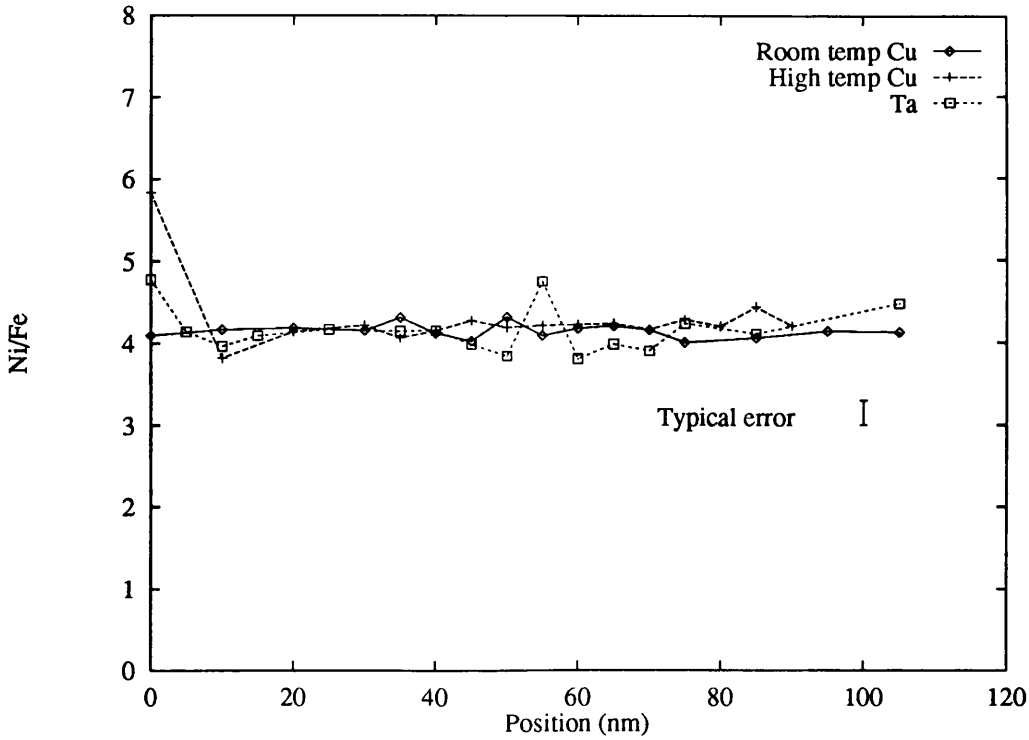

Figure 9.6: *Ratio of Ni to Fe in each sample*

E.W.Hill and J.K.Birtwistle, *IEEE Trans.Mag.*, **MAG-23**, pp2419–2421, (1987).

E.W.Hill, D.S.Halter and J.K.Birtwistle. *IEEE Trans.Mag.*, **MAG-25**, pp3836–3638, (1989).

E.W.Hill, J.P.Li and J.K.Birtwistle. *J.Appl.Phys.*, **69**, pp4526–4528, (1991).

E.W.Hill, J.P.Li and J.K.Birtwistle. *J.Appl.Phys.*, (1992).

E.W.Hill, S.L.Tomlinson and J.P.Li. PACS nos: 75.70.Cn, 75.50.Rr, 68.65.+g, 75.70.Bb.

G.R.Hoffman, J.K.Birtwistle and E.W.Hill *IEEE Trans.Mag.*, **MAG-19**, pp2139–2141, (1983).

G.R.Hoffman, E.W.Hill and J.K.Birtwistle *IEEE Trans.Mag.*, **MAG-20**, pp957–959, (1984).

G.R.Hoffman, J.K.Birtwistle and E.W.Hill *IEEE Trans.Mag.*, **MAG-22**, pp949–951, (1986).

Proceedings of NATO Summer School, Erice. (1992), to be published.

Chapter 10

Conclusions and Future Work

10.1 Conclusions

Transmission Electron Microscopy has been used to investigate the magnetic structure and behaviour of both sintered and melt-spun NdFeB alloys. The domain structures in sintered NdFeB were observed and it was found that the domain period varied between grains. This was explained in terms of the energy minimisation of the various terms introduced in chapter 1 and the inclination of the c-axis of the grain with respect to the grain normal i.e. the larger the value of θ, the larger the domain period and the straighter the domain walls will be. The variations of P with θ was investigated for each of the three materials and it was found that for a given value of θ, P was higher for materials B and C than for A.

The behaviour of domain walls at grain boundaries was also studied. Many types of behaviour have been observed and these have been described in terms of the orientation of the c-axes in the individual grains and the orientation of the boundary. We have observed instances where the walls appear to cross the boundary unhindered and also where the continuation of walls to the edge of the grain would lead to excess magnetostatic energy and therefore, the domains have terminated before the boundary. In other situations the walls seem to be independent i.e. domain walls from one grain meet the boundary in the middle of a domain in the other grain. The microscope used to image the domains at boundaries is not equipped to allow x-ray analysis to be carried out so it was not possible

to determine if a grain boundary phase was present but in some of the situations observed where the walls appear coupled it may be reasonable to assume that it is not, although such structures may arise simply through magnetostatic coupling.

The data describing the variation of P with θ was put into an energy minimisation model - the Kooy and Enz model. This model allows calculation of a parameter τ which is defined to be the ratio of the specific domain wall energy to the maximum magnetostatic energy. It was calculated using the values of P,θ and d. In the first material this produced a relatively constant value of τ with respect to θ suggesting that it is a fundamental parameter of the material. The second and third materials showed slightly decreasing values of τ with θ which cannot be easily explained. Some manipulation of the model and further calculation showed that the energy minimum becomes much shallower at higher values of θ which would make these values less reliable. For each material, a simple average was taken to get a single value of τ and the measured value of M_s was used to calculate σ_w. The domain wall energies were found to be very similar for each of the materials. Although the anisotropy field is greatly increased by the addition of Dy to materials B and C, the exchange field is decreased by a similar factor and the wall energy does not change significantly. The variation in these parameters is predicted to lead to a reduction in the domain wall width which will contribute to the increased coercivity observed in bulk materials. In order to support the application of the model to these materials, some magnetising experiments were undertaken to assess how closely the movement of the walls conformed to the models predictions. The domain period increases as the model predicts at low fields but at higher fields ($>\sim$0.5T) the measured domain period appears to be significantly smaller than the expected value. Incorporation of a demagnetising factor to take account of the finite extent of the grains would improve this but a more significant factor is that the model requires that the field be applied along the easy axis which was not the case. As a result, the effective applied fields are smaller than they appear. Domain wall pinning has also been observed in these experiments but only up to fields of approximately 0.5T.

In chapter 7, compositional information of sintered materials was obtained using EDX. No identifiable differences were found between the samples. They all consisted of 3-10μm $Nd_2Fe_{14}B$ grains with Nd rich areas present between some of the grains. The distribution

of Nb was investigated and was found to be present in two distinct ways i.e. small ~50nm precipitates and ~2μmfeatures. The smaller precipitates can be further subdivided into regions where the Nb appears to have substituted directly for Fe in the matrix and genuine precipitates of what is deduced to be FeNbB. This still leaves precipitates which have not been identified and no explanation has been offered for these. It is suggested that the larger features are also FeNbB which are particles which remain from the primary ingot. These are rarely found and, as a result, are probably of little importance.

Chapter 8 showed the results of magnetic studies of melt-spun NdFeB materials with differing Nd content. It was found that the mean domain width increased with increasing grain size and also that it decreased with increasing Nd content. This suggests that the increased Nd leads to reduced coupling between the individual grains as happens in the sintered materials

In chapter 9, the composition of NiFe layers with spacer layers of Cu or Ta was investigated using EDX. It was found that for Cu layers deposited at room temperature the layer was sharper than one deposited at 300°. This was assumed to be as a result of increased diffusion at the higher temperature. The Ta layer, although deposited at 300° was found to be very sharp and this is because the Ta-NiFe interface is chemically stable even at high temperature. A rougher interface allows more coupling between the magnetic layers which leads to increased coercivity and this is confirmed by coercivity measurements on the films.

10.2 Future Work

There is great scope for more work on the sintered materials using the magnetic field of the CM-20 objective lens. This machine is eventually to be fitted with an EDX detector and so it will be possible to conclusively determine whether a grain boundary phase is present and then to subject the walls near that boundary to a field. The movement of walls in each grain should give an indication as to whether or not they are exchange coupled. The magnetising experiments can be extended by reversing the direction of the magnetic field and determining if, when the sample is subjected to this field, the domain period returns to the value obtained before the sample had 'seen' any field. It would be particularly

interesting to compare sample A to samples B and C since the coercivity of A (0.7T) is below the maximum objective field strength while that of B (2.9T) is substantially above it. Similar experiments could be carried out on the sintered materials but these would be more difficult since the Foucault mode would have to be used (Fresnel contrast is obscured by the microstructure). Since the standard objective lens will alter the beam divergence, this would have to be compensated for at each field value with the upper half of the Lorentz lens in order that the diffraction pattern was in the same plane as the objective aperture. The image quality would then have to be maximised with the lower half as before.

Appendix A

Analysis Programmes

The following listings are the programme WINDOSUM mentioned in chapter 6 and other files which the programme requires. It was compiled using the DJGPP port to DOS of the GNU C compiler gcc.

```
/*                        windosum                                    */
/* This programme takes a series of spectra and a windows file */
/* and produces an output file containing the window labels,   */
/* the window width, the centre energy of the window and the   */
/* total counts in each window in each spectrum. The file      */
/* is suitable for reading into Quattro Pro and probably many  */
/* other spreadsheets.    S Young.                             */

#include <stdio.h>
#ifdef __GO32__
#include <std.h>
#include <gppconio.h>
#include <pc.h>
#include <ctype.h>
#endif
#include <string.h>
#include "mytypes.h"
#include "windosum.h"

#define MAXWINDOWS 20

void main()
{
spectrum_type   spectrum;
A_WINDOW        w[MAXWINDOWS];
char            root_name[10],outfile[12];
char            full_name[12],meth,opt,prompt[8];
char            sum_str[10],output[15],number[5];
FILE            *handle;
```

```
double          centre[MAXWINDOWS];
unsigned long   wndw[MAXWINDOWS];
int             maxwi,no_of_spectra,overwrite,flag;
int             i,count,nchans,width[MAXWINDOWS];

system("cls");
printf("\nWINDOSUM: adds all counts in a series of windows\n\n");

printf("How many spectra: ");
scanf("%d",&no_of_spectra);

if (no_of_spectra<1) exit(0);
if (no_of_spectra==1)
 strcpy(prompt,"");
else
  strcpy(prompt,"root ");

if (no_of_spectra==1)
  strcpy(number,"");
else
  strcpy(number,"1");

printf("\nWhat's the %sname? ",prompt);
scanf("%s",root_name);

strcpy(full_name,root_name);
strcat(full_name,number);

printf("\nCalculate gross or net counts G/N?\n");
do
{
  meth=toupper(getch());
} while ((meth!='G') && (meth!='N'));

nchans=read_spectrum(&spectrum,full_name);
if (nchans==0) exit(0);

maxwi=read_windows(&w[0],&width[0],&centre[0],spectrum.gf,spectrum.x0);

overwrite=YES;
do
{
  printf("\nInput name for output file ");
  scanf("%s",outfile);
  strcat(outfile,".prn");
  handle=fopen(outfile,"rt");
```

```
  if (handle!=NULL)
  {
    fclose(handle);
    printf("OOPS: %s already exists. Overwrite? (y/n) ",outfile);
    fflush(stdout);
  do
  {
    opt=toupper(getch());
  } while ((opt!='Y') && (opt!='N'));
  if (opt=='Y')
  {
    overwrite=YES;
    printf("Yes\n");
  }
  else
  {
    overwrite=NO;
    printf("No\n");
  }
  }
} while (overwrite==NO);

/* Create new file or overwrite existing one */
handle=fopen(outfile,"wt");

fprintf(handle,"\"%s\"","Labels");
for (i=0;i<=maxwi;i++)
{
fprintf(handle,",\"%c%c%c%c",w[i].let2,w[i].let1,w[i].let4,w[i].let3);

if (meth=='N')
  fprintf(handle," %s\"","NET");
else
  fprintf(handle,"\"");
}

fprintf(handle,"\n\"%s\"","Centre energy");
for (i=0;i<=maxwi;i++)
{
  sprintf(output,"%4.2f",centre[i]);
  fprintf(handle,",%s",output);
}

fprintf(handle,"\n\"%s\"","Width chans");
for (i=0;i<=maxwi;i++)
```

```
{
  sprintf(output,"%d",width[i]);
  fprintf(handle,",%s",output);
}
fprintf(handle,"\n\n");

/*-----MAIN LOOP-----*/

for (count=1;count<=no_of_spectra;count++)
{
  sprintf(full_name,"%s%d",root_name,count);
  if (no_of_spectra==1) strcpy(full_name,root_name);
  printf("\n\t Processing %s.sp \n",full_name);
  nchans=read_spectrum(&spectrum,full_name);

  if (nchans!=0)
  {
  for (i=0;i<=maxwi;i++)
  {
     wndw[i]=add_em_up(&spectrum,w[i].low,w[i].high,meth,&flag);
     printf("\t\t%lu counts in %c%c",wndw[i],w[i].let2,w[i].let1);
     printf("%c%c\n",w[i].let4,w[i].let3);
  }
  fprintf(handle,"\"%s\"",full_name);
  for (i=0;i<=maxwi;i++)
  {
    sprintf(sum_str,"%lu",wndw[i]);
    fprintf(handle,",%s",sum_str);
  }
  fprintf(handle,"\n");
  }
  else{
    fprintf(handle,"\"%s\"",full_name);
    for (i=0;i<=maxwi;i++)
      fprintf(handle,",%s","0");
    fprintf(handle,"\n");
    }
}
fclose(handle);
fflush(stdout);
if (flag==YES)
  printf("\nCounts in some windows were negative and were rounded to 0\n");
printf("Output written to %s, press any key to exit\n",outfile);
getch();
printf("\n\n");
}
```

```
/* specread.c */
/* Stuart Young 1993 */
#include<stdio.h>
#ifdef __GO32__
#include <std.h>
#endif
#include "mytypes.h"

/* A routine to read in a spectrum */

int read_spectrum(spectrum,name)
spectrum_type   *spectrum;
char            *name;
{
int         nchans,i;
int         data_size;
FILE        *file_handle;

if (strlen(name)==0) return(0);

strcat(name,".sp");

file_handle=fopen(name,"rb");
if (file_handle==NULL)
{
  printf("ERROR: couldn't find %s\n",name);
  sleep(1);
  return(0);
}
/* Because structure is padded, read numbers individually */

fread(&spectrum->mtype,2,1,file_handle);
fread(&spectrum->mhdsize,2,1,file_handle);
fread(&spectrum->precision,1,1,file_handle);
fread(&spectrum->sign,1,1,file_handle);
fread(&spectrum->mcmin,2,1,file_handle);
fread(&spectrum->mcmax,2,1,file_handle);
fread(&spectrum->units,4,1,file_handle);
fread(&spectrum->gf,4,1,file_handle);
fread(&spectrum->x0,4,1,file_handle);
fread(&spectrum->lablchars,34,1,file_handle);
fread(&spectrum->memstate,2,1,file_handle);
fread(&spectrum->iscale,2,1,file_handle);
fread(&spectrum->nscale,2,1,file_handle);
```

```
nchans=1024*(int) (0.5+(spectrum->mcmax-spectrum->mcmin)/1024.0);
data_size=spectrum->precision/8*nchans;
/*
printf("Precision is %d, %d channels\n",spectrum->precision,nchans);
printf("Reading %d btyes\n",data_size);
*/
fseek(file_handle,-data_size,2);
if (spectrum->precision==16)
  fread(&spectrum->counts.cts16bit[0],nchans*2,1,file_handle);

if (spectrum->precision==32)
  fread(&spectrum->counts.cts32bit[0],nchans*4,1,file_handle);

fclose(file_handle);

if ((spectrum->iscale!=0) && (spectrum->nscale!=0))
for (i=0;i<=nchans;i++)
{
if (spectrum->precision==16)
spectrum->counts.cts16bit[i]*=(double) (spectrum->iscale/spectrum->nscale);
if (spectrum->precision==32)
spectrum->counts.cts32bit[i]*=(double) (spectrum->iscale/spectrum->nscale);
}
return(nchans);
}

/* win_rout.c */
/* Stuart Young 1993 */
#include <stdio.h>
#ifdef __GO32__
#include <std.h>
#include <pc.h>
#endif
#include <math.h>
#include "mytypes.h"

int read_windows(windows,win_width,centre_energy,gf,x0)
A_WINDOW    *windows;
int         *win_width;
double      *centre_energy;
float     gf,x0;
{
int         no_of_windows,no_of_bytes;
char window_file[16];
FILE *handle;
```

```
no_of_bytes=sizeof(A_WINDOW);

printf("\nWhat's the window filename? ");
scanf("%s",window_file);

strcat(window_file,".wi");
handle=fopen(window_file,"rb");    /*Open window file*/
if (handle==NULL)           /*file doesn"t exist*/
{
  printf("ERROR: That one doesn't exist (or I can't find it)\n");
  sleep(1);
  exit(0);
}
no_of_windows=0;
printf("\nReading window file %s...",window_file);
do
{
  fread(windows,no_of_bytes,1,handle);
  *win_width=windows->high-windows->low+1;
  *centre_energy=((windows->low+(*win_width/2.0)-x0)/gf);
  win_width++;
  centre_energy++;
  no_of_windows++;
} while (windows++->low!=-1);
fclose(handle);
printf("It has %d windows\n",no_of_windows-2);
return(no_of_windows-2);
}

unsigned long add_em_up(spectrum,low,high,meth,flag)
spectrum_type  *spectrum;
int             low,high,*flag;
char            meth;
{
unsigned long       i,winwid,bg,total;

total=0;
bg=0;
if (meth=='G')
  for (i=low;i<=high;i++)
    total+=spectrum->counts.cts16bit[i];

if (meth=='N')
{
  winwid=high-low;
  bg=(spectrum->counts.cts16bit[high]-spectrum->counts.cts16bit[low])/2.0
```

```
  bg+=spectrum->counts.cts16bit[low]);
  bg*=winwid;
  for (i=low;i<=high;i++)
    total+=spectrum->counts.cts16bit[i];
  if (bg>total)
    {
    bg=0;total=0,*flag=YES;
    }
}
 return(total-bg);
}

/* Header for windosum.c */

int read_windows(A_WINDOW *,int *,double *,double,double);
unsigned long add_em_up(spectrum_type *,int,int,char,int *);
int read_spectrum(spectrum_type *,char *);

/* This file contain various types and #defines required */
/* for the various x-ray spectra related programmes */

#define ERROR 4
#define LOWER_CASE 0
#define UPPER_CASE 1
#define DIGIT 2
#define READ 0
#define WRITE 1
#define YES 1
#define NO 0
#define EXP 0
#define MBH 1

typedef struct windo
{
  short low,high,efficiency;
  unsigned char let1,let2,let3,let4;
} A_WINDOW;

/* NB short type required in following for DJGPP */
/* but should be int for Borland C               */

typedef struct spec
{
  unsigned short        mtype,mhdsize;
  unsigned char         precision,sign;
  unsigned short        mcmin,mcmax;
```

```
  unsigned char         units[4];               /* Units */
  float                 gf,x0;                  /* Calibration numbers */
  unsigned char         lablchars[34];          /* Label characters */
  unsigned short        memstate,iscale,nscale; /* Scaling */
  unsigned short        remainder[481];
  union counts
  {
    unsigned short cts16bit[1024];
    unsigned int cts32bit[1024];
  } counts;
} spectrum_type;
```